Exploring thermal effects in neutron star mergers

Untersuchung thermischer Effekte in Neutronensternverschmelzungen
Zur Erlangung des Grades eines Doktors der Naturwissenschaften (Dr. rer. nat.)
Genehmigte Dissertation von Sebastian Blacker aus Groß-Gerau
Tag der Einreichung: 18. Januar 2024, Tag der Prüfung: 13. Mai 2024

1. Gutachten: Priv.-Doz. Dr. Andreas Bauswein
2. Gutachten: Prof. Dr. Gabriel Martínez-Pinedo
Darmstadt, Technische Universität Darmstadt

TECHNISCHE
UNIVERSITÄT
DARMSTADT

Fachbereich Physik
Institut für Kernphysik
Theoriezentrum

Exploring thermal effects in neutron star mergers
Untersuchung thermischer Effekte in Neutronensternverschmelzungen

Genehmigte Dissertation von Sebastian Blacker

Tag der Einreichung: 18. Januar 2024
Tag der Prüfung: 13. Mai 2024

Darmstadt, Technische Universität Darmstadt

Bitte zitieren Sie dieses Dokument als:
URN: urn:nbn:de:tuda-tuprints-265305
URL: http://tuprints.ulb.tu-darmstadt.de/26530
Jahr der Veröffentlichung auf TUprints: 2024

Dieses Dokument wird bereitgestellt von tuprints,
E-Publishing-Service der TU Darmstadt
http://tuprints.ulb.tu-darmstadt.de
tuprints@ulb.tu-darmstadt.de

In Gedenken an Jürgen, der uns so plötzlich und viel zu früh verlassen hat

Erklärungen laut Promotionsordnung

§ 8 Abs. 1 lit. c PromO

Ich versichere hiermit, dass die elektronische Version meiner Dissertation mit der schriftlichen Version übereinstimmt.

§ 8 Abs. 1 lit. d PromO

Ich versichere hiermit, dass zu einem vorherigen Zeitpunkt noch keine Promotion versucht wurde. In diesem Fall sind nähere Angaben über Zeitpunkt, Hochschule, Dissertationsthema und Ergebnis dieses Versuchs mitzuteilen.

§ 9 Abs. 1 PromO

Ich versichere hiermit, dass die vorliegende Dissertation selbstständig und nur unter Verwendung der angegebenen Quellen verfasst wurde.

§ 9 Abs. 2 PromO

Die Arbeit hat bisher noch nicht zu Prüfungszwecken gedient.

Darmstadt, 18. Januar 2024

S. Blacker

Abstract

In this work, we perform neutron star merger simulations with equation of state (EoS) models containing nucleonic, hyperonic or deconfined quark matter. In particular, we focus on the different behavior of hyperonic and deconfined quark matter phases at finite temperatures compared to purely nucleonic neutron star material and explore the impact on the resulting gravitational-wave (GW) signal. Both hyperons and deconfined quarks are hypothesized to be present at high densities in neutron stars. However, current observations and theoretical calculations are inconclusive. Therefore, the true composition of neutron star cores remains unknown.

To investigate the impact of hyperons on neutron star mergers, we perform the first comprehensive study with several different available hyperonic EoSs. At finite temperatures, more hyperons are produced, therefore lowering the degeneracy pressure of nucleons. We find that this reduced pressure in hot hyperonic material results in a characteristic increase of the dominant postmerger GW frequency up to about 150 Hz compared to purely nucleonic matter. This frequency shift can be directly linked to the presence of hyperons. Although the effect is weak, it could serve as an observational indication of hyperons in the future. Our finding is particularly relevant as mass-radius relations of cold hyperonic stars may be indistinguishable from nucleonic stars.

When employing models with a transition to deconfined quark matter, so-called hybrid models, we find that thermal effects can significantly influence the structure of the neutron star merger remnant. For the hybrid EoS sample we consider, this can be attributed to the shift of the quark-hadron phase boundaries at finite temperatures, which strongly reduces the pressure compared to cold matter. We explicitly show that if this change of phase boundaries is not taken into account, the dominant gravitational-wave frequencies can be underestimated by several hundred Hz.

Additionally, we devise an effective description to incorporate the effects of shifting phase boundaries to supplement cold EoSs with a Maxwell-type phase transition, i.e. two distinct phases connected by a flat coexistence region. We validate our model by comparing results to our fully temperature-dependent hybrid EoS sample and find very good agreement in the postmerger GW frequencies. We then explore the impact varying phase boundaries have for a fixed, cold EoS. Our findings suggest that for hybrid models, the shape of the phase boundaries can have a strong impact on merger observables such as GW frequencies and the prompt collapse of the remnant to a black hole. We also show explicitly that it is even possible for deconfined quark matter to only occur in finite temperature systems like merger remnants but not in cold, isolated stars. This demonstrates that postmerger GWs contain important information on the underlying EoS complementary to observations from individual NSs. Future detections of GWs from binary NS mergers hence have the potential to shed light on the presence of hyperons and deconfined quark matter in neutron star material and provide information on the phase diagram of quantum chromodynamics in addition to constraints from terrestrial experiments.

Zusammenfassung

In dieser Arbeit simulieren wir Verschmelzungen von Neutronensternen mit Zustandsgleichungsmodellen, welche nukleonische, hyperonische oder freie Quarkmaterie enthalten. Insbesondere legen wir den Fokus auf das unterschiedliche Verhalten von Materiephasen mit Hyperonen und freien Quarks bei endlichen Temperaturen im Vergleich zu rein nukleonischer Neutronensternmaterie und untersuchen den Einfluss auf die resultierenden Gravitationswellen. Sowohl Hyperonen als auch freie Quarkmaterie tauchen möglicherweise bei hohen Dichten in Neutronensternen auf, können allerdings durch aktuelle Beobachtungen und theoretische Berechnungen zur Zeit weder bestätigt noch ausgeschlossen werden. Die tatsächliche Zusammensetzung von Neutronensternkernen ist daher nach wie vor unbekannt.

Um den Einfluss von Hyperonen auf Neutronensternverschmelzungen zu erforschen, führen wir die erste umfassende Untersuchung mit zahlreichen verfügbaren hyperonischen Zustandsgleichungsmodellen durch. Bei endlichen Temperaturen werden mehr Hyperonen produziert, was den Entartungsdruck der Nukleonen senkt. Dieser reduzierte Druck in heißer, hyperonischer Materie führt zu einem charakteristischen Anstieg der dominanten Gravitationswellenfrequenz nach der Verschmelzung um bis zu 150 Hz im Vergleich zu rein nukleonischer Materie. Obwohl dieser Effekt klein ist, könnte er in Zukunft trotzdem als beobachtbarer Nachweis von Hyperonen dienen. Unser Resultat ist insbesondere deswegen relevant, weil die Masse-Radius Beziehungen kalter, hyperonischer Neutronensterne möglicherweise ununterscheidbar von denen nukleonischer Sterne sind.

Beim Verwenden von Modellen mit einem Übergang zu freier Quarkmaterie, sogenannten hybriden Modellen, finden wir einen erheblichen Einfluss thermischer Effekte auf die Struktur des Überrests der Verschmelzung. In den von uns verwendeten, hybriden Zustandsgleichungsmodellen kann dies auf die Verschiebung der Quark-Hadron Phasengrenze bei endlichen Temperaturen zurückgeführt werden, welche den Druck im Vergleich zu kalter Materie deutlich senkt. Wir zeigen explizit, dass die dominante Gravitationswellenfrequenz um mehrere Hundert Hz unterschätzt werden kann, wenn diese Änderungen der Phasengrenzen nicht berücksichtigt werden.

Zusätzlich entwickeln wir eine effektive Beschreibung, um den Einfluss von temperaturabhängigen Phasengrenzen für Zustandsgleichungen mit einer Maxwell-Phasenkonstruktion, also zwei getrennten Phasen welche durch eine flache Koexistenzphase verbunden sind, zu berücksichtigen. Wir validieren unser Modell, indem wir die Ergebnisse mit Resultaten aus temperaturabhängigen, hybriden Zustandsgleichungsmodellen vergleichen. Dabei finden wir sehr gute Übereinstimmungen der Gravitationswellenfrequenzen nach der Fusion der beiden Sterne. Anschließend untersuchen wir den Einfluss verschiedener Phasengrenzen für eine feste, kalte Zustandsgleichung. Unsere Ergebnisse legen nahe, dass die Form der Phasengrenzen einen großen Einfluss auf beobachtbare Größen von Neutronensternverschmelzungen wie Gravitationswellenfrequenzen oder den direkten Kollaps des Überrests zu einem Schwarzen Loch hat. Wie wir explizit zeigen, besteht sogar die Möglichkeit, dass freie Quarkmaterie nur bei endlichen Temperaturen in Systemen wie kollidierenden Neutronensternen existiert, aber nicht in kalten, isolierten Sternen auftritt. Dies macht deutlich, dass Gravitationswellen, welche nach einer Neutronensternverschmelzung emittiert werden, wich-

tige Informationen über die zugrundeliegende Zustandsgleichung komplementär zu Beobachtungen einzelner Neutronensterne beinhalten. Zukünftige Beobachtungen von Gravitationswellen aus Neutronensternverschmelzungen haben daher das Potential, zusätzlich zu irdischen Experimenten Aufschluss über das Vorkommen von Hyperonen und freier Quarkmaterie in Neutronensternmaterie und über das Phasendiagramm der Quantenchromodynamik zu geben.

Contents

List of Figures

List of Tables

Nomenclature

List of abbreviations

ADM	Arnowitt-Deser-Misner
BNS	binary neutron star
CFC	conformal flatness condition
eff PT	effective phase transition
EoS	equation of state
GR	general relativity
GW	gravitational waves
MR	mass-radius
NS	neutron star
NN	nucleon-nucleon
RMF	relativistic mean field
SNA	single nucleus approximation
SPH	smoothed particle hydrodynamics
TOV	Tolman-Oppenheimer-Volkoff
χEFT	chiral effective field theory
SF	string flip
YN	hyperon-nucleon
YY	hyperon-hyperon
1D, 3D	one-, three-dimensional

1. Introduction

1.1. Neutron stars and neutron star mergers

Neutron stars (NSs) are compact astrophysical objects that contain more mass than our sun in a volume comparable to the extent of a mid-sized city. They form during the final evolution phase of massive stars through the gravitational collapse of the stellar core [1]. As the densities in NSs surpass even those of atomic nuclei, studying these objects provides insights into a phase of matter which is currently not fully understood [2]. In particular, the composition of neutron star material at densities above nuclear saturation density $\rho_{\text{nuc}} = 2.7 \times 10^{14} \text{g/cm}^3$ remains unknown due to our incomplete knowledge of the relevant interactions [3, 4, 5]. At these densities, matter could be composed of neutrons, protons, electrons and muons. However, more exotic phases may exist in NS cores. These could include heavy baryons such has hyperons and Δ baryons [6, 7, 8, 9], pion or kaon condensations [10, 11, 12, 13] or even different states of deconfined quark matter [14, 15, 7, 16, 17].

Systems containing two neutron stars orbiting each other can form from massive stellar binaries after both progenitors explode as supernovae provided the system is not disrupted [18, 19]. These binary neutron star (BNS) systems perpetually lose energy and angular momentum through the emission of gravitational waves (GWs) leading to a slow but continuous inspiral and eventually to a violent collision of the two stars [20].

We show the main evolution stages of a BNS merger in Fig. 1.1. These snapshots depict the density (top row) and the temperature (bottom row) in the equatorial plane from a simulation of two colliding $1.4\ M_\odot$ NSs conducted in this thesis. The general dynamics are in agreement with results found in other works, see e.g. [21, 22, 23, 20, 24]. In the late inspiral phase (left column in Fig. 1.1), the two star begin deforming each other through tidal effects. At this stage, the temperatures in the system are still low. During the merger of two neutron stars (middle column in Fig. 1.1), the densities in the system increase and can reach a few times nuclear saturation density. Parts of the initially cold NS matter are heated up to several tens of MeV by shocks, first at the collision interface and later in the merger remnant. Some material is also ejected in the process [23, 24]. The further fate of the system then depends on its mass as well as on the internal properties of dense matter [25]. A not too massive remnant, as the one shown in Fig. 1.1, is temporarily stabilized against gravitational collapse through its rapid, differential rotation. In these systems, the initially deformed and strongly oscillating remnant settles down into a more axial axial-symmetric state on the timescale of milliseconds, as can be seen by comparing the middle and the right column of Fig. 1.1. We also see that the temperature profile in the late evolution stage shows a cold central core surrounded by a hot ring structure and spiral waves in the lower density parts.

A more massive remnant on the other hand will directly form a black hole. The mass separating the two potential outcomes is commonly referred to as the threshold mass for prompt collapse, M_{thres}. Its exact value depends on the mass asymmetry of the system and, more importantly, on the microphysical properties of dense matter [26, 27, 28, 29]. Hence, M_{thres} is an crucial quantity

that contains valuable information on NS matter and also fundamentally impacts the dynamics in the BNS postmerger phase.

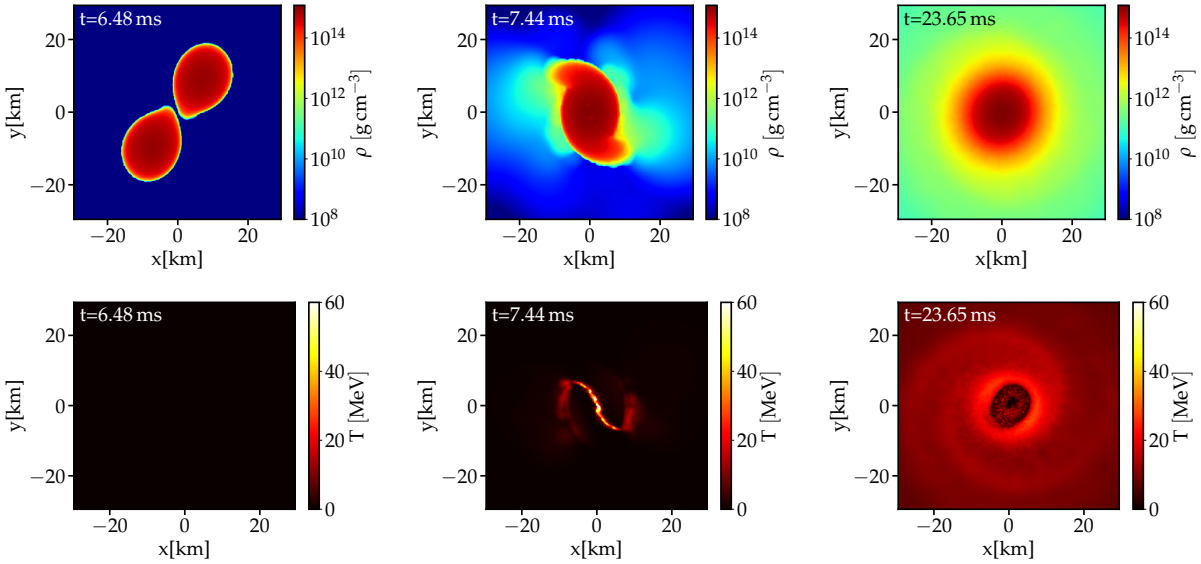

Figure 1.1.: Rest mass density (top row) and temperature (bottom row) in the equatorial plane at different stages of a merger simulation including two $1.4\ M_\odot$ neutron stars with the SFHo model describing the internal pressure of dense matter [30, 31]. See Sect. 3.2.1 for details on the SFHo model and Sect. 2.1 for information on the simulation code. Note the logarithmic scale of the density.

The recent progress in GW astronomy now allows us to observe BNS mergers [32, 33] and study the properties of matter in these events. Following the evolution of the system, the BNS merger GW signal can be divided into an inspiral part and a postmerger part [34]. At larger orbital separation, the inspiral part resembles a signal of two point masses. In this regime, the GWs are mainly shaped by the so-called chirp mass of the system, $\mathcal{M} = (m_1 m_2)^{3/5}/(m_1 + m_2)^{1/5}$, where m_i denotes the masses of the individual stars [35]. During the late inspiral phase, the tidal effects caused by the two stars deforming each other leave an additional imprint on the GW signal [36, 37, 38, 39]. The postmerger part depends on the fate of the remnant. In the case of a direct collapse, the GWs merely show a fast ring-down of the formed black hole [40, 41, 42]. A massive neutron star remnant on the other hand, produces a more interesting signal shaped by oscillations and deformations of the resulting object (see e.g. [43, 44, 45, 46, 47, 48, 49]).

An analysis of the complete GW signal from BNS mergers is particularly interesting for studying the properties of extremely dense matter because it allows us to simultaneously probe the different conditions present during the evolution of the system [50, 51]. In the late inspiral phase, the material is cold and in weak equilibrium composition as the merging NSs are very old. The GWs emitted after the merger on the other hand, can carry information on matter at higher densities and temperatures as well as potentially different compositions compared to the inspiral signal. A simultaneous detection of pre- and postmerger GWs can hence greatly increase our understanding of neutron star matter [52, 50, 53, 54].

1.1.1. Neutron star merger observations

Up to this day, GWs from two BNS mergers have been observed [32, 33]. In both cases, only the inspiral parts were recorded.

The first detection was the famous GW170817 event detected by the Advanced LIGO [55] and Advanced VIRGO detectors [56] on the 17th of August 2017 [32]. The GW signal was observed for $\sim$100 s allowing for a precise inference of the systems' chirp mass. The tidal effects from the late inspiral were also constrained, enhancing our understanding of the properties of cold neutron star matter [57]. No postmerger GW emission was detected, which was likely caused by the lower sensitivity of the available detectors at higher frequencies [58].

The event was succeeded by a short gamma-ray burst 1.7 s after the GW signal detection [59, 60, 61, 62], confirming that BNS mergers are sources of these extremely luminous events.

An optical signal named AT2017gfo was identified about 11 h later in a region of space consistent with the sky localization from the GW detectors [63, 64, 65], which rapidly evolved over the span of a few days shifting from mainly blue to red and near infrared [66, 67, 68]. This so-called kilonova is believed to be caused by the radioactive decay of heavy nuclei synthesized in the neutron rich ejected material from the merger by the so-called rapid neutron capture process (r-process) [69, 70, 71, 72]. This process plays an important role for the creation of heavy elements in the universe (see e.g. [73, 74, 75] for reviews). The main production site of the r-process is still subject to ongoing research. The observations from AT2017gfo indicate that mergers involving neutron stars contribute to the synthesis of r-process material in the universe [72, 76, 24] as was hypothesized decades ago [77, 78].

A second, probable NS merger named GW190425 was recorded on the 25 of April 2019 by the Advanced LIGO detector [33]. The inferred distance to the source was significantly larger than for GW170817. An interesting feature of this event was its large system mass of roughly $3.4\ M_\odot$, which is still compatible with the progenitor being a BNS system but considerable higher than the currently known galactic NS binaries [79]. No electromagnetic or postmerger GW signals were found [80]. This may be attributed to the relatively poor sky localization in combination with the large distance to the source. Furthermore, a binary this massive is expected to undergo prompt black hole formation, which should also reduce the amount of ejecta making the resulting kilonova dimmer [33, 81, 82].

Alongside these two BNS events, GWs from numerous binary black hole mergers have been observed over the last few years [83, 84, 85, 86]. In addition, the GW detectors have so far found two signals likely originating from coalescing neutron star-black hole systems [87]. These observations clearly demonstrate the potential GW astronomy has for studying mergers of compact objects and enhancing our understanding of their nature. In particular, the joint and follow-up electromagnetic studies of GW170817 have provided valuable information on several topics such as the r-process, the properties of neutron star matter and the origin of short gamma-ray bursts. Further areas of research from GW astronomy also include constraints on alternative theories of gravity [88] and an independent determination of the Hubble constant [89].

The most sensitive available gravitational-wave detector Advanced LIGO [55] is currently in the fourth observation run, O4, the detectors Advanced Virgo [56] and KAGRA [90] are anticipated to join this run in spring of 2024 [1]. A fifth period with further increased sensitivities is expected to begin in 2027 [91] and an additional detector LIGO-India is planned [92].

In addition, third-generation detectors such as the Einstein Telescope [93] or Cosmic Explorer [94] are expected to have about an order of magnitude better GW sensitivity compared to current detec-

[1] A schedule for the GW observation periods can be found on the webpage https://observing.docs.ligo.org/plan/

tors [95]. Hence, more BNS mergers are expected to be observed in the next years. Owing to the extremely small influence GWs have on their surroundings, distinguishing GW from background noise is very challenging and requires matching of detector data to precomputed waveform models. To correctly interpret future observations, reliable waveforms have to be developed [34] requiring a good theoretical understanding of relevant effects in BNS mergers and how they impact the GW signal. It is therefore crucial to employ accurate models for the properties of dense matter as well as sophisticated numerical simulations of BNS mergers.

1.2. The dense matter equation of state

A crucial step to reliably describe NSs and dense matter is the correct modeling of the underlying equation of state (EoS). The EoS provides the internal matter pressure as a function of density, composition and temperature. For describing neutron stars, an EoS model must consider a wide range of densities, where matter behaves quite differently. At lower densities in the crust of NSs, matter clusters into heavy nuclei [7]. At intermediate densities, matter becomes homogeneous, likely composed of superfluid neutrons, superconducting protons, electrons and muons [5], while the composition at even larger densities is unknown.

In many astrophysical applications such as simulations of neutron star mergers or core-collapse supernovae, matter can be hot and out of beta-equilibrium composition [96, 22, 97, 98, 20]. Hence, an EoS model suitable for these applications has to also account for a wide range of temperatures and high proton-neutron asymmetry. These types of models are usually referred to as 3D or general-purpose EoSs (see e.g. [5, 3, 99] for reviews). Due to the additional complexity, the number of general purpose EoS is limited and many more models are available as barotropic EoSs, i.e. at zero temperature in beta-equilibrium composition. Overviews can be found in the provided reviews and on repositories such as COMPOSE [2] [100, 3, 101].

In principle, the EoS of high-density matter could be derived from quantum chromodynamics (QCD), the fundamental theory of the strong interaction (see e.g. [102, 103] for overviews on QCD). However, from the point of QCD, a nucleon is a very complicated system composed of valence quarks, sea quarks and gluons [104]. The interaction between only two nucleons is hence already an interaction between two very complex objects. This makes a direct inference of the NS EoS from QCD currently unachievable and effective models have to be employed.

Current models of the high density EoS are based on several different approaches (see e.g. [3, 105, 106, 5, 99], for overviews). These can broadly be grouped into two categories: phenomenological and ab-initio EoSs.

Phenomenological EoSs are based on effective interaction models containing parameters that are typically fitted to reproduce properties of nuclei. Popular examples are relativistic mean-field models [107, 108] and non-relativistic Skyrme [109, 110, 111, 112] and Gogny [113, 114] interactions. A disadvantage of these approaches is that they are gauged by finite nuclei in their ground state and hence have to be extrapolated to higher densities and isospin asymmetries. These extrapolations may not always be reliable [115, 5].

Ab-initio EoS on the other hand employ realistic two- and three-body nucleon interactions that are based on scattering data and properties of light nuclei, e.g. [116, 117, 118, 119, 120, 121, 122]. With these interactions, one has to solve the many-body problem to determine the EoS. Many different approaches exist for this task (see e.g. [123, 124, 125, 126, 127, 128] or EoS reviews such as [3, 105, 106, 5, 99]).

[2] https://compose.obspm.fr

A particular ab-initio approach is the so-called chiral effective field theory (χEFT). This is an effective description with nucleons as relevant degrees of freedom that allows for a systematic expansion into higher order terms to obtain the nuclear forces. See e.g. [129, 130, 131] for reviews. With certain assumptions on the convergence behavior, this approach provides uncertainty estimates for the resulting EoSs from the neglected terms [132]. However, χEFT calculations are currently limited to densities and temperatures below roughly $2 \times \rho_{\text{nuc}}$ and 30 MeV, respectively [131]. For applications to neutron stars, the results of χEFT must therefore be combined with other approaches.

A general downside of ab-initio EoSs is that they can only be employed for the description of homogeneous matter [3, 5]. To obtain general purpose EoSs, they need to be supplemented with an effective model for the NS crust.

In addition to phenomenological or ab-initio models, parametric EoSs such as piecewise polytropic [133] or constant speed of sound descriptions [134] are commonly employed. These are representations of the EoS using a specific functional form and do not include any microphysics. Their appeal is their simplicity, i.e. that they can easily be adjusted in any desired way, which can be useful for exploring the available parameter space.

With several different EoS models and approaches available, it is important to confront them with observational and experimental constraints.

1.2.1. Current constraints on the equation of state

Besides basic requirements such as causality and thermodynamic stability, important current constraints on the high density EoSs come from astrophysical observations of NSs. Since NSs are in hydrostatic equilibrium with the internal pressure balancing the gravitational attraction, the stellar structure equations of general relativity (GR), the so-called Tolman-Oppenheimer-Volkoff (TOV) equations [135, 136] (see Sect. 3.1), provide a unique mapping between an EoS model and the mass-radius relation of neutron stars. For this, one typically assumes NSs to be cold and in weak equilibrium composition. Hence, a combined measurement of masses and radii of several NSs can in principle reveal the EoS of cold high-density matter. While NS masses have been inferred with high precision from observations of binary systems including pulsars [137, 138, 139, 140], radius measurements are extremely challenging because NSs are very small, far away objects [141, 142, 2].

Recently, the NICER mission has provided two simultaneous mass- and radius-measurements of the pulsars PSR J0030+0451 [143, 144] and PSR J0740+6620 [145, 146] using Bayesian parameter estimation. This inference relies on modeling the geometry of hot spots on the surface of the star and and results can vary for different assumed hot spot shapes [147]. Additional assumptions on e.g. the NS atmosphere or the background also need to be made.

A generic feature of solutions to the TOV equations is the existence of a maximum mass [148]. Any NS mass measurement hence already places constraints on the EoS as all models that fail to reach an observed mass are immediately ruled out. Current observations of massive pulsars indicate that the maximum NS mass is at least two solar masses [139, 140]. A very recent joint reanalysis of different detections even suggests the maximum TOV mass is larger than $2.09\ M_\odot$ at 3σ confidence interval [149]. These observations show that the NS EoS has to be relatively stiff.

Additional astrophysical constraints come from limits on the tidal deformability Λ set by the event GW170817 [32, 57, 150]. This parameter quantifies how easily a NS can be deformed by an external tidal field (see Sect. 3.1 for a mathematical definition), which depends on its compactness. Limits on the NS maximum mass and NS radii were also inferred from this event. These are (partly) based on universal EoS-insensitive relations between different observables and the assumption that the remnant did not immediately collapse to a black hole (see e.g. [151, 152, 153, 154, 155, 156,

27, 157, 158, 159]).

Further astrophysical constraints can for example come from observing the cooling of NS [160, 161, 162, 163] or from measuring the gravitational redshift of the 511 keV line from electron-positron annihilation at the surface [164].

In addition to astrophysical observations, the EoS can also be explored in nuclear physics and heavy-ion collision experiments (see e.g. [165, 166, 167, 168, 169, 170, 171, 5, 172]) at current and future facilities such as ALICE [173], HADES [174], CLAS [175], J-PARC [176], FAIR [177, 178, 179] or NICA [180, 181].

Recent works have also aimed to further constrain the EoS from the behavior of perturbative QCD calculations at asymptotically large densities [182, 183, 184] or by employing statistical methods to combine different measurements (e.g. [158, 185, 186, 187, 188, 159, 189, 190, 191, 149, 192, 193]).

1.2.2. Hyperons in neutron stars and the hyperon puzzle

An interesting possible feature in neutron stars is the occurrence of hyperons, i.e. heavy baryons with strangeness, at high densities (see e.g. [6, 7, 194, 8, 9]). In terrestrial conditions these particles are unstable and decay into nucleons. In neutron stars however, Pauli blocking could increase the chemical potential enough to make the inverse reaction energetically favorable leading to stable hyperonic matter. Once hyperons appear, they should reduce the Fermi pressure of the baryons and hence soften the EoSs [195, 196]. On the other hand, current observations of heavy pulsars indicate a maximum mass above $2\ M_\odot$ or even higher [139, 140, 149] and require the EoS to be stiff at high densities. The apparent tension between the energetically expected occurrence of hyperons in NSs and the stiff EoS required by NS mass measurements is commonly referred to as the hyperons puzzle [197].

Possible explanations to this puzzle could be sufficiently repulsive hyperon-hyperon (YY), hyperon-nucleon (YN) or hyperon three-body interactions [198, 199]. See e.g. [169, 200, 201, 202, 203, 204, 205] for current theoretical models. These interactions could either increase the stiffness of the hyperonic EoS or push the onset density of hyperons outside of the densities reached in NS cores. In the latter case, NSs would remain purely nucleonic at all masses.

An increasing number of EoSs that include hyperons and allow for $2\ M_\odot$ NSs have become available (e.g. [206, 207, 208, 209, 210, 211, 212]). The resulting NS models from these EoSs however, do not show distinct features compared to purely nucleonic EoSs. This suggests that even precise observations of NSs or tidal deformability measurements may not be sufficient to infer the presence of hyperons (see Sec. 5.1). Additional constraints from different astrophysical observations and terrestrial experiments will hence be needed to resolve the hyperon puzzle.

There are ongoing efforts to measure the YY and YN interactions from observing properties of hypernuclei [213, 214, 215, 216, 217] and scattering experiments including hyperons [218, 219, 220, 221, 222]. These are however hampered by the short lifetime of hyperons and limited to lower densities. Further information on hyperonic interactions come from the so-called femtoscopy technique that measures correlations in momentum space for hyperons produced in collider experiments [223, 224, 225, 226, 227, 227, 228, 229].

Astrophysical indications on the presence of hyperons can come from observations of NS shortly after supernovae. If hyperons are present in NSs, the trapped neutrions in the newly born proto-NS are expected to reduce the fraction of hyperons and stiffen the EoS. Once the star cools and neutrinos eventually leave, more hyperons can be present and the EoS should become softer possibly leading to a gravitational collapse [230]. More information can be found for example in

Refs. [231, 232, 233, 234, 197, 9]. Additionally, a surviving NS containing hyperons should cool more rapidly via Urca processes than a purely nucleonic star as the presence of hyperons allows for more weak reactions to take place. See e.g. [160, 161, 197, 235, 236, 237, 238, 239, 8, 9] for details.

So far all constraints are inconclusive and the hyperon puzzle remains unsolved in the sense that it is unknown whether hyperons are present in NS cores or not. In this work we will discuss the possibility to identify hyperons with the help from GW observations of BNS mergers.

1.2.3. Deconfined quark matter in neutron stars

A second possible feature in neutron stars and also a potential solution to the hyperon problem is a transition from hadronic to deconfined quark matter at high densities. Such a transition is expected to occur at some density due to the asymptotic freedom of quarks and gluons as fundamental degrees of freedom in QCD [15].

At zero baryon chemical potential, QCD predicts a smooth cross-over transition from hadronic matter to the quark-gluon plasma [240]. This regime is accessible through theoretical lattice QCD calculations and accelerator experiments [170, 240, 172]. At high densities and low temperatures present in neutron stars, the transition is less understood. Here, no ab-initio calculations of deconfined quark matter are available and only phenomenological models can be employed (e.g. [241, 242, 243, 244, 245, 246]). As a result, key features of the quark-hadron phase transition such as the onset density, the latent heat, the type of transition (smooth crossover or first-order), the behavior of the phase boundaries at finite temperatures as well as properties of the deconfined quark phase remain unknown [247, 248, 15, 7, 17, 16].

The possibility that NSs contain deconfined quark matter has been explored for a long time [14, 249]. See [15, 7, 17, 16] for recent reviews. Neutron stars containing a core of deconfined quark matter surrounded by hadronic material are commonly referred to as hybrid stars and the underlying EoS as hybrid EoS. In contrast, strange stars entirely made out of deconfined up, down and strange quark matter could also exist [249, 250, 251].

To model hybrid EoS, a two-phase approach is typically employed. In this scheme, two individual EoSs for the hadronic and the deconfined quark matter phase are formulated. These are then joined by a phase construction. A common choice is the so-called Maxwell construction with a density jump between the two separate phases occurring at equal pressure and chemical potential for a fixed temperature. Other choices allow for coexisting individually charged phases or a smooth transition from one phase to the other. See [252, 253, 254, 255] for details. A number of hybrid EoS models with different constructions are available at zero temperature, see e.g. [241, 250, 256, 257, 258, 259, 260, 244, 261, 262, 263, 264, 265, 266, 267, 268, 269, 270, 271, 272, 273] or EoS repositories such as COMPOSE [100, 3, 101]. Finite-temperature hybrid EoSs also exist (e.g. [274, 275, 276, 277, 278, 279, 280, 281, 282, 283, 284, 285, 286]), their number is however still somewhat limited.

Constraints on deconfined quark matter can in principle come from heavy-ion collision experiments (see e.g. for a review [287]). However, these experiments are currently somewhat difficult to interpret due to their very complex nature and generally probe the EoS at higher temperatures than those present in NSs.

Astrophysical constraints on the hadron-quark phase transition can mainly be provided by observations of core-collapse supernovae [288, 274, 276, 289, 290, 291, 292], where the presence of deconfined quarks is expected to influence the overall dynamics and the neutrino signal, as well as by observations of NSs (see e.g. [293, 294, 295, 296, 297, 298, 299]). A strong phase transition,

followed by a stable hybrid star branch will result in a kink in the neutron star mass-radius and mass-Λ curves as the associated large density jump leads to more compact stars [300, 293]. Such kinks could potentially be observable by very precise measurements over a wide span of neutron star masses. A second possibility is that the onset of the hadron-quark transition no longer permits stable NSs. This would result in a sudden end of the mass-radius curve and could in principle also be detectable (see discussion in Sect. 4.4.4). On the other hand, the transition may also be more continuous. In this case, the mass-radius relation of hybrid stars could be more similar to that of nucleonic or hyperonic EoSs and even several very precise measurements would not reveal the presence of quark matter. This ambiguity is commonly referred to as the masquerade problem [261].

In general, available constraints on the QCD phase transition are sparse and the question if deconfined quark matter appears in NSs remains open. A promising new window to address this question is offered through studying neutron star mergers.

1.3. Modeling thermal effects and exotic matter phases in neutron star mergers

So far, no postmerger GW signals from BNS mergers have been detected. Our current understanding of this evolution phase therefore relies on sophisticated numerical simulations. Since NS are extremely compact objects, these simulations need to be carried out in the framework of numerical, general relativistic hydrodynamics. Several different approaches have been employed over the past years, see e.g. [301, 302, 303, 304, 305, 306, 307, 308, 309] for overviews on numerical methods and employed codes. Although numerically stable formulations of the Einstein equations are available [310, 311, 312, 313, 314, 315, 316], these are computationally expensive. Therefore, approximations to general relativity are also used. In this work we will employ the conformal flatness condition (CFC) [317, 318], which greatly simplifies the equations while still keeping the essential features of general relativity (see Sect. 2.1 for details).

In addition to the hydrodynamic equations and gravity, BNS merger simulations require an EoS model to evolve the system. Owing to the current ambiguity on the EoS of dense matter, the general approach taken in simulations is to employ many different EoS models (somewhat) compatible with current constraints. The goal is to link different results to special EoS features or find universal relations between observables valid for all EoS models. This will help interpreting future observations and narrow down the EoS model space by ruling out incompatible EoSs.

Because matter is heated up during the postmerger phase and may be out of weak equilibrium composition, general purpose EoS models are desirable for BNS merger simulations. Since the number of 3D EoSs is limited, many works (e.g. [45, 47, 52, 319, 320, 321, 322, 323, 53, 324, 29, 325, 326, 327, 328, 329, 330, 331, 332]) also employ zero-temperature EoSs (microphysical or parametric) in combination with approximate thermal treatments. A popular choice is the so-called ideal-gas approach [333], which assumes an ideal-gas like thermal behavior at all densities and temperatures (see Sect. 2.2 for details). For nucleonic EoSs, it generally reproduces simulation results from general purpose models well [22]. Recently, Ref. [334] presented a more sophisticated scheme allowing for an approximate extension of a barotropic EoS to arbitrary electron fractions and temperatures under the assumption that matter is composed of protons, neutron, electrons and photons.

A general feature of all currently available BNS merger simulations with no direct black hole formation is the emergence of a dominant peak in the postmerger gravitational-wave spectrum. This peak is related to the fundamental quadrupolar oscillation mode of the merger remnant [43].

Its frequency f_{peak} depends on the mass configuration of the system as well as on the employed EoS model [45, 335, 49]. It has been shown to correlate with the remnant size and properties of resulting cold NS such as radii or tidal deformabilities [45, 44, 47, 48, 336, 51, 337]. A future detection of a postmerger signal and a measurement of f_{peak} will hence place immediate constraints on the cold matter EoSs.

Hyperonic EoSs have been employed in merger simulations (e.g. in [338, 44, 46, 47, 339, 340, 341, 52, 322, 337, 29, 53, 330, 342]) using general purpose models as well as barotropic EoS supplemented with the thermal ideal-gas approximation. However, few works have put the focus on the specific impact of hyperons. Refs. [343, 344] respectively compare results employing a specific nucleonic EoS with and without the additional inclusion of hyperons. Both works find increased postmerger GW frequencies and earlier collapses to a black holes of the systems with hyperons. A goal of this thesis is to perform a similar comparison but to employ two representative sets of general purpose EoS, one containing hyperonic and one with purely nucleonic EoSs, to find systematic differences that can be attributed to the presence of hyperons. Such a systematic study on EoSs including hyperons has not been performed so far.

Deconfined quark matter has also been studied in merger simulations. As the number of general purpose hybrid models, i.e. models featuring a transition to deconfined quark matter, is currently limited, few merger studies have been carried out employing these EoSs [345, 346, 52, 53, 28, 324, 29, 285, 347, 348]. Additionally, zero temperature hybrid EoS (microphysical or parametric) have also been employed together with the thermal ideal-gas approximation [319, 322, 321, 325, 327, 328, 329, 330, 349, 331, 332]. Since a strong phase transition softens the EoS, studies employing models with such a feature generally show larger postmerger frequencies and in some cases earlier collapses and reduced threshold masses. Several works have focused on ways to identifying and study a strong phase transition in BNS mergers [345, 52, 319, 53, 350, 351], partly by combining pre- and postmerger GW observables and comparing results to hadronic EoSs. On the other hand, if the transition to deconfined quark matter is more continuous and the EoS does not feature sudden density jumps, an unambiguous identification of the phase transition becomes more challenging [330, 327, 328, 350].

It is important to remark that postmerger observables of BNS mergers such as f_{peak} are also influenced by the finite-temperature EoS since parts of the merger remnant are heated up during the coalescence of the stars and the further evolution of the system. While the dependence of f_{peak} on properties of the cold EoS has been widely studied, the influence of the finite-temperature EoS on f_{peak} has received little attention. Only a few works have focused on explicitly employing different EoS descriptions at finite temperatures for a fixed cold EoS [22, 352, 353, 354, 355]. These were also limited to purely nucleonic models. So far, a systematic study on the influence thermal effects in exotic phases of matter have on GW signals from BNS mergers has not been performed.

In EoSs containing hyperons or deconfined quarks, the finite-temperature part is expected to be different from nucleonic EoS as other degrees of freedom are available. In current hyperonic models, the onset density as well as the abundances of different hyperon species vary with temperature (see e.g. [207, 208, 210, 211, 212, 209]). For the QCD phase diagram, the temperature-dependence of the phase boundaries is an inherent and characteristic property (see e.g. [356, 357, 247, 248, 245, 358, 246, 172]). Hence, the finite-temperature behavior of hyperonic or hybrid EoS should be more complex than for typical nucleonic models. Applying the ideal-gas approximation, as has often been done in previous works, may therefore not always be reliable. This motivates an exploration of thermal effects in merging systems containing exotic matter, which we will perform in this thesis. A good understanding of the thermal EoS is crucial to correctly interpret future observations from BNS mergers and to connect results from heavy-ion collision experiments, which

probe the phase diagram at larger temperatures [359, 287].

1.4. Goals and outline of this thesis

The goal of this thesis is to explore the effect of hyperon and deconfined quark matter phases at finite temperatures on neutron star merger observables. In particular, we focus on how the thermal parts of these exotic matter phases impact the GW signal compared to a typical "nucleonic" thermal behavior. We aim to find potential signals that can help identifying the presence of hyperons and deconfined quark matter, once postmerger GWs from BNS mergers are observed.

To investigate thermal properties of hybrid EoSs, we devise an extension of the commonly used ideal-gas approach [333] to include temperature-dependent phase boundaries. With this scheme, we then explore the effect of varying phase boundaries for a fixed cold EoS in different scenarios. We additionally employ EoS models studied in the literature to investigate how previous findings are influenced by finite-temperature effects.

We also perform the first comprehensive study of available general purpose EoS containing hyperonic degrees of freedom that are roughly compatible with current constraints. We compare the results to simulations using only the cold hyperonic EoS part and assuming a thermal behavior typical of nucleons. In addition, we perform several simulations employing different purely nucleonic models. Our aim is to quantify how much the postmerger frequencies are shifted under the influence of hyperons at finite temperatures across all EoSs in our sample. Our results for hyperonic EoSs are presented in [360] and the findings for hybrid EoS are published in [361].

The outline of the thesis is the following: In chapter 2, we give an overview of the simulation code we use for BNS merger simulations and discuss the ideal-gas approach. Chapter 3 contains information on all employed nucleonic, hyperonic and hybrid EoSs as well as the necessary equations to calculate neutron star properties from an EoS model. We present our extension of the ideal-gas approach and the impact of varying phase boundaries for a fixed, zero-temperature, hybrid EoSs in chapter 4. Here, we also discuss a toy model to construct some phase boundaries we employ in our analysis. In chapter 5, we show the results from our hyperonic EoS study. We summarize and discuss our findings in chapter 6 and outline potential future extensions. Additionally, Appendix A presents some improvements to the merger code that were implemented over the course of this thesis.

1.5. Conventions

Throughout this work, we use geometric units with $c = G = 1$ unless explicit units are provided, where c is the vacuum speed of light and G the gravitational constant. Masses are given in units of a solar mass $M_\odot$. We include gravity with the framework of general relativity and adopt the signature convention (-,+,+,+) for the metric. Greek indices refer to both space and time coordinates and run from 0 to 3 while Latin indices range from 1 to 3 and refer exclusively to spatial coordinates. Unless stated otherwise, we employ the Einstein summation rule. Differential operators Δ and ∂_i refer to spatial derivatives with respect to the flat three metric. In asymmetric binary neutron star systems, we define the mass ratio of the system as $q = M_2/M_1$ with $q < 1$. $M_{1,2}$ refer to the masses of the individual stars.

2. Numeric models

This chapter provides an overview on the physical and numerical models used in this work to simulate binary neutron star mergers. Due to neutron stars being extremely compact objects, the simulations have to be performed within the framework of general relativity. We discuss the simulation code in Sect. 2.1 and the ideal-gas approach to approximate thermal effects in Sect. 2.2.

2.1. Simulation code

All simulations in this thesis are preformed using a general relativistic, smoothed particle hydrodynamics (SPH) code. Detailed information on this simulation tool can be found in [362, 21].

The SPH method is a well-established procedure to numerically solve the equations of fluid dynamics. It was originally introduced in Refs. [363, 364] for simulating stars, but has been used extensively since then for modeling several physical systems. See e.g. [365, 366, 306] for reviews.

The main idea of SPH is to model a continuous fluid with an ensemble of particles with fixed masses. All physical quantities (such as pressure, density, etc.) are evaluated at the positions of these particles, i.e. comoving with the fluid. An additional so-called kernel function $W(\vec{r}-\vec{r}_a, h_a)$ is then used to smooth out physical properties over a spatial domain. This function is typically spherically symmetric, differentiable and features a maximum at the particle position $\vec{r}_a$ with a monotonic decrease at increasing distance $|\vec{r}-\vec{r}_a|$ from the particle a. The spatial extent of the kernel function is characterized by the smoothing length h_a. Many different kernel functions are available in the literature (see e.g. [306] for an overview). The code used in this work employs a cubic spline kernel

$$W(\vec{r}-\vec{r}_a, h_a) = \frac{1}{\pi h_a^3} \begin{cases} 1 - \frac{3}{2}d^2 + \frac{3}{4}d^3 & \text{for } 0 \leq d \leq 1 \\ \frac{1}{4}(2-d)^3 & \text{for } 1 \leq d \leq 2 \\ 0 & \text{for } d > 2 \end{cases}, \tag{2.1}$$

with $d = |\vec{r}-\vec{r}_a|/h_a$.

For a given kernel function, a physical quantity A can be evaluated at any point in space $\vec{r}$ using the smoothing operator (see e.g. [367, 368, 369, 306])

$$\langle A(\vec{r})\rangle = \int A(\vec{r}')W(|\vec{r}-\vec{r}'|, h)d^3r' \,. \tag{2.2}$$

For a finite number of particles, this integral can be approximated by a sum, i.e.

$$\langle A(\vec{r})\rangle \approx \sum_a V_a A(\vec{r}_a) W(\vec{r}-\vec{r}_a, h_a) \,, \tag{2.3}$$

where V_a represents a volume associated with the particle at $\vec{r}_a$. Clearly, only particles with a non-zero kernel function at the position $\vec{r}$ contribute to this sum.

A main advantage of the SPH approach is that by using integration by parts in Eq. (2.2), spatial derivatives can be expressed as derivatives of the kernel function. For example, gradients can be evaluated with

$$\nabla A(\vec{r}) = \sum_a V_a A(\vec{r}_a) \nabla W(\vec{r} - \vec{r}_a, h_a) \; . \tag{2.4}$$

Since the kernel function is known and differentiable, these expressions can be evaluated directly without the need of finite differentiating techniques.

Using the SPH method, the code solves the equations of general relativistic hydrodynamics. These are based on the Valencia formulation [370, 303] with so-called conserved quantities, namely the conserved rest-mass density ρ^*, the conserved specific momentum $\hat{u}_i$, and the conserved energy density τ. These conserved quantities are related to the primitive variables rest-mass density ρ, coordinate velocity v^i, and specific internal energy ϵ via

$$\rho^* = \rho \alpha u^0 \psi^6, \tag{2.5}$$

$$\hat{u}_i = h u_i = h(v^i + \beta^i)\psi^4 u^0, \tag{2.6}$$

$$\tau = hW - \frac{P}{\rho W} - \omega, \tag{2.7}$$

with $\omega = \sqrt{1 + \frac{\hat{u}_i \hat{u}_j \delta^{ij}}{\psi^4}}$, the Lorentz factor $W = \alpha u^0 = (1 + \gamma^{ij} u_i u_j)^{1/2}$, the relativistic enthalpy $h = 1 + \epsilon + \frac{P}{\rho}$ (not to be confused with the smoothing length of a particle h_a) and the pressure P. α, β^i and ψ are metric potentials introduced below in Eqs. (2.12) and (2.13), $\gamma_{ij} = \psi^4 \delta_{ij}$ is the spatial part of the spacetime metric and δ_{ij} refers to the Kronecker delta. With these conserved quantities, the volume associated with each particle can be approximated as $V_a = m_a / \rho^*_a$, where m_a is the rest-mass of particle a.

The term "conserved quantity" stems from the structure of the hydrodynamic equations taking the form of a continuity equation,

$$\partial_t U + \nabla F(U) = S \; , \tag{2.8}$$

with a state vector of conserved variables U, a flux vector $F(U)$ and a source vector S. The main advantage of formulating the equations in this way is that if a solution exists, the system will converge towards this solution even if discontinuities are present in the system, i.e. in the presence of shocks [305].

For the set of chosen conserved quantities, the evolution equations comoving with the fluid are given by [371, 362, 21, 372]

$$\frac{d\rho^*}{dt} = - \rho^* \partial_i v^i, \tag{2.9}$$

$$\frac{d\hat{u}_i}{dt} = - \frac{\alpha \psi^6 \partial_i P}{\rho^*} - \alpha \hat{u}^0 \partial_i \alpha + \hat{u_j} \partial_i \beta^j + \frac{2 \hat{u}_k \hat{u}_k \partial_i \psi}{\psi^5 \hat{u}^0}, \tag{2.10}$$

$$\begin{aligned} \frac{d\tau}{dt} = & - \frac{\psi^6 (v^i + \beta^i)}{\rho^*} \left(1 - \frac{wW}{\omega}\right) (\partial_i P) - \frac{\psi^6 P \partial_i (v^i + \beta^i)}{\rho^*} \\ & - \frac{6 \psi^5 P (v^i + \beta^i)}{\rho^*} (\partial_i \psi) - \frac{\hat{u}_i}{\psi^4} \left(1 - \frac{wW}{\omega}\right) (\partial_i \alpha) \\ & - \frac{1}{\psi^4} \left(\frac{1}{\omega} - \frac{1}{wW}\right) \left(\hat{u}_i \hat{u}_j \partial_j \beta^i - \frac{1}{3} \hat{u}_i \hat{u}_i \partial_j \beta^j\right) \; , \end{aligned} \tag{2.11}$$

with $\frac{d}{dt} = \partial_t + v^i \partial_i$. Note that Eq. (2.11) slightly differs from the form given in the references [362] and [21]. However, this formulation is mathematically equivalent and the set of equations presented here shows improved numerical stability [372]. Neutrinos and magnetic fields are not included.

By employing the SPH scheme, all spatial derivatives of Eqs. (2.9)-(2.11) can be directly evaluated using the kernel function as described earlier. This reduces the evolution equations for ρ^*, $\hat{u}_i$ and τ to explicit, ordinary differential equations. These are then integrated in time employing a fourth-order Runge-Kutta method with an adaptive time step size to obey the Courant–Friedrichs–Lewy condition [373]. Note that for a given set of primitive variables, the conserved variables can be calculated directly using Eqs. (2.5)-(2.7). The reverse however, cannot be done analytically. To recover the primitive variables, Eqs. (2.5)-(2.7) have to be inverted numerically with a root-finding algorithm during the simulation. For this we employ a fixed point iteration method.

Additionally, to close the system, an equation of state (EoS) $P(\rho, \epsilon, Y_e)$ has to be provided. The code supports fully temperature- and composition-dependent three dimensional EoSs tables. Non-tabulated values are inferred using linear interpolation from neighboring points. The electron fraction Y_e of each SPH particle is determined from cold, neutrinoless beta-equilibrium during the initial setup. The values are then advected in the merger simulation, hence the dynamic timescales of the simulation are assumed to be short compared to the timescales of weak processes.

The code also supports the usage of barotropic EoSs tables, i.e. EoSs at zero temperature in neutrinoless beta-equilibrium composition where the pressure only depends on density. In this case, thermal pressure is added via the approximate ideal-gas treatment (see Sect. 2.2 for details). When barotropic EoSs are used, Y_e of each particle is set to the respective value of beta-equilibrium composition depending on the density.

To include shocks, an additional time-dependent artificial viscosity scheme is employed when two particles approach each other by treating them as two sides of a one-dimensional Riemann problem [374, 375]. This results in additional contributions to the conserved specific momentum and the conserved energy density equations. Details can be found in Ref. [21]. We use this scheme together with the approach proposed in Ref. [376] to reduce the viscosity in pure shear flows with no compression.

In addition to evolving the conserved quantities, the effects of gravity need to be included. In contrast to Newtonian gravity, general relativity cannot be treated within the SPH formalism. Therefore, the simulation code solves the Einstein field equations separately. These equations are expressed in the so-called Arnowitt-Deser-Misner (ADM) formalism [377], which is the standard formulation used in numerical relativity today, see e.g. [301, 302, 304, 305] for more information on this method and the derivation of equations. The main idea is to foliate the four-dimensional spacetime into spacelike, non-interacting, 3-dimensional hypersurfaces parameterized by a global time coordinate. Having a global time coordinate is essential for numerical simulations as it allows to evolve the entire system simultaneously in the time. With this approach, the Einstein field equations split up into a set of constraint and evolution equations.

The line element within this formalism is then given by,

$$ds^2 = (-\alpha^2 + \beta_i \beta^i) dt^2 + 2\beta_i dx^i dt + \gamma_{ij} dx^i dx^j \ , \tag{2.12}$$

with the lapse function α, the shift vector β^i and the three dimensional spatial metric part γ_{ij}. Additionally, we employ the so-called conformal flatness condition (CFC) [317, 318] assuming that γ_{ij} can be expressed as

$$\gamma_{ij} = \psi^4 \delta_{ij} \ . \tag{2.13}$$

The potential ψ is called the conformal factor. The CFC approximation greatly simplifies the task of solving the Einstein equations while still keeping the essential features of general relativity. Defining two additional potentials B^i and χ via

$$\beta^i = B^i - \frac{1}{4}\partial_i \chi \ , \tag{2.14}$$

the field equations take the following form of coupled, Poisson-like, elliptical partial differential equations with non-compact source terms

$$\Delta\psi = -2\pi\psi^5 E - \frac{\psi^5 K_{ij}K^{ij}}{8}, \tag{2.15}$$

$$\Delta(\alpha\psi) = 2\pi\alpha\psi^5(E+2S) + \frac{7\alpha\psi^5 K_{ij}K^{ij}}{8}, \tag{2.16}$$

$$\Delta B^i = 16\pi\alpha\rho W\hat{u}_i + 2\psi^{10}K^{ij}\partial_j\left(\frac{\alpha}{\psi^6}\right), \tag{2.17}$$

$$\Delta\chi = \partial_i B^i, \tag{2.18}$$

with $E = \rho w W^2 - P$ and $S = \rho w(W^2-1) + 3P$. The extrinsic curvature of a hypersurface K_{ij} is given by

$$K_{ij} = \frac{\psi^4}{2\alpha}\left(\delta_{ij}\partial_j\beta^l + \delta_{jl}\partial_i\beta^l - \frac{2\delta_{ij}\partial_k\beta^k}{3}\right). \tag{2.19}$$

Note that both α and β^i entirely depend on the chosen gauge condition. For the derivation of Eqs. (2.15)-(2.18), the so-called maximal slicing gauge condition $tr(K_{ij}) = 0$ was used. See e.g. [378] for details.

These equations determine the metric potentials at a fixed time coordinate for given matter source terms. In each timestep, the matter distribution is mapped from the particles onto a three-dimensional cubic grid covering the binary. On this grid, the field equations are discretized and solved with a full multigrid method (see e.g. [379]). Then, the metric potentials are mapped back onto the particles and the system is evolved in time by solving the hydrodynamic equations. A multipole expansion in spherical harmonics is used to calculate the boundary conditions on the metric grid, as well as the values of the metric potentials for particles that have moved outside the grid. This means that the evolution of the system is exclusively calculated on the SPH particle level and the metric is determined by repeatedly solving an effective initial value problem.

A downside of using the CFC approximation is that its structure of the metric does not include gravitational waves (GWs) by construction. Therefore, an additional backreaction scheme to mimic the effects of gravitational radiation on the systems and to extract the GW signal is needed. This is done following ideas from [380, 381] by adding a small, non-conformally flat contribution to the metric leading to the following three additional elliptic equations that need to be solved simultaneously with the CFC equations

$$\Delta U_5 = -4\pi\sigma \ , \tag{2.20}$$

$$\Delta R = -4\pi I^{[3]}_{ij} x^i \partial_j \sigma \ , \tag{2.21}$$

$$\Delta U_7 = -4\pi\rho^*(I^{[3]}_{ij}x^i\partial_j U_5 - R) \ . \tag{2.22}$$

The additional terms to the metric then read

$$h_{00} = -\frac{4}{5}(1-2U_5)(I_{ij}^{[3]}x^i\partial_j U_5 - R) - \frac{8}{5}U_7 \,, \tag{2.23}$$

$$h_{ij} = -\frac{4}{5}I_{ij}^{[3]} \,, \tag{2.24}$$

with $\sigma = T^{00} + T^{ii}$. $T^{\mu\nu}$ is the energy-momentum tensor and the quadrupole I_{ij} is given by [380]

$$\begin{aligned} I_{ij} = \int \rho^* \Bigg[& x^i x^j \left(1 + \frac{v^i v^i}{2} - U + \epsilon\right) + \frac{11}{21}x^i x^j v^i v^j - \frac{4}{7}x^i x^k v^j v^k \\ & + \frac{4}{21}v^i v^i x^i x^j + \frac{11}{21}x^i x^j x^i \partial_j U - \frac{17}{21}x^i x^j x^k \partial_k U \Bigg] \,. \end{aligned} \tag{2.25}$$

Here, U is the Newtonian gravitational potential.

The first time derivative $I_{ij}^{[1]}$ is calculated analytically, where the total time derivatives of U, $\partial_i U$ and $v^i v^i$ are neglected. The second and third time derivative are then calculated numerically on the fly with a finite difference approach. The backreaction scheme can also be turned off and back on again at any time during the simulation. Generally, this combination of CFC and approximate GW treatment reproduces results from fully general relativistic simulations well (see e.g [44, 382, 383, 384]).

The initial setup is provided by solving the TOV equations with the barotropic EoS slice. The stars are then placed on spherical orbits. Hence, the simulation starts with cold, irrotational stars in beta-equilibrium composition. In all simulations in this work, an initial center-to-center separation of 26 (≈38 km) is chosen if not specified otherwise. The systems is then relaxed for a short amount of time without the backreaction scheme but with an additional damping force to move SPH particle distribution towards an equilibrium configuration. The angular velocity of the system is constantly adjusted to keep the stars on a spherical orbit during the relaxation. If the distance between the stars grows, the angular is reduced and if the stars approach each other the angular velocity is increased. Over the course of this thesis some adjustments where made to this initial relaxation phase. These are presented in Appendix. A.

The simulation code is written in the programming language Fortran and parallelized with OpenMP. Additional reduction clauses are used to make results reproducible when running on the same CPU with the a constant number of threads.

2.2. Approximate thermal treatments, the ideal gas approach

As outlined in Sect. 1.2, many EoSs only exist as barotropic EoSs, i.e. at zero temperature and beta-equilibrium composition. This applies to microphysical models, but is especially true for parametric EoS descriptions such as piecewise polytropic [133] or constant speed of sound models [134]. When performing neutron star merger simulations, thermal effects are important as temperatures can reach several tens of MeVs. Therefore, approximate treatments to capture these effects need to be employed for barotropic EoSs. A commonly used effective scheme is the so-called ideal-gas approach from Ref. [333]. Here, the specific internal energy ϵ and the pressure P are split into a cold and a thermal contribution.

$$P = P_{\text{cold}}(\rho) + P_{\text{th}} \tag{2.26}$$

$$\epsilon = \epsilon_{\text{cold}}(\rho) + \epsilon_{\text{th}} \tag{2.27}$$

P_{cold} and ϵ_{cold} are assumed to only depend on the density ρ and are given by the EoS model. The total specific internal energy ϵ is inferred by evolving the hydrodynamic equations, therefore directly providing ϵ_{th}. Then, for the thermal pressure contribution, an ideal-gas like behavior is assumed,

$$P_{\text{th}} = (\Gamma_{\text{th}} - 1)\rho\epsilon_{\text{th}} \,, \tag{2.28}$$

where Γ_{th} is called the ideal-gas index. Hence, this treatment is also referred to as "Γ_{th} approach". We stress again that this approach uses ϵ_{th} and not the temperature of the system as ϵ_{th} is the quantity directly inferred from the hydrodynamic equations.

For available general purpose EoSs, Γ_{th} can vary between roughly 4/3 and 8/3 [385] and depends on temperature and density. Despite this variation, Γ_{th} is usually assumed to be constant when employing this approach in merger simulations. Comparisons with available fully temperature and composition-dependent nucleonic EoSs have shown that values of $\Gamma_{\text{th}} \approx 1.75$ are able to reproduce general features of mergers with sufficient accuracy [22]. Therefore, this thermal treatment has been employed in several merger simulations (e.g. [45, 47, 52, 319, 320, 321, 323, 53, 324, 29, 325, 327, 326]).

When we employ the ideal-gas approach in this thesis, we do not consider the evolution of the electron fraction Y_e. This means that we effectively assume matter to be in cold beta-equilibrium composition at all densities and temperatures. Any composition effects on the finite temperature EoS are neglected.

3. Neutron star matter equation of state models

As discussed in the introduction, the equation of state (EoS) is a key ingredient for the physics of neutron stars (NSs) and neutron star mergers. Since the exact conditions in the cores of NSs are currently not easily accessible through terrestrial experiments, our knowledge on the EoS remains somewhat limited. While different theoretical, experimental and observational constraints exist (see Sect. 1.2.1 for details), there remains some ambiguity on the true EoS of dense matter. In this section, we provide an overview on the different EoS models we employ in this thesis to resemble this ambiguity.

We start by introducing the necessary equations to calculate NS properties for an EoS model, namely the mass-radius curve and the tidal deformability. Then we discuss three different EoS samples, models containing nucleonic matter, models with nucleons and hyperons and hybrid models featuring a first-order phase transition from nucleonic to deconfined quark matter. All models we present in this section are general purpose EoSs also including leptons and photons and covering a wide range of densities, temperatures and electron fractions.

3.1. Calculating neutron star properties from the equation of state

For a given EoS, properties of NSs need to be calculated within the framework of general relativity (GR). The resulting stellar structure equations assuming spherically symmetric stars in hydrostatic equilibrium are the so-called Tolman-Oppenheimer-Volkoff equations [135, 136]

$$\frac{dm}{dr} = 4\pi r^2 e \tag{3.1}$$

$$\frac{dP}{dr} = -\frac{me}{r^2}\left(1+\frac{P}{e}\right)\left(1+\frac{4\pi r^3 P}{m}\right)\left(1-\frac{2m}{r}\right)^{-1} . \tag{3.2}$$

The derivation of these equations can be found in any standard general relativity textbook, e.g. [386]. Here, r is the radial coordinate, m is the gravitational mass contained in a sphere of radius r, P the internal pressure of matter and e the total energy density. Together with the EoS ($P(e)$) the TOV equations can be solved by picking a central density and integrating outwards until the pressure drops to zero. The corresponding radial coordinate R is the circumferential eigen radius of the NS and the mass contained within this radius is the gravitational NS mass M. Throughout this thesis, we will refer to R as the neutron star radius and M as the neutron star mass. By solving the TOV equations for several different central densities, one obtains the mass-radius (MR) curve of NSs. A simultaneous measurement of mass and radius of a NS can hence provide direct constraints on the EoS (see Sect. 1.2.1).

Additional constraints on the EoS can be inferred by studying the response of neutron stars in external gravitational fields, e.g. tidal fields from companions. To linear order, the quadrupole Q_{ij} induced by an external tidal field $\mathcal{E}_{ij}$ is given by

$$Q_{ij} = -\lambda \mathcal{E}_{ij} , \tag{3.3}$$

with the so-called tidal deformability λ

$$\lambda = \frac{2}{3} k_2 R^5 \ , \tag{3.4}$$

where k_2 is the tidal love number [36, 37]. A commonly used related quantity is the dimensionless tidal deformability

$$\Lambda = \frac{2}{3} k_2 \frac{R^5}{M^5} = \frac{2}{3} k_2 C^{-5} \tag{3.5}$$

with the stellar compactness $C = M/R$. Throughout this thesis, we will refer to the dimensionless quantity Λ as the tidal deformability.

The tidal love number can be calculated for a given EoS model by solving the differential equations (see [36, 37, 38] for details)

$$\frac{\mathrm{d}H(r)}{\mathrm{d}r} = \beta(r) \ , \tag{3.6}$$

$$\begin{aligned} \frac{\mathrm{d}\beta(r)}{\mathrm{d}r} = {} & 2\left(1-2\frac{m}{r}\right)^{-1} H(r)\left[-2\pi\left(5e+9p+\frac{e+p}{\mathrm{d}p/\mathrm{d}e}\right)+\frac{3}{r^2}+2\left(1-2\frac{m}{r}\right)^{-1}\left(\frac{m}{r^2}+4\pi r p\right)^2\right] \\ & + \frac{2\beta(r)}{r}\left(1-2\frac{m}{r}\right)^{-1}\left[\frac{m}{r}+2\pi r^2(e-p)-1\right] \ . \end{aligned} \tag{3.7}$$

These equations for $H(r)$ and $\beta(r)$ can be integrated outwards alongside the TOV equations starting just outside the center with $H(r) = a_0 r^2$ and $\beta(r) = 2a_0 r$. Here, a_0 is a constant that can be chosen freely as it cancels for determining k_2. With the definition

$$y = \frac{R\beta(R)}{H(R)} \ , \tag{3.8}$$

k_2 is given by [38]

$$\begin{aligned} k_2 = {} & \frac{8C^5}{5}(1-2C)^2[2+2C(y-1)-y]\Big\{2C[6-3y+3C(5y-8)] \\ & + 4C^3[13-11y+C(3y-2)+2C^2(1+y)]+3(1-2C)^2[2-y+2C(y-1)]\ln(1-2C)\Big\}^{-1} \ . \end{aligned} \tag{3.9}$$

Solving Eqs. (3.5)-(3.9) for different central densities yields an $M-\Lambda$ curve for a given EoS model. Inferring Λ and M simultaneously, e.g. from an inspiral gravitational-wave (GW) signal of a neutron star binary [32, 57, 150], provides information on the NS EoS complementary to the mass-radius measurements. Note that in GW detections, the inferred parameter is the so-called combined tidal deformability $\tilde{\Lambda}$ of the entire system

$$\tilde{\Lambda} = \frac{13}{16}\frac{(M_1+12M_2)M_1^4\Lambda_1+(M_2+12M_1)M_2^4\Lambda_2}{(M_1+M_2)^5} \tag{3.10}$$

where the subscript indicates the masses and tidal deformabilities of the individual stars. For equal mass binaries $\tilde{\Lambda}$ is identical to the tidal deformabilities of the individual stars, i.e. $\Lambda_1 = \Lambda_2 = \tilde{\Lambda}$.

3.2. Nucleonic EoS sample

In this section, we present all EoS models employed in this work that consider protons, neutrons and nuclei as relevant degrees of freedom. Electrons and photons are also included, generally on the levels of ideal Fermi- and Bosegases, respectively. We include EoSs based on both phenomenological and ab-initio approaches.

3.2.1. Phenomenological models

A commonly employed, phenomenological scheme in modeling baryon interactions is the so-called relativistic mean-field (RMF) approach [107, 108]. It is based on an effective Lagrangian density, where the interactions between baryons are described by meson exchange. From this Lagrangian, the field equations for nucleons and mesons are derived. Thermodynamic quantities can be inferred from Fermi-Dirac distribution functions. The couplings of mesons to baryons are chosen by fitting overall properties of nuclear matter, e.g. the saturation density as well as masses and radii of nuclei. Within the RMF framework, we consider two different types of RMF interactions, models with constant and approaches with density-dependent baryon-meson couplings. We employ the EoSs FSU2R [387], SFHo [30, 31], SFHx [30, 31], TM1 [388, 389] and TMA [390, 389], which assume constant meson-baryons couplings. These models generally differ in interaction terms included in the Lagrangian density, details can be found in the provided references. Additionally, we include the EoSs DD2 [391, 30], DD2F [391, 392] and GS2 [393], which employ density-dependent couplings [394].

In the EoSs DD2, DD2F, SFHo, SFHx, TM1 and TMA, the respective nucleon-nucleon interactions are employed with the extended nuclear statistical equilibrium approach of Ref. [30]. At low densities, this scheme includes an ensemble of light and heavy nuclei and a gas of unbound nucleons. The nuclei are treated as an ideal Boltzmann gas. Interactions between nuclei and free nucleons are mimicked using the excluded volume correction. The change in nuclear binding energies due to the coulomb screening by the electron gas is also accounted for by using so-called Wigner-Seitz cells [395]. To model the transition from the inhomogeneous matter in the neutron star crust to homogeneous matter in the core, matching pressure with local charge neutrality and equal proton fractions in both phases is required. The GS2 model employs a virial expansion of the grand canonical partition function at low densities assuming a non-ideal gas of neutrons, protons, alpha particles and heavy nuclei (see [396] for details). This is then smoothly connected to the high density RMF calculations of [397]. For the FSU2R model, the EoS is matched to the low density part of the DD2 EoS using linear interpolation of thermodynamic quantities between 0.03 fm^{-3} and 0.10 fm^{-3}.

Further popular phenomenological approaches in EoS calculations are models based on Skyrme interactions [109, 110, 111, 112] between nucleons. These are non-relativistic models based on effective density-dependent contact interactions that are fitted to reproduce properties of nuclei. Thermodynamic quantities are then determined from the minimized free energy of the system. We employ the skyrme-based models LS220, LS375 from [398] and the SLy4 EoS of [399] in this thesis. Additionally, we include the skyrme-based EoSs “Fiducial”, “Large Mmax”, “Large SL”, “Large R”, “Small SL” and “Smaller R” from Ref. [400], we refer to these models as DHS F, DHS LM, DHS LSL, DHS LR, DHS SSL and DHS SR, respectively.

The two models LS220 and LS375 employ the so-called single nucleus approximation (SNA) for inhomogeneous matter which considers alpha particles and a representative heavy nucleus instead of a full distribution of nuclei alongside the free nucleons. This single nucleus is treated within

Table 3.1.: Properties of cold stars for the sample of purely nucleonic EoSs considered in this work. Second to fifth column provide the maximum mass $M_{\rm max}$, the radius $R_{1.4}$ and tidal deformability $\Lambda_{1.4}$ of a $1.4\ M_\odot$ neutron star and the tidal deformability $\Lambda_{1.75}$ of a $1.75\ M_\odot$ neutron star. Table adapted from Ref. [360].

EoS	$M_{\rm max}$ [$M_\odot$]	$R_{1.4}$ [km]	$\Lambda_{1.4}$	$\Lambda_{1.75}$	Ref.
APR	2.20	11.57	267.6	54.5	[401, 402]
DD2	2.42	13.22	698.8	178.5	[391, 30]
DD2F	2.08	12.40	425.5	79.3	[391, 392]
DSH F	2.17	11.73	296.3	61.8	[400]
DSH LM	2.22	12.65	513.9	119.9	[400]
DSH LSL	2.16	11.76	271.5	55.9	[400]
DSH LR	2.13	12.44	437.6	87.3	[400]
DSH SSL	2.18	11.70	335.8	70.3	[400]
DSH SR	2.14	11.29	233.1	48.8	[400]
FSU2R	2.06	12.87	640.8	143.5	[387]
FTNS	2.22	11.46	304.8	65.3	[403, 404]
GS2	2.09	13.60	721.3	160.6	[393]
LPB	2.10	12.37	429.9	79.9	[405, 406]
LS220	2.04	12.96	541.9	94.2	[398]
LS375	2.71	13.95	960.1	257.7	[398]
SFHo	2.06	11.89	333.5	63.5	[30, 31]
SFHx	2.13	11.98	395.1	86.7	[30, 31]
SLy4	2.05	11.72	303.7	54.7	[407, 399]
TM1	2.21	14.47	1149.0	257.7	[408, 409]
TMA	2.01	13.79	929.1	184.1	[390, 30]

a finite-temperature liquid drop model and interactions between unbound nucleons and nuclei are mimicked with the excluded volume correction. The free energy density of alpha particles is calculated using a Maxwell-Boltzmann expression of a classical ideal gas. A Maxwell construction models the transition from homogeneous to inhomogeneous matter.

The SRO scheme of Ref. [399] uses a similar approach as [398] employing the SNA with some improvements such as more accurate values of alpha particle binding energies. In this approach, the transition from inhomogeneous to homogeneous matter is performed at a density where both phases have equal free energies. The SRO scheme was designed to be employed with Skyrme interactions. In this work, we use the EoS table calculated with the SLy4 parameterization of [407].

The parametric EoS framework of [400] aims to quantify how uncertainties in nucleon-nucleon interactions propagate throughout the EoS. Different tables can be calculated by choosing different sets of parameters. For this, the Skyrme interactions of [410] are employed, which are fitted to current calculations from chiral effective field theory and binding energies of nuclei. As for several of our RMF based EoSs, these interactions are employed within the framework of [30] to describe matter at low densities. The tables we employ in this thesis are pre-computed and provided in the online repository [1].

[1] https://neutronstars.utk.edu/code/eos/

3.2.2. Ab-initio models

Besides phenomenological approaches, we also employ ab-initio models. These are based on bare two- and three-nucleon interactions that reproduce results from nucleon-nucleon scattering experiments and properties of light nuclei. An example is the APR [401] EoS, which starts from a Hamiltonian employing the Argonne V18 two body-potential [119], the Urbana IX three nucleon-interaction [118, 120] and the relativistic boost interaction $\delta\nu$ [401, 11, 411]. In [401] the EoS is then calculated using a variational approach for the ground state energy at zero temperature in beta-equilibrium composition. An interesting result from this calculation is that the EoS features a neutral pion condensate at supranuclear densities. In this work, we employ the APR version of Ref. [402]. Here, the original APR EoS was extended to finite temperatures and different proton fractions using the aforementioned SRO scheme of Ref. [399]. This scheme was modified in [402] to employ the APR potentials instead of a Skyrme parameterization to construct a general purpose APR version.

Another ab-initio model is the FTNS EoS [404]. This model also starts from a non-relativistic Hamiltonian including the Argonne V18 two body-interaction [119] as well as the Urbana IX three nucleon-potential [118, 120]. The EoS is calculated using the cluster variational method of [126]. In Ref. [404], non-uniform matter was treated with the SNA, the EoS we employ however uses the approach of Ref. [403], which accounts for a wide distribution of heavy and light nuclei. Heavy nuclei are treated within a liquid drop approximation with several corrections such as electron screening as well as phenomenological temperature- and density-dependent corrections to surface and shell energies. For light nuclei, binding energies are explicitly computed from experimental data with phenomenological terms accounting for interactions with unbound nucleons, Coulomb screening by the electron gas and Pauli energy shifts. These phenomenological corrections allow for a smooth transition between the inhomogeneous and homogeneous phase of matter.

The final ab-initio EoS we use in this work is the LPB model of Ref. [406], which is an extension of the cold EoS of Ref. [405] to finite temperatures. The nucleon interactions are taken directly from recent chiral effective field theory (χEFT) calculations. The two-body interaction is determined at next-to-next-to-next-to-leading order expansion in [412] and the three-body potential is inferred at next-to-next-to-leading order in [413]. The EoS is calculated in Ref. [406] within the Brueckner-Bethe-Goldstone many body theory [414, 123, 124] using the so-called Brueckner-Hartree-Fock approximation to calculate the free energy of the system. At low densities, the EoS is matched to the TM1 EoS. All thermodynamic quantities are linearly interpolated between the high and low density EoSs in the density range from 0.05 fm^{-3} to 0.08 fm^{-3}.

In Fig. 3.1, we plot the mass-radius curves of all EoSs in the nucleonic sample. We see that that our sample includes stiff as well as soft models and covers a broad range of radii between roughly 10 km and 15 km. We summarize different properties of resulting NSs for these models in Table. 3.1. We remark, that the models GS2, LS375, TM1 and TMA are in tension with the symmetric 90% confidence intervals on the tidal deformability observation from GW170817 [32, 57] assuming low spin priors. All EoSs in the nucleonic sample reach maximum masses of two solar masses or more as required by current observations of heavy pulsars [139, 140]. However, the models DD2F, FSU2R, LS220, SFHo, and Sly4 are incompatible with the results of Ref. [149] suggesting the maximum TOV mass is larger than $2.09\ M_\odot$ at 3σ confidence interval. We still include all the EoSs conflicting with the aforementioned constraints to have a larger nucleonic EoS sample.

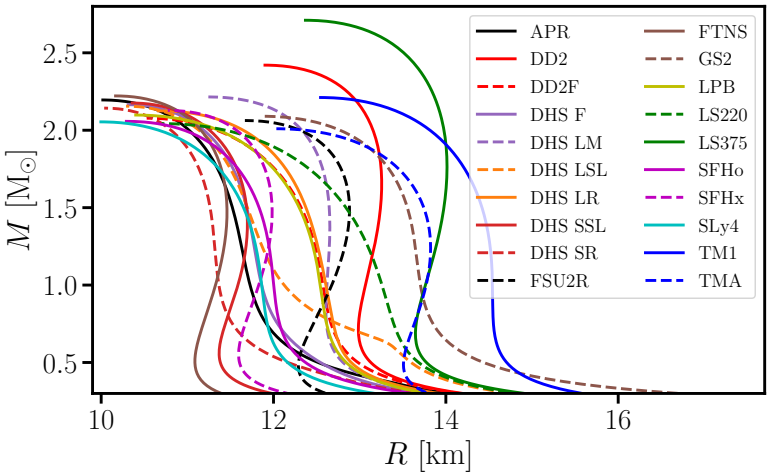

Figure 3.1.: Mass-radius curves of neutron stars for all equation of state models in the purely nucleonic sample.

3.3. Hyperonic EoSs

In this section, we present EoS models accounting for the presence of hyperons in neutron star matter. We include the models BHBΛΦ [207], DD2Y [208], DNS [415], FSU2H* [211], QMC-A [210], R(DD2YDelta)1.1-1.1 [212], R(DD2YDelta)1.2-1.1 [212], R(DD2YDelta)1.2-1.3 [212] and SFHoY [209]. All of these EoSs are based on the phenomenological relativistic-mean field approach (see Sec. 3.2.1), which now also includes strangeness. The hyperon content in all models is density- and temperature-dependent and the transition from nucleonic to hyperonic matter is smooth. Apart from BHBΛΦ, which only considers Λ baryons, all hyperonic EoSs in our sample consider the baryon octet of Λ, Σ and Ξ baryons. The three R(DD2YDelta) EoSs additionally account for the appearance of Δ-baryons. Note that the R(DD2YDelta)1.2-1.3 EoS is very similar to DD2Y at zero temperature.

The models BHBΛΦ, DD2Y as well as the three R(DD2YDelta) EoSs are based on the DD2 framework and employ the same treatment as this EoS for purely nucleonic matter. Similarly, the SFHoY models is based on the nucleonic SFHo EoS. For the FSU2H* EoS we additionally consider two alternative descriptions from [416] referred to as FSU2H*L and FSU2H*U with a lower/higher onset density of hyperons compared to FSU2H*. These are based on the same RMF approach as FSU2H*, but employ different values of the hyperonic potentials to effectively quantify how current uncertainties propagate to the EoS. See Ref. [416] for details.

The DNS EoS is based on the CMF model of Ref. [417]. The interactions in this model are inferred with a non-linear realization of the sigma model and restore chiral symmetry at high densities and/or temperatures. See [417, 415] for details. The QMC-A model differs from the other RMF EoSs presented so far as it relates the internal quark structure of hadrons to the RMFs of nuclear matter. For this, the interactions are considered self-consistently between valence quarks, which are confined in non-overlapping baryons and mesons. The couplings are chosen such that the model reproduces properties of symmetric nuclear matter. The dynamics of the quarks inside a baryon are used to model the effects of dense medium surrounding on the interaction. The confined quarks themselves are described with a bag model [210]. In this approach, the appearance of hyperons emerges naturally from the inclusion of strange quarks and requires no additional terms. For the

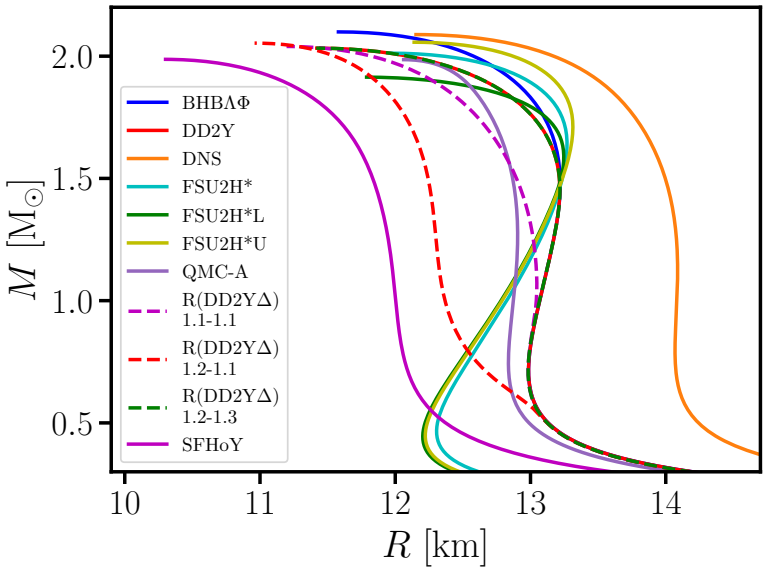

Figure 3.2.: Mass-radius curves of neutron stars for all equation of state models we employ in this thesis containing hyperons.

DNS, QMC-A and the three FSU2H* EoSs the low density part is modeled with the DD2 EoS. The low and high density matter descriptions are matched by using linear interpolation of thermodynamic quantities between 0.03 fm^{-3} and 0.10 fm^{-3}.

We show the mass-radius curves of all EoSs in the hyperonic sample in Fig. 3.2. We find considerable variation in NS radii within our sample. All models apart from FSU2H*L reach a maximum mass around $2\ M_\odot$. However, the maximum masses are generally smaller than those of the nucleonic sample (compare Fig. 3.1), which can be explained by the additional softening introduced by the hyperons. Only the models BHBΛΦ and DNS are compatible with the lower limit on the maximum mass of $2.09\ M_\odot$ set by Ref. [149] at the 3σ limit.

We summarize different properties of resulting NSs for hyperonic models in Table. 3.2. In particular, we provide the onset density of hyperons ρ_{onset} at zero temperature and in β-equilibrium composition and lowest NS mass containing hyperons for each model. Note that the tidal deformabilities resulting from the models DNS, FSU2H*, FSU2H*U and FSU2H*L are not compatible with the symmetric 90% confidence intervals on the tidal deformability observation from GW170817 [32, 57] assuming low spin priors. We still employ these models in this work to have a representative sample of different general purpose EoS with hyperons.

3.4. Hybrid EoS sample

In this work we use 7 relativistic-mean field, hybrid EoSs featuring a two-phase construction with first-order phase transition from hadronic to deconfined quark matter from Ref. [283]. We follow the labeling of Refs. [52, 53, 361] and refer to these EoSs as DD2F-SF-n with n $\in$\{1,2,3,4,5,6,7\}. The hadronic phase of all DD2F-SF models is given by the DD2F EoS (see Sect. 3.2). The quark phase is based on the phenomenological string-flip (SF) approach of Ref. [418]. In this scheme, quark confinement of up- and down-quarks is modeled with a density-dependent scalar self energy contribution to the effective quark masses leading to divergent effective masses at zero-densities.

Table 3.2.: Properties of cold stars for the sample of EoSs considered in this work which include hyperonic degrees of freedom. Second to fifth column provide the maximum mass M_{max}, the radius $R_{1.4}$ and tidal deformability $\Lambda_{1.4}$ of a $1.4\ M_\odot$ neutron star and the tidal deformability $\Lambda_{1.75}$ of a $1.75\ M_\odot$ neutron star. ρ_{onset} is the onset rest-mass density for the occurrence of hyperons in the $T = 0$, beta-equilibrium EoS slice and M_{onset} the lowest NS mass containing hyperons. Table adapted from Ref. [360].

EoS	M_{max} [$M_\odot$]	$R_{1.4}$ [km]	$\Lambda_{1.4}$	$\Lambda_{1.75}$	ρ_{onset} [ρ_{nuc}]	M_{on} [$M_\odot$]	Ref.
BHB$\Lambda\phi$	2.10	13.21	695.2	160.1	2.11	1.31	[207]
DD2Y	2.03	13.21	694.8	150.9	2.11	1.30	[208]
DNS	2.09	14.04	957.7	208.3	2.90	1.82	[415]
FSU2H*	2.01	13.18	778.8	192.1	2.14	1.45	[211]
FSU2H*L	1.91	13.16	784.4	177.6	2.11	1.44	[211, 416]
FSU2H*U	2.06	13.17	784.4	205.7	2.18	1.55	[211, 416]
QMC-A	1.99	12.89	574.8	126.0	3.50	1.86	[210]
R(DD2YΔ) 1.1-1.1	2.04	12.96	586.8	114.0	1.73	0.86	[212]
R(DD2YΔ) 1.2-1.1	2.05	12.27	397.3	85.4	1.39	0.50	[212]
R(DD2YΔ) 1.2-1.3	2.03	13.21	696.1	150.8	2.11	1.29	[212]
SFHoY	1.99	11.89	333.6	61.9	3.65	1.59	[209]

Deconfinement is treated with a Gaussian functional resulting in a medium-dependent reduction of the string tension between quarks. Higher-order repulsive vector fields are included in the pure deconfined quark phase to provide the necessary stiffness allowing for a maximum neutron star mass above $2\ M_\odot$. See [418, 283] for details.

The phase transition is modeled with a Maxwell construction by matching the pressure and chemical potential in both phases at fixed temperatures. Note that electrons are added to the EoS after the phase construction making the transition a property of strongly interacting matter only.

Within the SF model, different parameterizations can be chosen. This changes the properties of the deconfined quark phase as well as the onset density and density jump of the phase transition. The employed SF parameters of each EoS can be found in Refs [52, 283].

In Fig. 3.3(a), we plot the high-density part of all DD2F-SF EoS as well as the nucleonic DD2F model. We see that below the respective onset densities, the hybrid models are identical with the DD2F EoS. The only exception is the DD2F-SF-2 model, which employs slightly different parameters within the excluded volume correction (see [283]). The phase transition in each model can be clearly seen as a region of almost constant pressure, where both phases coexist. Our sample covers a range of onset densities between roughly $2 - 4 \times \rho_{\text{nuc}}$ and different sizes of the density jump.

Fig. 3.3(b) shows the resulting mass-radius curves of the EoSs. The onset of the phase transition leads to a visible kink in all curves bending them towards lower radii compared to the nucleonic DD2F EoS. Here, hybrid stars are more compact that nucleonic stars. At larger masses, the different parameterizations behave differently covering a range of hybrid star masses-radius configurations. Some models feature lower maximum masses and smaller radii than DD2F, but others allow for larger maximum masses and radii. We provide the maximum masses as well as the boundaries of

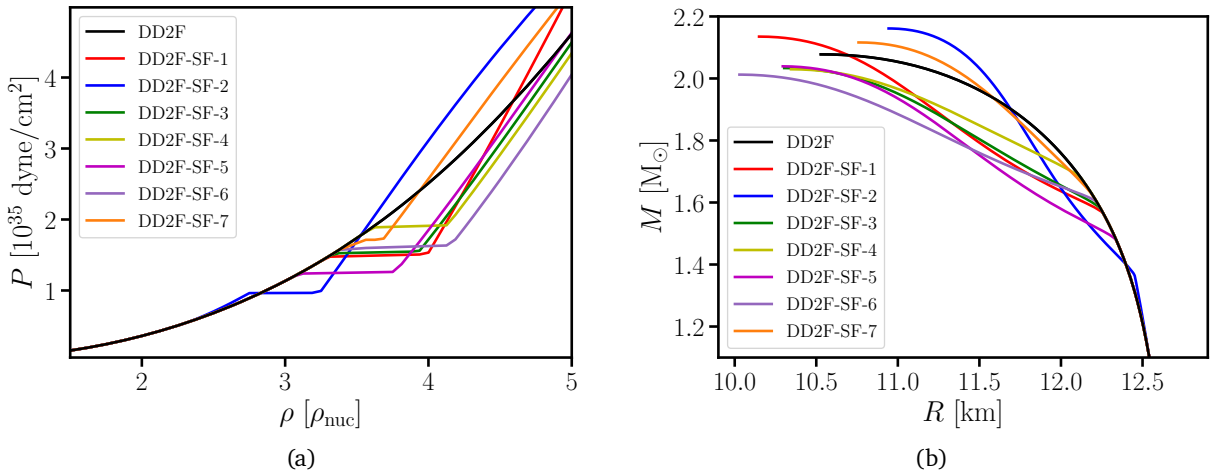

Figure 3.3.: (a): Pressure as a function of density for the nucleonic DD2F EoS (black) and all hybrid DD2F-SF models we employ in this work (colored). (b): Mass-radius curves of neutron stars for the EoS shown in (a). Both figures adapted from Ref. [52].

Table 3.3.: Properties of cold stars for the hybrid DD2F-SF EoSs sample. We provide the maximum mass $M_{\rm max}$, the smallest mass with deconfined quark matter present in the core $M_{\rm onset}$ and the phase boundaries $\rho_{\rm on,0}$ and $\rho_{\rm fin,0}$ in the $T = 0$, beta-equilibrium EoS slice.

EoS	$M_{\rm max}$ [$M_\odot$]	$M_{\rm on}$ [$M_\odot$]	$\rho_{\rm on,0}$ [$\rho_{\rm nuc}$]	$\rho_{\rm fin,0}$ [$\rho_{\rm nuc}$]
DD2F-SF-1	2.14	1.57	3.30	4.00
DD2F-SF-2	2.16	1.37	2.76	3.25
DD2F-SF-3	2.03	1.58	3.35	3.94
DD2F-SF-4	2.03	1.68	3.61	4.13
DD2F-SF-5	2.04	1.48	3.10	3.77
DD2F-SF-6	2.01	1.60	3.41	4.16
DD2F-SF-7	2.12	1.62	3.51	3.69

the coexistence phase and the lightest hybrid star for each model in Table 3.3.

All DD2F-SF EoS reach maximum masses of at least $2\ M_\odot$ and are compatible with current constraints on the tidal deformability from GW170817 [32, 57]. However, only the parameterizations DD2F-SF-1, DD2F-SF-2 and DD2F-SF-7 reach maximum masses in agreement with the suggested lower limit of $2.09\ M_\odot$ at 3σ confidence interval from Ref. [149].

The phase boundaries of all DD2F-SF models separating the nucleonic, the coexistence and the pure quark matter phase are temperature-dependent. In Fig. 3.4(a), we show how the onset of quark deconfinement (dashed lines) and the beginning of the pure quark matter phase (solid lines) vary with temperature. The Y_e values match those of cold beta-equilibrium composition at all densities. We see that with increasing temperature the coexistence region of all models is shifted towards lower densities and is also enlarged as the dashed lines generally show a larger temperature-dependence compared to the solid lines. Models with lower phase boundaries at $T = 0$ also tend to have lower boundaries at finite temperature. However, some lines cross in Fig. 3.4(a). In the

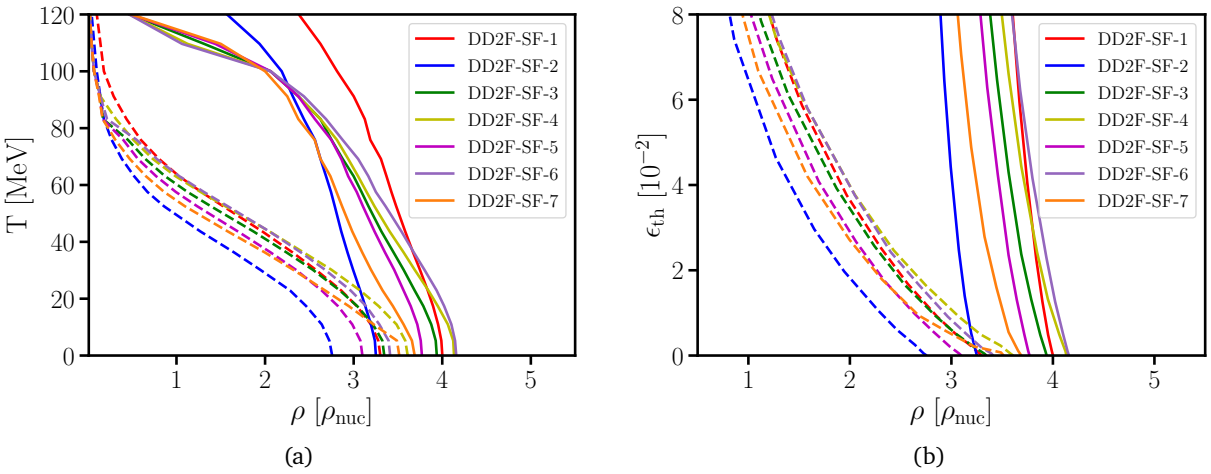

(a) (b)

Figure 3.4.: (a): Phase boundaries of the DD2F-SF-n EoSs [283] in the density-temperature plane. Different colors refer to different EoS models. The dashed lines display the onset of the coexisting phases whereas the solid lines mark the beginning of the pure quark matter regime for each hybrid model. (b): Same as (a) but in the density-ϵ_{th} plane, where ϵ_{th} is the specific thermal energy. Figure adapted from Ref. [361].

temperature range relevant for mergers (up to around 40 MeV to 60 MeV), the change of the phase boundaries is significant and the onset density can become as low as nuclear saturation density. This means that in a neutron star merger deconfined quark matter can be present at lower densities than in cold, isolated neutron star due to thermal effects.

As explained in Sect. 2.2, the specific thermal energy ϵ_{th} rather than the temperature is the relevant hydrodynamic quantity characterizing thermal effects in the neutron star simulations. Therefore, we also show the phase boundaries of all DD2F-SF EoS in the $\rho - \epsilon_{\mathrm{th}}$ plane in Fig. 3.4(b). Generally, the qualitative behavior of the boundaries is similar to the density-temperature plane although the exact shape of the curves is somewhat different.

4. Results: Impact of thermal effects in neutron star mergers for hybrid EoSs

In this chapter, we investigate the impact of finite temperature effects in neutron star mergers for hybrid EoSs, i.e. models that feature a first-order phase transition from hadronic to deconfined quark matter. We start by visualizing the effect the earlier onset of quark deconfinement has on the EoS model and demonstrate how this behavior is completely neglected by the commonly used ideal-gas approach. We then develop an extension of this scheme to correctly capture the effects of temperature-dependent phase boundaries. We test this new method and apply it to different hybrid EoS scenarios in neutron star merger simulations. The content of this chapter is based on the results published in Ref. [361].

4.1. Phase boundaries of hybrid EoSs at finite temperatures

One of the main assumptions of the approximate ideal-gas treatment for thermal effects discussed in Sect. 2.2 is that the thermal behavior of the EoSs is the same at all densities and temperatures. For EoSs featuring a phase transition to deconfined quark matter, this assumption breaks down as a sudden change in EoS properties is precisely the feature of a hybrid model. In particular, the two phases are expected to show different thermal behavior. Additionally, since a first-order phase transition is constructed by balancing pressure P and chemical potential μ of both phases at fixed temperatures and compositions

$$P_{\mathrm{H}}(\rho_{\mathrm{on}}, T, Y_e) = P_{\mathrm{Q}}(\rho_{\mathrm{fin}}, T, Y_e) \ , \tag{4.1}$$

$$\mu_{\mathrm{H}}(\rho_{\mathrm{on}}, T, Y_e) = \mu_{\mathrm{Q}}(\rho_{\mathrm{fin}}, T, Y_e) \ , \tag{4.2}$$

a shift in phase boundaries at finite temperatures is plausible due to the different thermal properties of nucleonic and deconfined quark matter. Here, ρ_{on} and ρ_{fin} mark the beginning and the end of the coexistence phase, respectively.

For the fully temperature- and composition-dependent DD2F-SF models we introduce in Sect. 3.4, such a shift does indeed occur. These models employ a two-phase description for the hadronic and the deconfined quark phases that are connected by a Maxwell construction. Fig. 4.1 shows the phase diagram of the DD2F-SF-1 EoSs in the density-temperature plane as a representative example. The different phases are highlighted with different colors and the dashed (solid) line mark the onset (end) of the coexistence phase. It is clear that at finite temperatures, the appearance of deconfined quark matter is shifted to lower densities. This is indicated in particular by the red color visualizing the enlargement of the pure deconfined quark matter phase at finite temperatures compared to the zero temperature case. Note that in this figure, the Y_e values match those of cold beta-equilibrium at every density and temperature.

The effects of these shifting phase boundaries are demonstrated in Fig. 4.2. The blue line shows the EoS slice at $T = 0$ while the red line depicts this EoS at $T = 30$ MeV. Both models have the same

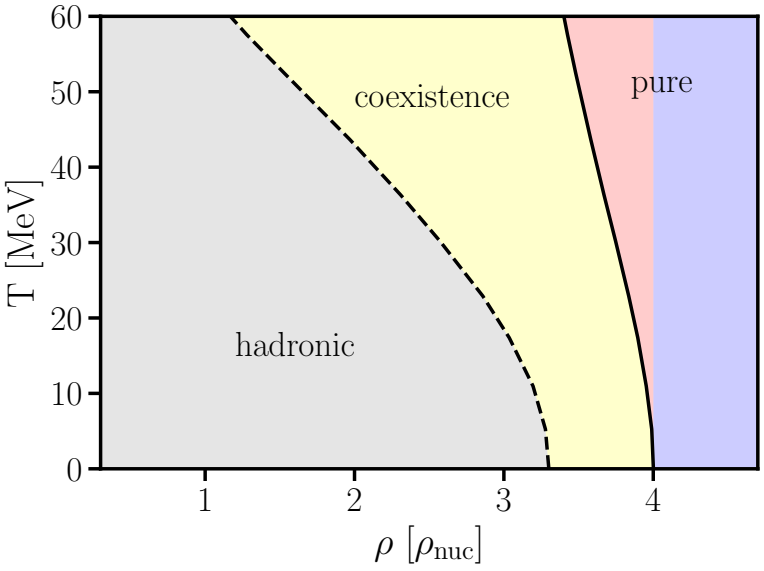

Figure 4.1.: Phase diagram of the DD2F-SF-1 EoS in the density-temperature plane. Different colors highlight different phases of matter. Black lines indicate the boundaries between these phases. The red colored region illustrates the increase of the pure quark phase at finite temperatures. At all densities and temperatures we pick the Y_e values of the barotropic EoS, i.e. those corresponding to cold, neutrinoless beta-equilibrium. Figure adapted from Ref. [361].

Y_e values at all densities. One can clearly see that in the finite temperature case the coexistence phase, visible as a region of almost constant pressure, has moved to lower densities and is also enlarged compared to the zero temperature case. This means that deconfined quark matter is already present at lower densities. The result is a significant reduction in pressure and a regime of effectively negative $P_{\rm th}$ (as defined by Eq. (2.26)) since the pressure at finite temperature P becomes lower than $P_{\rm cold}$.

The dashed green line shows the pressure one would infer using the ideal-gas approach with $\Gamma_{\rm th} = 1.75$ at all densities. It is apparent that this approach cannot capture the correct behavior of the DD2F-SF-1 EoS at finite temperatures. A large density region between roughly $2.57 \times \rho_{\rm nuc}$ and $4.00 \times \rho_{\rm nuc}$ exists, where the ideal-gas scheme significantly overestimates the pressure. We indicated this region by the red shading in Fig. 4.2.

At densities below the onset density at T=30 MeV, we find that the red line is approximated very well by the green curve. In this regime, the hot EoS remains in the hadronic phase where the ideal-gas approach is a good estimate. At large densities beyond $4.00 \times \rho_{\rm nuc}$, the green line also approximates the red line reasonably well, however the agreement is not as good as at lower densities. Here, the pressure is systematically slightly overestimated by the ideal-gas approach. At such high densities cold matter is already present at $T = 0$, hence there is no crossing into a different phase with increasing temperature. However, the deconfined quark matter behaves more similarly to an ultrarelativistic ideal Fermigas, where the thermal index is $\Gamma_{\rm th} = 4/3$. Picking $\Gamma_{\rm th} = 1.75$ thus results in slightly too large thermal pressures.

To conclude, for hybrid EoSs an increase in temperature at fixed density can lead to a change in phase, i.e. to a sudden shift of the thermal behavior. As the ideal-gas approach assumes a uniform

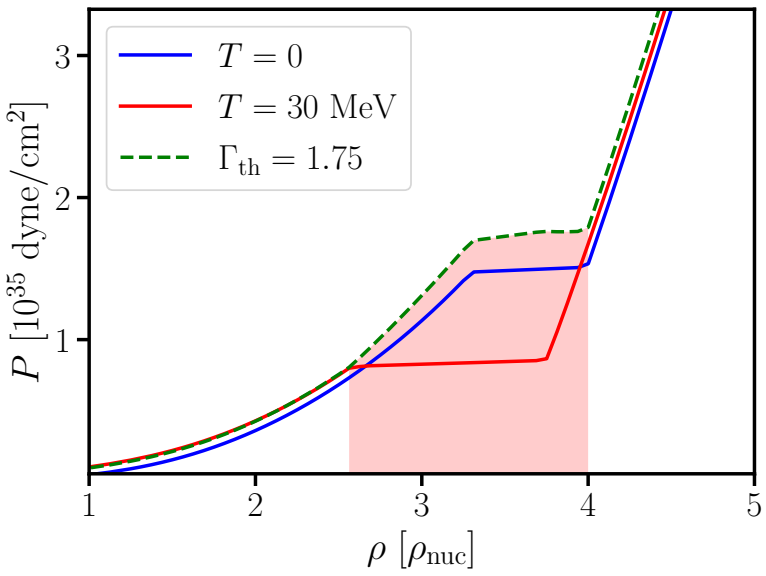

Figure 4.2.: Pressure as a function of density for the DD2F-SF-1 EoS at $T = 0$ (blue line) and $T = 30$ MeV (red line). The dashed green line indicates the pressure we would obtain by inferring the thermal pressure with the commonly used thermal ideal-gas approach of Eq. (2.28) with $\Gamma_{\rm th} = 1.75$ and thermal energies corresponding to $T = 30$ MeV. The highlighted region illustrates the density range where the ideal-gas approach significantly overestimates the pressure of the hot EoS. Figure adapted from Ref. [361]

thermal behavior across all densities and temperatures, it cannot correctly approximate the finite temperature part for hybrid EoSs. Also note that simply picking a different value of $\Gamma_{\rm th}$ in different density ranges is not sufficient, since this still effectively assumes constant phase boundaries with temperature. As the phase boundaries continuously vary with temperature, a fully density- and temperature-dependent extension of $\Gamma_{\rm th}$ is necessary to make this scheme viable for hybrid EoS models. We present such an extension in the next section.

4.2. Extending the ideal-gas approach to hybrid EoSs

In this section, we present an extension of the ideal-gas approach suitable for thermal effects of two-phase hybrid EoS models. We will refer to this scheme as effective phase transition (effPT) scheme.

As for the traditional approach, we calculate the thermal pressure from the specific thermal energy $\epsilon_{\rm th}$ rather than the temperature T since $\epsilon_{\rm th}$ is directly inferred from solving the hydrodynamic equations. The main idea is to use different descriptions for the thermal pressure at different densities depending on which phase of matter is present at $\epsilon_{\rm th} = 0$ and $\epsilon_{\rm th} > 0$. This requires knowledge of the phase boundaries $\rho_{\rm on}$ and $\rho_{\rm fin}$ as a function of $\epsilon_{\rm th}$ in addition to the boundaries $\rho_{\rm on,0}$ and $\rho_{\rm fin,0}$ at zero temperature. The task is to provide a reasonable approximation for the pressure at $\epsilon_{\rm th} > 0$ starting from a given cold EoS and knowledge of $\rho_{\rm on}$ and $\rho_{\rm fin}$ for the requested $\epsilon_{\rm th}$.

To illustrate the approach Fig. 4.3(a) shows the DD2F-SF-1 EoS at slices of constant $\epsilon_{\rm th}$. The blue line shows $\epsilon_{\rm th} = 0$ and the red line $\epsilon_{\rm th} = 0.03$. Additionally, the blue and red crosses mark the

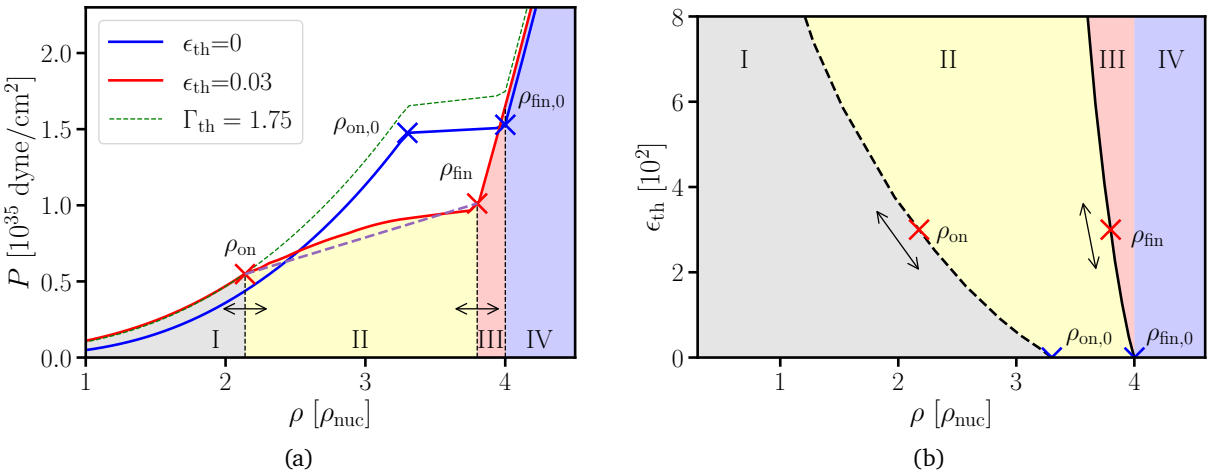

Figure 4.3.: (a): Pressure as a function of density for the DD2F-SF-1 EoS at $\epsilon_{\rm th} = 0$ (blue line) and at $\epsilon_{\rm th} = 0.03$ (red line). The purple, dashed line illustrates a linear interpolation between the phase boundaries at $\epsilon_{\rm th} = 0.03$. The green, dashed line displays the pressure we would obtain using the ideal-gas approach of Eq. (2.28) for $\epsilon_{\rm th} = 0.03$. (b): Phase diagram of the DD2F-SF-1 EoS in the density-$\epsilon_{\rm th}$ plane. In both panels, we highlight the different regimes as in Fig. 4.1. Each regime requires a different treatment by our effective procedure to include thermal effects. Blue and red crosses refer to the phase boundaries at $\epsilon_{\rm th} = 0$ and $\epsilon_{\rm th} = 0.03$, respectively. Arrows indicate how these boundaries change with $\epsilon_{\rm th}$. Both figures are adapted from Ref. [361].

boundaries of the coexistence phase for both cases, respectively.

Note that while $\epsilon_{\rm th} = 0$ is equivalent to $T = 0$ at all densities, $\epsilon_{\rm th} = 0.03$ corresponds to different temperatures at each density covering the range between roughly 40 MeV to 30 MeV for densities between $2 \times \rho_{\rm nuc}$ and $4 \times \rho_{\rm nuc}$. Hence, for a constant $\epsilon_{\rm th} = 0.03$ the coexistence phase is no longer a flat region of constant pressure but an almost linear function. For comparison, the dashed purple line shows the linear pressure-density relation between $\rho_{\rm on}$ and $\rho_{\rm fin}$.

The dashed green line illustrates the pressure we would obtain using Eq. (2.28) and $\epsilon_{\rm th} = 0.03$. Similar to Fig. 4.2 there is a large density range where this approach greatly overestimates the pressure. We identify four different regimes in Figure 4.3(a) that each require different treatments for the thermal pressure. We mark them in different colors and label them with roman numerals I-IV.

Regime I corresponds to densities below $\rho_{\rm on}$, where matter remains in the hadronic phase at $\epsilon_{\rm th} = 0.03$. Regime II contains matter in the coexistence phase at finite $\epsilon_{\rm th} = 0.03$, i.e. between $\rho_{\rm on}$ and $\rho_{\rm fin}$. In Regime III at densities between $\rho_{\rm fin}$ and $\rho_{\rm fin,0}$, matter changes from the coexistence phase at $\epsilon = 0$ to the pure deconfined quark phase at $\epsilon_{\rm th} = 0.03$. Finally, regime IV contains matter above $\rho_{\rm fin,0}$, where pure deconfined quark matter is already present at $\epsilon_{\rm th} = 0$. The origin of these regimes is further illustrated in Fig. 4.3(b). Here, we plot the corresponding EoS phase diagram in the $\rho - \epsilon_{\rm th}$ plane. As in Fig. 4.1, the dashed line displays the onset of quark deconfinement $\epsilon_{\rm th,on}(\rho)$ and the solid line the beginning of the pure quark phase $\epsilon_{\rm th,fin}(\rho)$.

The four regimes as well as the phase boundaries at $\epsilon_{\rm th} = 0.03$ and $\epsilon_{\rm th} = 0$ are highlighted in the same way as in Fig 4.3(a). Note that the borders between regime I and II as well as between

regime II and III depend on the value of ϵ_{th} and move along the phase boundaries as indicated by the arrows in Fig. 4.3(a) and Fig. 4.3(b). However, since $\rho_{\text{fin},0}$ is fixed by the cold EoS the boundary between regime III and IV does not depend on ϵ_{th}.

The identification of these four regimes is the critical new input to the eff PT procedure. For given values of ρ and ϵ_{th}, we need to determine in which regime matter with these thermodynamic properties is located by comparing to the phase boundaries $\epsilon_{\text{th,on}}(\rho)$ and $\epsilon_{\text{th,fin}}(\rho)$. We will assume that these are known functions. In practice, this can either mean assuming an explicit analytic form or providing tables and interpolating to non-tabulated values. By inverting these functions, the densities ρ_{on} and ρ_{fin} can be inferred for a fixed ϵ_{th}. In the following subsections, we will present the procedure to infer the total pressure P at finite ϵ_{th} in the four different regimes.

4.2.1. Regime I

If $\epsilon_{\text{th}} < \epsilon_{\text{th,on}}(\rho)$ then matter remains in the hadronic phase. This case is effectively equivalent to any purely hadronic EoS, where the traditional ideal-gas approach has been shown to work well. This is also indicated by Fig. 4.3(a), in which the red and the green line almost coincide in regime I. Therefore, in this regime we determine P using Eq. (2.26) and Eq. (2.28) with $\Gamma_{\text{th}} = 1.75$.

4.2.2. Regime II

For $\epsilon_{\text{th,on}}(\rho) \leq \epsilon_{\text{th}} < \epsilon_{\text{th,fin}}(\rho)$, matter lies between ρ_{on} and ρ_{fin}, i.e. in the coexistence region. As discussed before, in this regime the pressure at finite ϵ_{th} may be lower than P_{cold} of the cold barotropic EoS. Therefore, this regime has to be treated with some care.

The procedure we develop to approximate P is sketched in Fig. 4.4. Here, the blue line is a hypothetical cold hybrid EoS model and the red line shows the EoS we construct with our eff PT procedure at constant $\epsilon_{\text{th}} > 0$ from the blue line and our knowledge of ρ_{on} and ρ_{fin}. We recall that we explicitly assume ρ_{on} and ρ_{fin} to be known for a given ϵ_{th}. Note that this figure only serves to explain the eff PT procedure and does not show any microphysical EoS model.

Based on the observation from Fig. 4.3(a) that the pressure in the coexistence phase can be approximated by a linear function, the main idea to infer P is to estimate the pressures P_{on} and P_{fin} at the densities ρ_{on} and ρ_{fin} highlighted by red crosses in Fig. 4.4 and then to interpolate at the density ρ.

As P_{on} is located at the onset of quark deconfinement, it should still be well approximated by the traditional ideal-gas approach. Therefore, P_{on} can be estimated by inferring P_{cold} at ρ_{on} from the cold EoS and calculating P_{th} using Eq. (2.28) and $\Gamma_{\text{th}} = 1.75$. This is indicated by the blue and black arrows on the left side of Fig. 4.4. P_{fin} cannot be obtained in the same way because of the problems of the ideal-gas approach we outlined before. Instead, the idea is to estimate the pressure at two densities above $\rho_{\text{fin},0}$ and to extrapolate downwards to ρ_{fin}.

As discussed earlier, at densities above ρ_{fin} P_{th} can be approximated with the ideal-gas approach using $\Gamma_{\text{th}} = 4/3$. Together with the values from the cold EoS, we then determine P at two densities above $\rho_{\text{fin},0}$ and use the slope $\frac{\mathrm{d}P}{\mathrm{d}\rho}$ to extrapolate the pressure P_{fin} at ρ_{fin}. This is indicated by the two rightmost arrows, the red dots and the black arrow in Fig. 4.3(a). Now that we have the pressures P_{on} and P_{fin}, we infer P at the density ρ through linear interpolation.

In rare cases the extrapolated pressure P_{fin} can be smaller than P_{on}. This would result in an unphysical drop of the pressure with increasing density. To avoid such a behavior, we instead use the slope of the cold EoS in the coexistence phase $m = (P_{\text{cold}}(\rho_{\text{fin},0}) - P_{\text{cold}}(\rho_{\text{on},0}))/(\rho_{\text{fin},0} - \rho_{\text{on},0})$ and extrapolate linearly from P_{on} and ρ_{on} to ρ, if this case occurs.

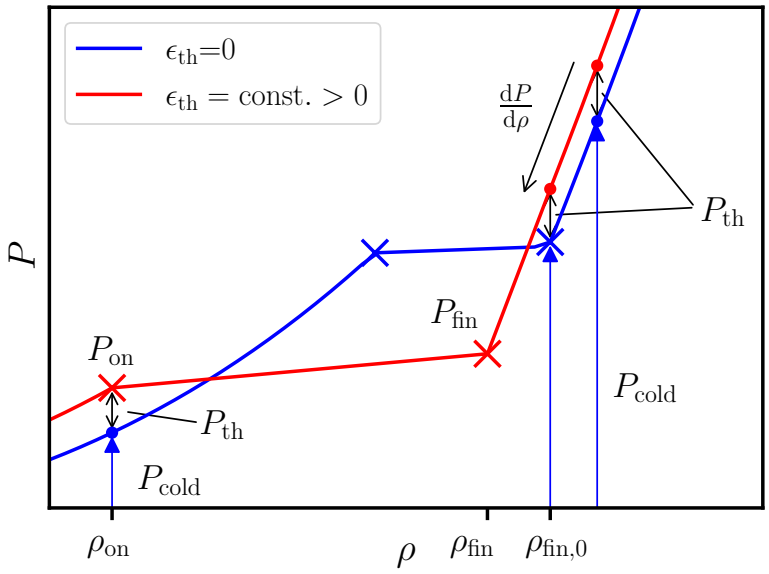

Figure 4.4.: Sketch of our effective procedure to estimate the pressure for $\epsilon_{\rm th} > 0$. The blue line depicts a barotropic, hybrid EoS, which we assume to be given. The red line represents the same EoS at constant $\epsilon_{\rm th} > 0$. For a given $\epsilon_{\rm th}$, we determine the densities $\rho_{\rm on}$ and $\rho_{\rm fin}$ from the phase boundaries, which have to be provided. For the pressure $P_{\rm on}$, we estimate $P_{\rm th}$ with Eq. (2.28) using $\Gamma_{\rm th} = 1.75$. For $P_{\rm fin}$, we consider two points above $\rho_{\rm fin,0}$ and infer $P_{\rm th}$ at these points with Eq. (2.28) and $\Gamma_{\rm th} = 4/3$. From these two points, we obtain the slope $\frac{{\rm d}P}{{\rm d}\rho}$ and use it to extrapolate $P_{\rm fin}$ at $\rho_{\rm fin}$. For densities between $\rho_{\rm on}$ and $\rho_{\rm fin}$, we estimate P through linear interpolation between $\rho_{\rm on}$ and $\rho_{\rm fin}$. Figure adapted from Ref. [361].

.

4.2.3. Regime III

For $\epsilon_{\rm th,fin} \leq \epsilon_{\rm th}$ and $\rho < \rho_{\rm fin,0}$, matter is in the pure deconfined quark phase but cold matter at the same density is in the coexistence phase. We see from Fig. 4.3(a) that P may still be lower than $P_{\rm cold}$ in this regime.

In Fig. 4.4, this case occurs in the density range from the red cross at $P_{\rm fin}$ to the red dot at $\rho_{\rm fin,0}$. Hence, the pressure can be inferred in the same way as $P_{\rm fin}$ in the previous section. We estimate the pressure at two points above $\rho_{\rm fin,0}$, determine the slope $\frac{{\rm d}P}{{\rm d}\rho}$ and then extrapolate down to ρ.

We then perform an additional consistency check. We determine the pressure $P_{\rm on}$ as for regime II. Then we extrapolate linearly to the density ρ using the slope of the cold EoSs in the coexistence phase $m = (P_{\rm cold}(\rho_{\rm fin,0}) - P_{\rm cold}(\rho_{\rm on,0}))/(\rho_{\rm fin,0} - \rho_{\rm on,0})$ to obtain a new pressure P^*. To avoid an unphysical drop in pressure with density, we pick the larger value of P and P^* as our approximated pressure in this regime.

4.2.4. Regime IV

If we have $\rho > \rho_{\rm fin,0}$ matter is in the pure deconfined quark phase at all densities. Here, the ideal gas approach can provide a reasonable approximation since no further transition takes place in this regime. However, as discussed before, $\Gamma_{\rm th} = 1.75$ slightly overestimates the pressure in the

deconfined quark matter phase and $\Gamma_{\rm th} = 4/3$ should provide a better description. Hence, we will use the ideal-gas approach with $\Gamma_{\rm th} = 4/3$ to infer P at densities above $\rho_{\rm on,0}$. The cold pressure at this density can be directly inferred from the tabulated EoS.

4.2.5. Choices of $\Gamma_{\rm th}$

We briefly motivate the values of $\Gamma_{\rm th}$ we picked in the different regimes of the eff PT scheme. For this, we determine the total pressure P at fixed $\epsilon_{\rm th}$ and cold, beta-equilibrium Y_e for all DD2F-SF EoSs as a function of density from the respective 3D table. We then infer $P_{\rm cold}$ at each density from the 1D EoS table and obtain $P_{\rm th}$ from Eq. (2.27). By inverting Eq. (2.28) we calculate $\Gamma_{\rm th}(\rho)$.

We show the calculated values of $\Gamma_{\rm th}(\rho)$ for the DD2F-SF-1 model in Fig. 4.5(a). Different colors refer to different $\epsilon_{\rm th}$.

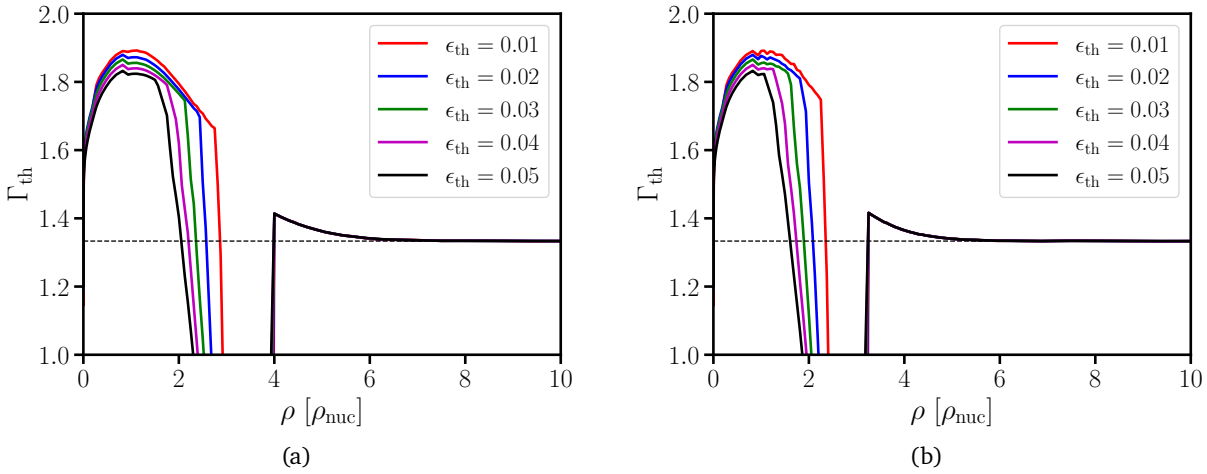

Figure 4.5.: (a): Thermal ideal-gas index as function of density for the DD2F-SF-1 EoS at different $\epsilon_{\rm th}$. The dashed line marks $\Gamma_{\rm th} = 4/3$, which is expected for an ultra-relativistic Fermi gas. (b): Same as (a) but for the DD2F-SF-2 EoS.

We see that at low densities (below $\approx 2 \times \rho_{\rm nuc}$) $\Gamma_{\rm th}$ is in the range of $\Gamma_{\rm th} \approx 1.6 - 1.85$ with larger $\epsilon_{\rm th}$ leading to smaller $\Gamma_{\rm th}$. Here, matter remains in the hadronic phase. Hence, $\Gamma_{\rm th} = 1.75$ is a reasonable choice for regime I.

At higher densities, we observe a sharp drop of $\Gamma_{\rm th}$ quickly leading to $\Gamma_{\rm th} < 1$ corresponding to negative $P_{\rm th}$ (as defined by Eq. (2.28)). Larger $\epsilon_{\rm th}$ feature this drop at lower densities. This behavior is caused by the "earlier" onset of the phase transition resulting in lower pressures at $\epsilon_{\rm th} > 0$ than at $\epsilon_{\rm th} = 0$ (see Fig. 4.3).

At densities around $4 \times \rho_{\rm nuc}$, $\Gamma_{\rm th}$ steeply rises and reaches values around $\Gamma_{\rm th} = 1.4$, irrespective of $e_{\rm th}$. Here, matter at $\epsilon_{\rm th} = 0$ enters the pure quark phase. With increasing density, $\Gamma_{\rm th}$ approaches 4/3 as indicated by the horizontal dashed line. This value is expected for an ultra-relativistic Fermi gas. Recall that we have picked $\Gamma_{\rm th} = 4/3$ in our eff PT scheme at all densities in the pure deconfined quark phase, i.e. at $\rho \geq \rho_{\rm fin,0}$. In particular, we use this value to extrapolate the pressures in regime III as well as infer the value of $P_{\rm fin}$ for constructing the pressures in regime II. When approximating this model, we hence expect to slightly underestimate the pressure in these two regimes as well as in the low density part of regime IV. Note however, that these errors are comparable to those induced by picking a constant $\Gamma_{\rm th}$ throughout the hadronic phase.

We find similar results for other DD2F-SF EoSs. In particular, we always find $\Gamma_{\rm th} \approx 1.4$ around $\rho_{\rm fin,0}$ followed by an asymptotic decay to $\Gamma_{\rm th} = 4/3$ with increasing density. As an example, we show $\Gamma_{\rm th}(\rho)$ for the DD2F-SF-2 EoS in Fig. 4.5(b). In comparison to the DD2F-SF-1 EoS, we see that the onset of the phase transition is shifted to lower densities, but the overall behavior of the curves remains very similar.

Note that the onset of quark deconfinement and especially the EoS of pure deconfined quark matter are very uncertain. Therefore, it is not clear whether the trend of $\Gamma_{\rm th}$ is a general behavior of hybrid EoS models or simply a feature of the SF approach since all DD2F-SF EoS share this phenomenological model. We continue to use $\Gamma_{\rm th} = 4/3$ for the pure deconfined quark phase throughout this work, as this value is physically motivated by assuming deconfined quark matter behaves like an ideal, ultra-relativistic Fermi gas.

4.3. Testing the effPT scheme

In this section, we test the performance of the effPT approach by comparing results from this scheme to results using the fully temperature- and composition-dependent DD2F-SF EoS set. First, we attempt to reconstruct the DD2F-SF models in a wide density and temperature range. Additionally, we perform merger simulations and compare the inferred dominant postmerger gravitational-wave (GW) frequencies when employing the effPT scheme to results from simulations with the full EoS tables. Our findings demonstrate that the effPT approach closely resembles a fully consistent treatment of the temperature-dependent phase boundaries. We also compare the results with the effPT scheme to the performance of the traditional ideal-gas approach and find that neglecting the shift of quark deconfinment at finite temperatures can induce significant deviations in the EoS and GW frequencies.

4.3.1. Reconstructing the DD2F-SF EoSs

To show the importance of correctly accounting for changing transition densities at finite temperatures, we estimate the pressure of the DD2F-SF models in a range of densities and temperatures with both the effPT scheme and the traditional ideal-gas approach. For evaluating the performance, we consider the relative residuals, which we define as $|P_{\rm true} - P_{\rm approx}|/P_{\rm true}$. $P_{\rm approx}$ is the pressure approximated by either of the two effective schemes and $P_{\rm true}$ is the pressure inferred from the respective 3D EoS table. For both effective treatments, we reconstruct the pressure using the tabulated values of $\epsilon_{\rm th}$. Additionally, we employ the true phase boundaries of the DD2F-SF models (see Fig. 3.4) in the effPT approach. All quantities from the EoS tables are inferred at Y_e corresponding to cold beta-equilibrium composition. In the traditional idea-gas approach, we pick different values of $\Gamma_{\rm th}$ depending on the phase present in the zero-temperature EoSs. With this we aim to at least somewhat account for the different thermal behavior of the hadronic and the deconfined quark phase. We set $\Gamma_{\rm th} = 1.75$ for $\rho \leq \rho_{\rm on,0}$, $\Gamma_{\rm th} = 1.4$ for $\rho_{\rm on,0} < \rho < \rho_{\rm on,0}$ and $\Gamma_{\rm th} = 4/3$ for $\rho \geq \rho_{\rm fin,0}$. We remark that this choice of $\Gamma_{\rm th}$ leads to a drop in pressure at the densities $\rho_{\rm on,0}$ and $\rho_{\rm fin,0}$ for a fixed value of $\epsilon_{\rm th}$.

We then average the reconstructed values over the tabulated temperatures between $T = 5$ MeV and $T = 80$ MeV, as this is the relevant temperature range for many astrophysical scenarios such as neutron star mergers and core collapse supernovae. Since the tables have more tabulated points a low temperatures, we keep a separation of at least 5 MeV between two considered points to not over-represent the low temperatures range.

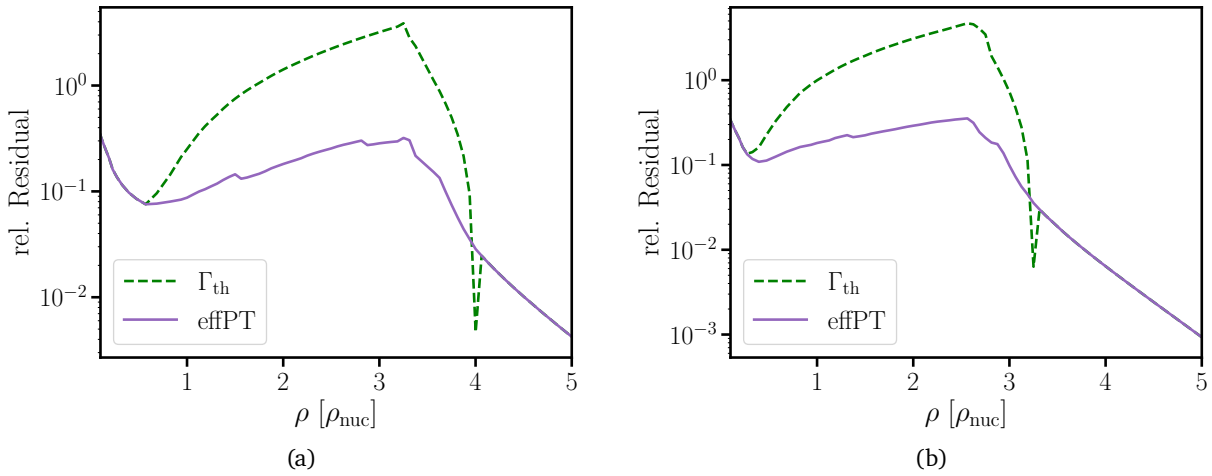

Figure 4.6.: (a): Density dependence of the mean relative residuals for the total pressure from the thermal ideal-gas approach and our effective treatment of thermal effects in hybrid models compared to the actual DD2F-SF-1 EoS. At each density, we average over the residuals in the temperature range between $T = 5$ MeV and $T = 80$ MeV. Figure adapted from Ref. [361]. (b): Same as (a) but for the DD2F-SF-2 EoS.

We plot the averaged relative residuals from the effPT and the traditional ideal-gas approach for the DD2F-SF-1 EoS for different densities in Fig. 4.6(a) with a purple and a dashed green line, respectively. Note the logarithmic scale of the y-axis.

We see that at very low and very high densities the residuals from both schemes are identical. This is because at these densities no phase transition occurs in the considered temperature range. Matter either remains purely hadronic or pure deconfined quark matter is already present at $T = 0$. Since we chose $\Gamma_{\rm th} = 1.75$ for the hadronic phase and $\Gamma_{\rm th} = 4/3$ for the deconfined quark phase in both approaches, the results are identical if no transition sets in with increasing temperature.

On the other hand, in the intermediate density range, namely between roughly $0.6 \times \rho_{\rm nuc}$ and $4 \times \rho_{\rm nuc}$, the effPT scheme reproduces the DD2F-SF-1 with much greater accuracy than the traditional approach. Especially for densities between about $2 \times \rho_{\rm nuc}$ and $3.5 \times \rho_{\rm nuc}$, the temperature-averaged relative residuals from the ideal-gas approach become larger than 1 implying a more than 100% error for the estimated pressure. This occurs despite the adjustments on $\Gamma_{\rm th}$ in the ideal-gas scheme. In this density range, the relative residuals from the effPT scheme are about an order of magnitude smaller.

Around $4 \times \rho_{\rm nuc}$ there appears to be a small region, where the traditional ideal-gas scheme significantly outperforms the effPT scheme (even though the relative residual of the effPT scheme is still smaller than 10%). This feature is caused by a single tabulated density point located right at the border between the coexistence phase and the pure deconfined quark phase at $T = 0$. Hence, at this density pure deconfined quark matter is present at practically all finite temperatures, the traditional scheme however still assumes $\Gamma_{\rm th} = 1.4$ here. As demonstrated in Sec. 4.2.5, the DD2F-SF model features $\Gamma_{\rm th}$ of around 1.4 in this density range, only dropping to $\Gamma_{\rm th} = 4/3$ at higher densities. Since the effPT scheme uses $\Gamma_{\rm th} = 4/3$ to extrapolate from the quark phase, it slightly underestimates the thermal pressure at this point leading to a larger relative residual compared to the ideal-gas approach.

Table 4.1.: Mean relative residuals of the total pressure calculated by the traditional ideal-gas approach and our effPT scheme compared to the actual EoS for all DD2F-SF models (compare Fig. 4.6). We average the residuals over all points tabulated in the respective EoS file in the temperature range of 5 MeV to 80 MeV and the density range of $0.5 \times \rho_{\rm nuc}$ to $5 \times \rho_{\rm nuc}$. Table adapted from Ref. [361].

EoS	traditional approach	effective scheme
DD2F-SF-1	1.179	0.146
DD2F-SF-2	1.429	0.149
DD2F-SF-3	1.209	0.117
DD2F-SF-4	1.111	0.089
DD2F-SF-5	1.294	0.094
DD2F-SF-6	1.139	0.090
DD2F-SF-7	1.294	0.278

In Fig. 4.6(b), we show the relative residuals for the DD2F-SF-2 EoS. We find qualitatively very similar results as for the DD2F-SF-1 model. A noticeable difference is that compared to Fig. 4.6(a), the region of larger deviations for both approaches is shifted towards lower densities due to the lower onset densities of the DD2F-SF-2 EoS. We obtain similar results for the other DD2F-SF models. To quantify the performance of both schemes in reconstructing the EoSs, we further average the temperature-averaged relative residuals over all tabulated densities in the range between $0.5 \times \rho_{\rm nuc}$ and $5 \times \rho_{\rm nuc}$. We provide these averaged residuals for all DD2F-SF EoSs in Table 4.1. Generally, the effPT scheme performs well and produces average relative residuals of around 10%-15%. The only exception is the DD2F-SF-7 EoS where the error is somewhat larger with about 28%.

On the other hand, the traditional scheme produces errors about an order of magnitude larger than the effPT approach in the chosen density and temperature range. For this treatment, we observe relative residuals of around 110%-140%. As this EoS range is most relevant for neutron star mergers, these results demonstrate the importance of properly accounting for the temperature-dependent phase boundaries. We conclude that employing the traditional approach, i.e. assuming constant phase boundaries, leads to average pressure differences of more than 100% even with different choices of $\Gamma_{\rm th}$ depending on the phase of the cold EoS.

4.3.2. Merger simulations at a fixed system mass

We further validate the effPT scheme by performing several NS merger simulations with all 7 DD2F-SF EoSs. For each EoS, we perform 3 simulations. One using the full 3D EoS table, one with the 1D table and the effPT approach and one with the 1D table and the traditional ideal-gas treatment. We refer to these simulations as 3D framework, effPT framework and $\Gamma_{\rm th}$ framework, respectively. For the effPT framework, we use the phase boundaries, i.e. $\rho_{\rm on}$ and $\rho_{\rm fin}$, of every DD2F-SF model as a function of the specific thermal energy $\epsilon_{\rm th}$. We extract these boundaries before the simulation from the respective 3D table by interpolating to the Y_e of cold, beta-equilibrium at each density and provide them to the simulation code in tabulated form. For the $\Gamma_{\rm th}$ framework, we use the same values of $\Gamma_{\rm th}$ in different density ranges as described in Sect. 4.3.1 to somewhat mimic the different thermal properties of deconfined quark matter. All simulations evolve symmetric binaries with a total system mass of $2.7\ M_\odot$ at infinite separation and do not employ the procedure outlined in Appendix A to enforce an initial radial velocity at the beginning of the simulation. We recall that in the 3D framework each SPH particle has a Y_e value assigned during the setup. This is then

advected with the particle during the simulation. In the other two frameworks Y_e is always adjusted to the value of cold, beta-equilibrium as the density of a particle evolves. This different treatment of composition effects will additionally introduce differences between the 3D framework compared the other frameworks.

Fig. 4.7(a) shows the time evolution of the maximum rest-mass density $\rho_{\max}$ from all simulations with the DD2F-SF-1. The results from the three different frameworks are displayed with different colors. The horizontal lines mark the phase boundaries of this model at zero temperature, the vertical line highlights the merging time. In order to increase the visibility, we slightly smoothed the simulation output of $\rho_{\max}$ in plots throughout this chapter as the SPH method features some small amount of noise when physical quantities are directly evaluated on the particles.

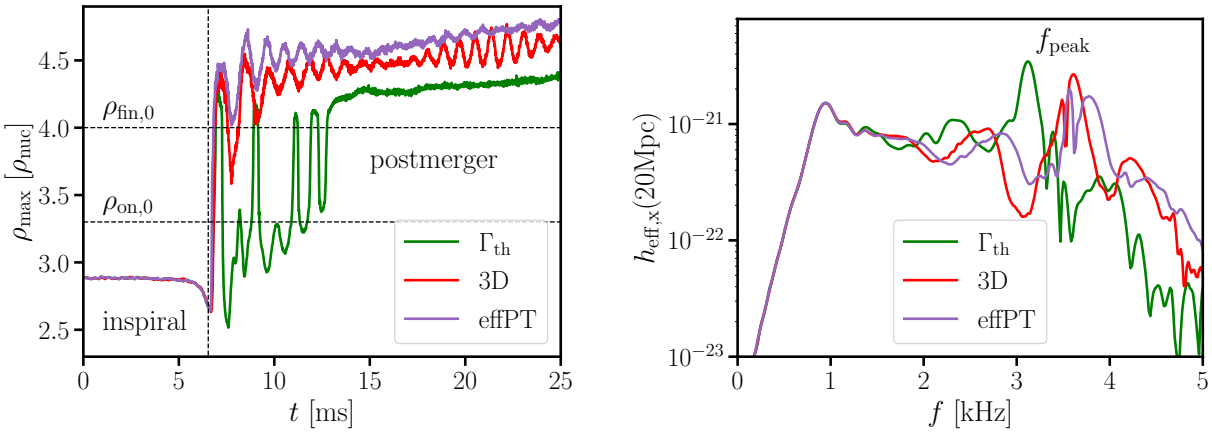

Figure 4.7.: Evolution of the maximum rest-mass density for the merger of two $1.35\ M_\odot$ NSs using the DD2F-SF-1 EoS and the different frameworks outlined in the text to model the finite-temperature regime of the EoS. The horizontal dashed lines show the phase boundaries of this EoS at zero temperature. The vertical line marks the merging time. (b): Gravitational-wave spectrum of the cross polarization at a distance of 20 Mpc along the polar axis from the same simulations as in (a). Both figures adapted from Ref. [361].

We see that prior to the merger, the maximum densities in all three frameworks are almost identical. This is plausible since at this stage of the evolution, the densities are below $\rho_{\rm on,0} = 3.30 \times \rho_{\rm nuc}$ and the stars are cold. After the merger, we observe that in the $\Gamma_{\rm th}$ framework $\rho_{\max}$ exhibits strong oscillations bouncing in and out of the quark phase. At later times, around 6 ms after the merger, some material settles permanently into the pure deconfined quark matter phase. In the 3D framework, $\rho_{\max}$ shows a different behavior. In this simulation matter at the highest densities enters the pure, deconfined quark phase on the first contraction of the merger remnant and remains in this state throughout almost the entire postmerger evolution. We clearly see the larger overall densities and smaller oscillations compared to the results from the $\Gamma_{\rm th}$ framework.

From this observation, we conclude that the different density evolution in the $\Gamma_{\rm th}$ framework is an artifact of the ideal-gas scheme not considering the shifting phase boundaries at finite temperatures. As apparent from Fig. 4.2 and Fig. 4.3, this leads to an overestimation of the pressure in the merger remnant resulting in lower overall densities. Additionally, we see in Fig. 4.3 that the $\Gamma_{\rm th}$ framework

also induces an incorrect EoS shape. Since the phase boundaries change with temperature at fixed $\epsilon_{\rm th}$, the transition region smears out and becomes a more smooth function of density. On the other hand, the ideal-gas approach more closely resembles the shape of the cold EoS, namely a steeper increase of pressure followed by a almost flat plateau. Both effects lead to the stronger oscillations and the overall lower values of $\rho_{\rm max}$ in the $\Gamma_{\rm th}$ framework compared to the 3D framework.

The eff PT framework does correctly consider the thermal shift of the phase boundaries. As we see in Fig. 4.7(a), it performs significantly better than the $\Gamma_{\rm th}$ framework at reproducing the maximum density evolution of the 3D framework. In particular, matter at the highest density in this simulation also enters the pure quark phase on the first contraction and remains in this phase throughout the postmerger evolution. However, we also see that the eff PT approach slightly overestimates the densities in the merger remnant during the entire postmerger evolution. This may be caused by the minor underestimation of the pressure in the regimes II and III we discussed in Sect. 4.2.5. Additionally, the eff PT scheme does not include isospin-dependence and matter is assumed to be in cold, beta-equilibrium composition at all times. This approximation will also contribute to the small differences between the 3D and the eff PT framework we observe.

In three of our simulations (using the DD2F-SF-4,6,7 EoSs), we observe a delayed transition taking place in the merger remnant when employing the ideal-gas approach. In these systems, no quark matter is present after the initial density increase. As the remnant further evolves, it continues to contract and the phase transition sets in after a few milliseconds. This results in a sudden increase of the maximum density.

When using the 3D EoS tables or the eff PT scheme, this feature does not occur for the binary mass configurations we consider in this work. In these frameworks, deconfined quark matter is always present in the postmerger remnant due to the "earlier" onset of quark deconfinement at finite temperatures. Especially, we observe that in these systems the maximum densities are already larger than $\rho_{\rm on,0}$ right after the merger and no sudden increase at later time takes place. The delayed onset of quark deconfinement in the systems simulated with the $\Gamma_{\rm th}$ framework is hence likely an artifact of this approach not accounting for the temperature-dependent phase boundaries. This indicates a delayed phase transition in the merger remnant may be a less common feature. We will further explore this issue in Sect 4.4.3.

Next, we will discuss the GW signals from the simulations using the three different frameworks. Figure 4.7(b) shows the spectra of the cross polarization at a distance of 20 Mpc along the polar axis for the DD2F-SF-1 EoS from all three frameworks. The color scheme is the same as in Fig. 4.7(a).

We see that the low frequency part (roughly below 1.7 kHz) of all three spectra is virtually identical. This is plausible, as this part of the GW spectrum is produced during the inspiral where the stars remain cold and no differences between the three frameworks are present. The higher frequency range is formed from postmerger remnant oscillations and hence more affected by thermal effects. Here, greater differences between the three spectra are present. We clearly see the dominant peak $f_{\rm peak}$ caused by the fundamental quadrupole fluid mode of the remnant, as explained in Sect. 1.3, for all three simulations.

From the 3D framework, we derive an $f_{\rm peak}$ of abut 3.61 Hz. However, for the $\Gamma_{\rm th}$ framework we find a value around 500 Hz smaller at only 3.12 kHz. Such a difference is substantial and will be measurable with future GW detectors. The reason for this huge discrepancy, as we have discussed before, is that the $\Gamma_{\rm th}$ framework assumes a stiffer EoS at finite temperatures (see Fig. 4.3(a)), which results in less compact remnants with lower densities and fewer amounts of quark matter.

The spectrum of the eff PT framework in Fig. 4.7(b) is in much better agreement with the spectrum of the 3D EoS table. We infer an $f_{\rm peak}$ of around 3.57 kHz from this spectrum, i.e. around 40 Hz smaller than from the 3D framework. This is somewhat surprising as our earlier discus-

Table 4.2.: Dominant postmerger GW frequency f_{peak} in kHz for our sample of DD2F-SF EoS models inferred from simulations. The different columns correspond to the different frameworks modeling the finite-temperature regimes as outlined in the text.

EoS	Γ_{th}	3D	effPT
DD2F-SF-1	3.12	3.61	3.57
DD2F-SF-2	3.25	3.58	3.62
DD2F-SF-3	3.12	3.50	3.52
DD2F-SF-4	3.16	3.33	3.44
DD2F-SF-5	3.22, 3.42	3.54, 3.81	3.60, 3.85
DD2F-SF-6	3.14	3.64	3.67
DD2F-SF-7	3.13	3.37	3.41

sion suggested the effPT scheme tends to slightly overestimate the remnant densities. Hence, we would also expect a somewhat larger f_{peak}. A closer look at the spectrum shows that overall the high frequency part does indeed seem to be shifted towards larger frequencies compared to the 3D framework. Only the highest peak is narrowly smaller. However, there is a second peak in the effPT spectrum at larger frequencies of about 3.78 kHz. Such a split in f_{peak} is typically attributed to a frequency drift during the postmerger phase [49]. As the merger remnant evolves, the dominant oscillation mode changes with time. The exact shape of the peak around f_{peak} is hence affected by the remnant dynamics.

Generally, we still observe that the effPT scheme is able to reproduce the overall shape of the GW spectrum significantly better than the traditional ideal-gas approach. This also applies to the secondary peak at around 2.5 kHz.

We find similar results for the other DD2F-SF models. In Tab. 4.2 we provide the obtained f_{peak} frequencies from the entire DD2F-SF EoS sample from all three frameworks. We consistently find that the Γ_{th} framework greatly underestimates the frequencies compared the 3D framework with differences reaching up to 500 Hz. Additionally, we see that the frequencies inferred with the ideal-gas approach are relatively similar for all 7 models and close to the f_{peak} produced by the purely hadronic DD2F EoS of 3.10 kHz (see Fig. 4.9). This indicates that in the Γ_{th} framework, the phase transition only weakly influences the overall remnant structure and hence the corresponding postmerger GW signal. In particular, we find that the appearance of a delayed transition in the remnant shortly after the merger does not have a visible impact on the GW spectrum as the remnant has already mostly settled down and further GW emission is very weak.

On the other hand, we find good agreement between the effPT and the 3D framework with maximum deviations of f_{peak} of 110 Hz. This demonstrates that the temperature-dependence of the phase boundaries needs to be considered properly as it has a large impact on the whole remnant structure. This is understandable, since the "earlier" onset of the phase transition at finite temperatures leads to more deconfined quark matter in these systems compared to simulations with the Γ_{th} framework.

As a second example, we plot the evolution of the maximum density and the GW spectra from the simulations with the DD2F-SF-5 EoS in Fig. 4.8. We find similar results for ρ_{max} as for the DD2F-SF-1 model in Fig. 4.7(a). The Γ_{th} scheme produces strong oscillations in and out of the deconfined quark phase at early times while in the 3D as well as in the effPT scheme pure deconfined matter is present at all times after the initial density increase at merging. For the GW spectra, we observe that all three frameworks produce two distinct dominant peaks at high frequencies. While the two peaks from the effPT and the 3D framework agree within 60 Hz, the peaks from the Γ_{th} framework

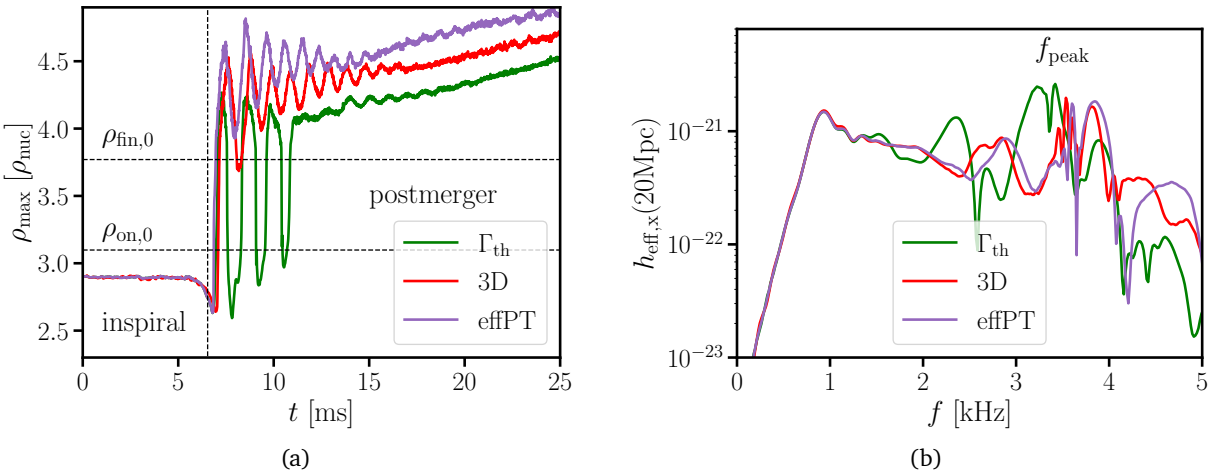

Figure 4.8.: Evolution of the maximum rest-mass density for the merger of two $1.35\ M_\odot$ NSs using the DD2F-SF-5 EoS and the different frameworks outlined in the text to model the finite-temperature regime of the EoS. The horizontal dashed lines show the phase boundaries of this EoS at zero temperature. The vertical line marks the merging time. (b): Gravitational-wave spectrum of the cross polarization at a distance of 20 Mpc along the polar axis from the same simulations as in (a).

appear at frequencies about 300 Hz to 400 Hz lower compared to the other two approaches. For this EoS we hence provide both values of $f_{\rm peak}$ for each framework can in Tab. 4.2.

From our results, we conclude that for the DD2F-SF EoS sample the shifting of the phase boundaries at finite thermal energies is the main process affecting the remnant structure enough to reveal the phase transition through the GW signal. As the traditional ideal-gas approach neglects these shifts, it fails to reproduce the correct values of $f_{\rm peak}$ and differences up to 500 Hz compared to employing the full 3D EoS table emerge. The effPT scheme on the other hand, does consider the changing phase boundaries at finite temperatures. Hence, it is able to properly capture the transition to deconfined quark matter at all $\epsilon_{\rm th}$ and reproduce the results from the 3D framework with much higher accuracy. This implies that the effPT scheme is also able to replicate features indicating the appearance of deconfined quark matter in neutron star merger remnants such as a characteristic shift of $f_{\rm peak}$ compared to the tidal deformability ([52, 53]). Simulations employing the traditional ideal-gas index on the other hand, may not reliably describe such features as demonstrated by the significant underestimation of postmerger GW frequencies. We therefore advertise caution when employing this scheme for hybrid EoSs.

We also find that for the DD2F-SF models, the dependence of $f_{\rm peak}$ on Y_e is relatively weak. Recall that both the effPT and the $\Gamma_{\rm th}$ scheme do not include composition effects and always assume cold, neutrinoless beta-equilibrium composition. Since the phase boundaries only weakly change with Y_e, the effPT scheme is still able to reproduce $f_{\rm peak}$ with good accuracy. In principle, a stronger dependence of the transition densities on Y_e may occur, which would require additional modifications to the effPT scheme.

4.3.3. Merger simulations at different binary masses

So far, we have only tested the effPT scheme at a fixed binary mass $M_{\rm tot}$ of 2.7 $M_\odot$. When varying $M_{\rm tot}$, changes in $f_{\rm peak}$ as well as in the strength of the shift between a hybrid EoS and the corresponding purely hadronic EoS are expected (see Ref. [53]). At very low $M_{\rm tot}$, the densities and temperatures in the system are too low to produce significant amounts of deconfined quark matter to noticeably impact the structure of the merger remnant. Hence, no or at most small differences in $f_{\rm peak}$ between hybrid and hadronic EoS are seen. With increasing $M_{\rm tot}$, larger amounts of matter transition into the deconfined quark phase shifting $f_{\rm peak}$ more strongly.

To provide a more stringent test, we explore whether the effPT scheme can qualitatively and quantitatively capture the dependence of $f_{\rm peak}$ on $M_{\rm tot}$ for a hybrid EoS. For this, we perform additional merger simulations with the nucleonic DD2F EoS and the hybrid DD2F-SF-6 model. For both EoSs, we simulate symmetric binaries with masses of 2.4 $M_\odot$, 2.5 $M_\odot$, 2.611 $M_\odot$, 2.65 $M_\odot$, 2.7 $M_\odot$ and , 2.78 $M_\odot$, which are the masses used in Ref. [53]. For the simulations with the DD2F model, we use the full 3D EoS table, for the DD2-SF-6 EoS we employ the effPT and the 3D framework.

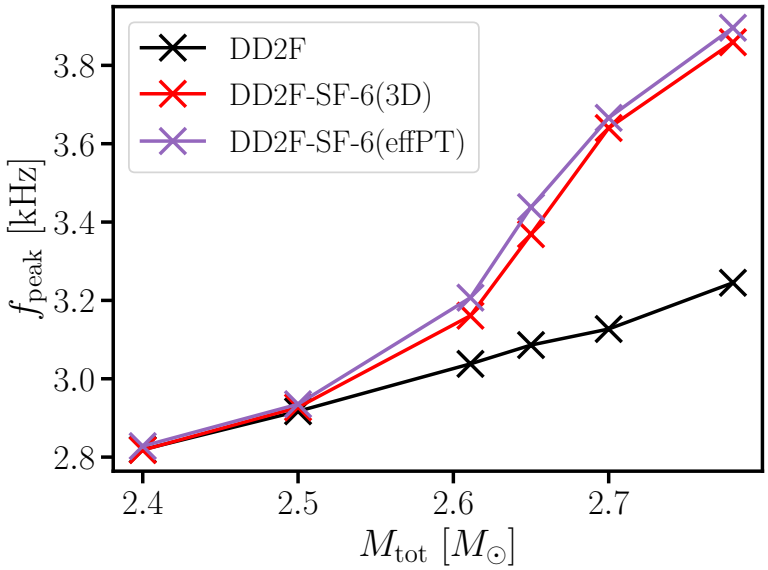

Figure 4.9.: Dominant postmerger GW frequency $f_{\rm peak}$ as a function of the total binary mass for the purely nucleonic DD2F model (black) and the hybrid DD2F-SF-6 EoS (colored). Crosses show simulation data, between these points linear interpolation is used. The two different colors refer to different approaches to model the finite-temperature regime of the DD2F-SF-6 EoS as outlined in the text. Figure adapted from Ref. [361].

The resulting $f_{\rm peak}$ frequencies are plotted in Fig. 4.9 as a function of $M_{\rm tot}$. We see that the effPT scheme is able to reproduce $f_{\rm peak}$ from the 3D framework very well in the whole mass range. In particular, we find that the range, where the results from the hybrid model begin to deviate from those produced by the hadronic EoS, agrees well. Also, the stronger shift of $f_{\rm peak}$ at high and the almost coinciding values at lower masses are reproduced accurately.

We also see that the effPT scheme constantly yields slightly larger frequencies than the 3D framework, which we as also observe in the previous section. However, we find that the differences are minor and the overall behavior is captured very well.

4.4. Impact of different finite-temperature phase boundaries

So far, we have tested the effPT scheme and showed that it is able to reproduce results from fully temperature- and composition-dependent hybrid EoSs well when used with the correct phase boundaries at finite thermal energies. In this section, we will explore the impact different assumed phase boundaries at finite $\epsilon_{\rm th}$ can have in mergers for a given cold EoS. For this, we will consider different barotropic EoSs and perform simulations for a fixed, cold EoS and employ varying phase boundaries at finite temperature with our effPT scheme. We then compare the differences we find to directly probe finite-temperature effects.

4.4.1. Simple thermal EoS model

We begin by introducing a simple, yet thermodynamically consistent toy model to demonstrate that the cold, barotropic EoS does not completely determine the EoS at finite temperatures. In the case of two-phase hybrid models, different thermal treatments of both phases can thus result in a different temperature dependence of the phase boundaries. The scheme was developed by Stefan Typel and first presented in Ref. [361].

In a system in thermodynamic equilibrium with properties determined by the temperature T, the particle number N and the volume V, the relevant thermodynamic potential is the free energy

$$F(T,V,N) = -PV + \mu N \ , \tag{4.3}$$

with the pressure P and the chemical potential μ defined as

$$P = -\left.\frac{\partial F}{\partial V}\right|_{T,N} , \quad \mu = \left.\frac{\partial F}{\partial N}\right|_{T,V} . \tag{4.4}$$

The internal energy of the system E is given by

$$E(S,V,N) = F + TS \ , \tag{4.5}$$

where S is the entropy of the system defined as

$$S = -\left.\frac{\partial F}{\partial T}\right|_{V,N} . \tag{4.6}$$

When considering neutron star EoS models, it is useful to introduce densities

$$n = \frac{N}{V}, \quad f = \frac{F}{V}, \quad e = \frac{E}{V}, \quad s = \frac{S}{V} \tag{4.7}$$

removing N and V as explicit variables. With this we have

$$\begin{aligned} &f = -P + \mu n, \quad P = n^2 \left.\frac{\partial (f/n)}{\partial n}\right|_T , \quad \mu = \left.\frac{\partial f}{\partial n}\right|_T , \\ &s = -\left.\frac{\partial f}{\partial T}\right|_n , \quad e = f + Ts = Ts - P + \mu n \end{aligned} \tag{4.8}$$

If we split the energy density into a cold part e_c and a thermal part e_th, we see that the free energy also naturally splits into a thermal f_th and a cold part f_c

$$f = e_\mathrm{c} + e_\mathrm{th} - Ts \equiv f_\mathrm{c} + f_\mathrm{th} \tag{4.9}$$
$$\tag{4.10}$$

with

$$f_\mathrm{c} = e_\mathrm{c}, \quad f_\mathrm{th} = e_\mathrm{th} - Ts\ . \tag{4.11}$$

With this, we can write e_th as

$$e_\mathrm{th} = f_\mathrm{th} + Ts = f_\mathrm{th} - T\left.\frac{\partial(f_\mathrm{c}+f_\mathrm{th})}{\partial T}\right|_n = f_\mathrm{th} - T\left.\frac{\partial f_\mathrm{th}}{\partial T}\right|_n\ , \tag{4.12}$$

as f_c does not depend on T. For the pressure, we have

$$P = n^2\left.\frac{\partial((f_\mathrm{c}+f_\mathrm{th})/n)}{\partial n}\right|_T = n\left.\frac{\partial f_\mathrm{c}}{\partial n}\right|_T - f_\mathrm{c} + n\left.\frac{\partial f_\mathrm{th}}{\partial n}\right|_T - f_\mathrm{th} \equiv P_\mathrm{c} + P_\mathrm{th}\ , \tag{4.13}$$

with the thermal pressure P_th

$$P_\mathrm{th} = n\left.\frac{\partial f_\mathrm{th}}{\partial n}\right|_T - f_\mathrm{th}\ . \tag{4.14}$$

The definition of the thermal entropy density s_th and the thermal chemical potential is analogous and straightforward. We get

$$s_\mathrm{th} = -\left.\frac{\partial f_\mathrm{th}}{\partial T}\right|_n, \quad \mu_\mathrm{th} = \left.\frac{\partial f_\mathrm{th}}{\partial n}\right|_T\ . \tag{4.15}$$

If we assume that the ideal-gas relation $P_\mathrm{th} = (\Gamma_\mathrm{th}-1)e_\mathrm{th}$ with a constant Γ_th holds at all densities, we get

$$\Gamma_\mathrm{th} = \frac{P_\mathrm{th}}{e_\mathrm{th}} + 1 = \frac{n\left.\frac{\partial f_\mathrm{th}}{\partial n}\right|_T - f_\mathrm{th}}{f_\mathrm{th} - T\left.\frac{\partial f_\mathrm{th}}{\partial n}\right|_n} + 1 = \frac{n\left.\frac{\partial f_\mathrm{th}}{\partial n}\right|_T - T\left.\frac{\partial f_\mathrm{th}}{\partial T}\right|_n}{f_\mathrm{th} - T\left.\frac{\partial f_\mathrm{th}}{\partial n}\right|_n}\ . \tag{4.16}$$

This expression can be rewritten into a partial differential equation for f_th

$$\Gamma_\mathrm{th} f_\mathrm{th} = n\left.\frac{\partial f_\mathrm{th}}{\partial n}\right|_T - (1-\Gamma_\mathrm{th})T\left.\frac{\partial f_\mathrm{th}}{\partial T}\right|_n\ . \tag{4.17}$$

We will discuss two solutions of this equation.

First solution

A particular solution to Eq. (4.17) is given by

$$f_\mathrm{th} = Tn\left(a\ln\frac{n}{n_0} - b\ln\frac{T}{T_0} + c\right)\ , \tag{4.18}$$

where $a,\ b,\ c$ are dimensionless free parameters and n_0 and T_0 are scaling variables to guarantee correct units in the arguments of the logarithmic functions. This solution is similar to the free energy density of a classical ideal gas (without the rest-mass contribution)

$$f_{\text{id}} = Tn[\ln(n\lambda^3) - 1] \,, \tag{4.19}$$

where λ is the thermal wave length

$$\lambda = \sqrt{\frac{2\pi\hbar^2}{mT}} \tag{4.20}$$

depending on the temperature and the mass of the particles. Using Eq. (4.18) and the definitions in Eq. (4.12), Eq. (4.14) and Eq. (4.15), we get

$$\begin{aligned} \mu_{\text{th}} &= T\left(a\ln\frac{n}{n_0} - b\ln\frac{T}{T_0} + a + c\right), \quad P_{\text{th}} = aTn, \\ e_{\text{th}} &= bTn, \quad s_{\text{th}} = -n\left(a\ln\frac{n}{n_0} - b\ln\frac{T}{T_0} - b + c\right) \,. \end{aligned} \tag{4.21}$$

In order to have positive thermal pressure and energy we require $a > 0$ and $b > 0$. Additionally, we have the condition

$$\Gamma_{\text{th}} = 1 + \frac{a}{b} \,. \tag{4.22}$$

A specific choice of Γ_{th}, a and c hence completely determines the finite temperature EoS. For a classical ideal gas we have $a = 1$, $\Gamma = 5/3$ and

$$c = \ln\left(n_0\sqrt{\frac{2\pi}{mT_0}}^3\right) - 1 \,. \tag{4.23}$$

We can set

$$a = \sqrt{\frac{3}{2}(\Gamma_{\text{th}} - 1)}, \quad b = \sqrt{\frac{3}{2(\Gamma_{\text{th}} - 1)}} \tag{4.24}$$

to recover this ideal gas limit.

Second solution

A second possible solution to Eq. (4.17) is

$$f_{\text{th}} = aT^b n^c \tag{4.25}$$

with dimensionless constant parameters a, b and c. With Eq. (4.18), Eq. (4.12), Eq. (4.14) and Eq. (4.15), we get

$$\mu_{\text{th}} = acT^b n^{c-1}, \quad P_{\text{th}} = a(c-1)T^b n^c, \quad e_{\text{th}} = a(1-b)T^b n^c, \quad s_{\text{th}} = -abT^{b-1}n^c. \tag{4.26}$$

Requiring $s_{\text{th}} > 0$, $P_{\text{th}} > 0$ and $e_{\text{th}} > 0$ at finite temperature and $s_{\text{th}} = 0$, $P_{\text{th}} = 0$ and $e_{\text{th}} = 0$ at $T = 0$ leads to the conditions $a < 0$, $b > 1$ and $0 < c < 1$. For Γ_{th}, we get

$$\Gamma_{\text{th}} = \frac{c-b}{1-b}. \tag{4.27}$$

Similarly to the first solution, the finite temperature EoS is completely determined by a specific choice of a, b and Γ_{th}.

Phase transition

We now consider a system featuring two separated phases connected by a transition with a region of coexisting phases. We label quantities of the two phases with h and q, respectively and employ a Maxwell construction for the phase transition. In this approach, the pressure is assumed to be constant in the coexistence region between the densities $n_h(T)$ and $n_q(T)$ at a given temperature T. Starting from the Maxwell relation

$$\left.\frac{\partial P}{\partial n}\right|_T = n \left.\frac{\partial \mu}{\partial n}\right|_T , \tag{4.28}$$

we get

$$\mu_h(T) - \mu_q(T) = \int_{n_h(T)}^{n_q(T)} \frac{1}{n} \left.\frac{\partial P}{\partial n}\right|_T dn . \tag{4.29}$$

Assuming a constant pressure $P_{\text{pt}}(T)$ for $n_h(T) \leq n \leq n_q(T)$ implies $\left.\frac{\partial P}{\partial n}\right|_T = 0$ and hence $\mu_h(T) = \mu_q(T)$, i.e. a constant chemical potential $\mu_{\text{pt}}(T)$ in the coexistence region for a given T. Note that in general μ_h and μ_q depend on density and temperature and different values of T will therefore result in different phase boundaries $n_h(T)$ and $n_q(T)$. If we split the free energies in both phases into a cold and a thermal part

$$f^h = e^h_{\text{c}} + f^h_{\text{th}}, \quad f^q = e^q_{\text{c}} + f^q_{\text{th}} \tag{4.30}$$

and use the parametric solution from Eq. (4.18) for the thermal contributions, we obtain the equations

$$\begin{aligned} P_{\text{pt}}(T) =& P_{\text{c}}(n_h(T)) + a_h T n_h(T) \\ =& P_{\text{c}}(n_q(T)) + a_q T n_q(T) , \end{aligned} \tag{4.31}$$

$$\begin{aligned} \mu_{\text{pt}}(T) =& \mu_{\text{c}}(n_h(T)) + T(a_h \ln(n_h/n_0) - \\ & b_h \ln(T/T_0) + a_h + c_h) \\ =& \mu_{\text{c}}(n_q(T)) + T(a_q \ln(n_q/n_0) - \\ & b_q \ln(T/T_0) + a_q + c_q) , \end{aligned} \tag{4.32}$$

where P_c and μ_c refer to the contribution of pressure and chemical potential from the respective cold EoS.

These two equations fix the phase boundaries $n_h(T)$ and $n_q(T)$ at each temperature T. The energy densities at the edges of the coexistence phase are given by

$$e(T, n_h(T)) = e_{c,h}(n_h(T)) + b_h T n_h(T) , \tag{4.33}$$

$$e(T, n_q(T)) = e_{c,q}(n_q(T)) + b_q T n_q(T) . \tag{4.34}$$

Here, $e_{c,h}$ and $e_{c,q}$ are the energy densities of both phases at $T = 0$. Hence, the transition boundaries at finite temperatures are completely determined by the EoSs of both phases at zero temperature and a specific choice of the parameters a_h, b_h, c_h, a_q, b_q and c_q. Varying the thermal parameters will result in different $n_h(T)$ and $n_q(T)$ at $T > 0$, but not change the coexistence region at $T = 0$.

If we employ Eq. (4.25) as a solution for f_{th}, we obtain the following equations for $P_{\text{pt}}(T)$, $\mu_{\text{pt}}(T)$ $e(T, n_h(T))$ and $e(T, n_q(T))$

$$
\begin{aligned}
P_{\text{pt}}(T) =& P_{\text{c}}(n_h(T)) + a_h(c_h - 1)T^{b_h} n_h^{c_h}(T) \\
=& P_{\text{c}}(n_q(T)) + a_q(c_q - 1)T^{b_q} n_q^{c_q}(T) \ ,
\end{aligned} \tag{4.35}
$$

$$
\begin{aligned}
\mu_{\text{pt}}(T) =& \mu_{\text{c}}(n_h(T)) + a_h c_h T^{b_h} n^{c_h - 1}(T) \\
=& \mu_{\text{c}}(n_q(T)) + a_q c_q T^{b_q} n^{c_q - 1}(T) \ ,
\end{aligned} \tag{4.36}
$$

$$
e(T, n_h(T)) = e_{c,h}(n_h(T)) + a_h(1 - b_h)T^{b_h} n^{c_h}(T) \tag{4.37}
$$

$$
e(T, n_q(T)) = e_{c,q}(n_q(T)) + a_q(1 - b_q)T^{b_q} n^{c_q}(T) \ . \tag{4.38}
$$

Example phase boundaries

As demonstrated in the previous sections, the thermal EoS part is not completely determined by the cold EoS. For hybrid EoSs this means that a single, cold EoS can have different transition regions at finite temperature depending on the employed thermal model.

As an example, we will consider the following simple two-phase model. For both cold phases, we assume a polytropic EoS, where pressure and chemical potential are given by

$$
p_{\text{c}} = K n^{\Gamma} \tag{4.39}
$$

$$
\mu_{\text{c}} = \frac{K\Gamma}{\Gamma - 1} n^{\Gamma - 1} + E_0 \ . \tag{4.40}
$$

For the phase present at low densities, we pick $\Gamma = 1.8$ and for the high density phase we choose $\Gamma = 2.5$. Additionally, we require the transition region to lie between $n_{\text{on}} = 0.3$ fm^{-3} and $n_{\text{fin}} = 0.5$ fm^{-3} with a chemical potential of $\mu_{\text{pt}} = 1005$ MeV and a pressure of $p_{\text{pt}} = 21$ MeV/fm^3. This fixes the parameters E_0 and K in both cold phases.

For the finite temperature EoS, we use the first solution of Sec. 4.4.1. Hence, we construct the phase boundaries using Eq. (4.31) and Eq. (4.32). We set $\Gamma_{\text{th}} = 1.75$ and $\Gamma_{\text{th}} = 4/3$ for the low and high density phase, respectively, employing typical values for a nucleonic and a deconfined quark matter phase. In both phases, we determine the parameter c using Eq. (4.23) with $m = 931.49$ MeV and set the scaling variables to $n_0 = 1$ fm^{-3} and $T_0 = 1$ MeV. For the low density phase, we use Eq. (4.24) to calculate the parameters a_h and b_h. In the high density phase, we vary a_q and determine the parameter b_q from the relation $\Gamma_{\text{th}} = 1 + a/b$ keeping $\Gamma_{\text{th}} = 4/3$. We compare this simple thermal model to tabulated pressure values of the DD2F-SF EoS sample in the density range between $3.5 \times \rho_{\text{nuc}}$ and $7 \times \rho_{\text{nuc}}$ for temperatures from 10 MeV to 50 MeV. We find that the parameter a roughly varies between $0.1 - 0.85$. We therefore construct four different phase boundaries choosing values from this interval.

The resulting boundaries are plotted in Fig. 4.10 in the $n - T$ plane. Different colors represent results for different values of a_q. We see that within this model, it is possible to produce a variety of different phase boundaries with qualitatively different behaviors at $T > 0$. As an example, for $a_q = 0.389$ the coexistence phase and the onset of the high density phase move towards larger densities with increasing temperature. On the other hand, for $a_q = 0.707$ the curves are strongly shifted towards lower densities at finite temperatures. Recall that the zero temperature EoS is constant for all cases. Hence, as the temperature approaches zero, all boundaries converge towards the same $\rho_{\text{on},0}$ and $\rho_{\text{on},0}$.

The results in Fig. 4.10 clearly demonstrate that the knowledge of the cold EoS does not uniquely fix the transition densities at finite temperatures. We also stress that assuming an ideal-gas like relation between the thermal pressure and energy (Eq. (2.28)) with a constant Γ_{th} for both phases

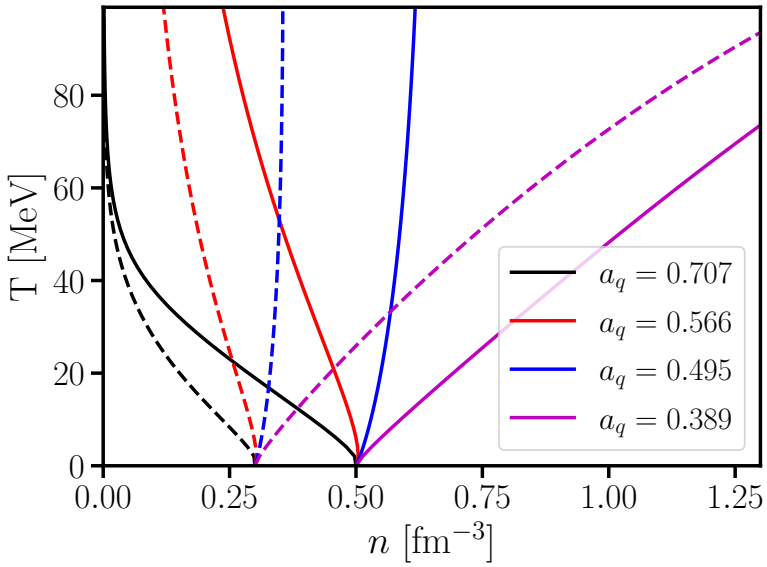

Figure 4.10.: Phase boundaries in the n-T-plane determined with the simple phase transition model for different choices of $\Gamma_{\rm th}$ in the high density phase for a single cold EoS. Different colors refer to different phase boundaries. Dashed lines mark the beginning of the coexisting phases and solid lines display the onset of the high density phases. Figure adapted from Ref. [361]

does also not completely determine the finite-temperature phase boundaries. All shown examples in Fig. 4.10 have $\Gamma_{\rm th} = 1.75$ in the low and $\Gamma_{\rm th} = 4/3$ in the high density phase and qualitatively very different shapes are still possible.

4.4.2. Example 1: DD2F-SF based models

After establishing a motivation to consider different finite-temperature phase boundaries for a fixed, cold EoS, we test the potential impact these variations can have in neutron star mergers. We start by considering the cold, beta-equilibrium composition slice of the DD2F-SF-7 EoS (see Sect. 3.4), which has coexisting phases between $\rho_{\rm on,0} = 3.5 \times \rho_{\rm nuc}$ and $\rho_{\rm fin,0} = 3.7 \times \rho_{\rm nuc}$. For this model, a finite-temperature description exists. We can hence compare results from different phase boundaries to those calculated with the true boundaries inferred from by the model.

We remark, that all phase boundaries of the DD2F-SF models are constructed by fulfilling the Gibbs condition, i.e. matching the pressure P, the baryon chemical potential μ_b and the charge chemical potential μ_c at a given temperature T, $P_1(\mu_b, \mu_c, T) = P_2(\mu_b, \mu_c, T)$. Within the DD2F-SF-7 model, this condition is only satisfied at the true boundaries. There are two points to be made here: Firstly, we stress that the eff PT scheme describes the phase as functions of the specific thermal energy $\epsilon_{\rm th}$. A phase transition on the other hand, is constructed at finite temperature. Within different microphysical EoSs (also hadronic models), there can be substantial variation in $\epsilon_{\rm th}$ at a given temperature and density. Secondly, as stressed before, we point out that the knowledge of the cold EoS does not entirely determine the EoS at finite temperatures. In principle, different models can lead to very similar cold EoS and still vary significantly at finite temperatures. For hybrid EoSs, this can lead to different phase boundaries at $\epsilon_{\rm th} > 0$ even if the onset of quark deconfinement is

similar at $\epsilon_{\text{th}} = 0$.

Phase boundary model

To generate new phase boundaries for the DD2F-SF-7 EoS, we employ the thermal toy model we presented in Sect. 4.4.1. We recall that this model provides a simple, parametric approach to extend a barotropic EoS to finite temperatures while obeying basic thermodynamic relations. As we have demonstrated, this approach is capable of generating qualitatively different phase boundaries at finite temperatures for a fixed, cold EoSs.

In order to construct the phase transition at $T > 0$, the total pressure and chemical potential of both phases need to be matched. For this, an analytic description of the cold EoS part is beneficial. We find that in the density range relevant for the phase transition between $0.1 \times \rho_{\text{nuc}}$ and $3.5 \times \rho_{\text{nuc}}$, the DD2F EoS can be well approximated by a two segment piecewise polytropic model. In this approach, the pressure, chemical potential and energy density of each segment is given by

$$P = K_i n^{\Gamma_i} \,, \tag{4.41}$$

$$\mu = \frac{K_i \Gamma_i}{\Gamma_i - 1} n^{\Gamma_i - 1} + E_{0,i} \,, \tag{4.42}$$

$$e = \frac{K_i}{\Gamma_i - 1} n^{\Gamma_i} + E_{0,i} n \,, \tag{4.43}$$

with $i = 1, 2$. To determine the optimal parameters, we perform a least squares fit to the tabulated, pressure of the barotropic DD2F EoS. We only treat the parameters $\Gamma_{1,2}$ and the density n_1, where the two segments are joined, as free parameters. K_2 and $E_{0,2}$ are constantly adjusted during the fitting process to recover P and μ of the DD2F model at $n = 3.5 \times \rho_{\text{nuc}}$. This ensures that we recover the true onset density of the DD2F-SF-7 EoS at zero temperature. Finally, the parameters K_1 and $E_{0,1}$ are fixed by requiring continuous pressure and energy density.

For the cold quark phase, we find that a piecewise polytropic approach is not suited well since the pressure of pure quark matter is expected to become negative at low densities due to quark deconfinement. Therefore, we describe the cold quark phase using the bag model of Ref. [261]. In this approach, the grandcanonical potential density Ω is given by

$$\Omega = -\left(\frac{3}{4\pi^2} a_4 \mu_q^4 + \frac{3}{4\pi^2} a_2 \mu_q^2 + B_{\text{eff}} \right) \frac{1}{(\hbar c)^3} \,. \tag{4.44}$$

From this we infer

$$P_q = \left(\frac{3}{4\pi^2} a_4 \mu_q^4 - \frac{3}{4\pi^2} a_2 \mu_q^2 - B_{\text{eff}} \right) \frac{1}{(\hbar c)^3} \,, \tag{4.45}$$

$$n_q = \left(\frac{3}{\pi^2} a_4 \mu_q^3 - \frac{3}{2\pi^2} a_2 \mu_q \right) \frac{1}{(\hbar c)^3} \,, \tag{4.46}$$

$$e_q = \left(\frac{9}{4\pi^2} a_4 \mu_q^4 - \frac{3}{4\pi^2} a_2 \mu_q^2 + B_{\text{eff}} \right) \frac{1}{(\hbar c)^3} \,. \tag{4.47}$$

Here, μ_q and n_q refer to the quark chemical potential and number density, respectively. We assume $3\mu_q = \mu$ and $n_q = 3n$. We fit this model to the tabulated DD2F-SF-7 EoS in the density range between $3.7 \times \rho_{\text{nuc}}$ and $15 \times \rho_{\text{nuc}}$. To recover the correct ρ_{fin} at $n = 3.7 \times n_{\text{nuc}}$, P and μ have to be fixed to the values of the tabulated DD2F-SF-7 EoS at this density. We achieve this by only treating

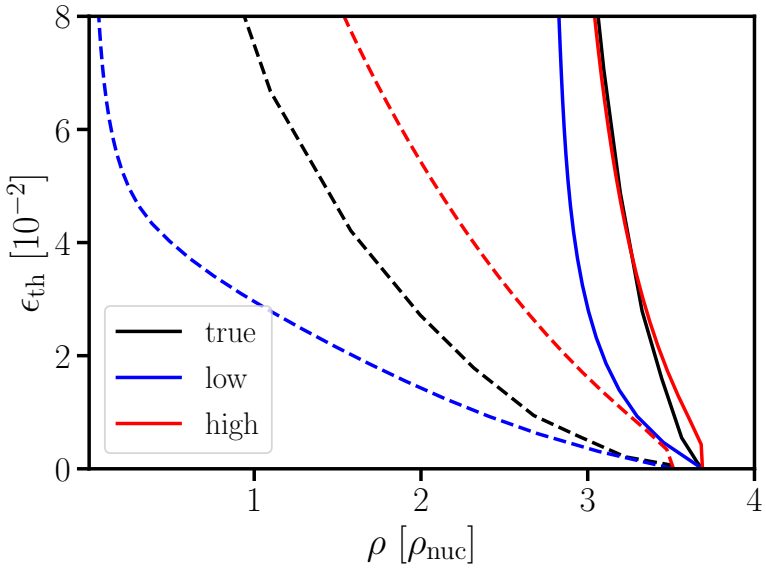

Figure 4.11.: Newly constructed phase boundaries in the n-$\epsilon_{\rm th}$-plane with our simple thermal EoS model (see Sect. 4.4.1) for the DD2F-SF-7 EoS. Different colors refer to different phase boundaries. Dashed lines mark the beginning of the coexisting phases and solid lines display the onset of pure deconfined quark matter. The nomenclature corresponds to the merger results shown in Fig. 4.12. Model true refers to the original phase boundaries of the DD2F-SF-7. Figure adapted from Ref. [361].

a_4 as a free parameter during the fitting and constantly updating a_2 and $B_{\rm eff}$ depending on the current value of a_4.

For the finite temperature part, we employ the first solution from our thermal toy model discussed in Sect. 4.4.1. We pick $\Gamma_{\rm th} = 1.75$ for the hadronic phase and $\Gamma_{\rm th} = 4/3$ for the deconfined quark phase. For a specific choice of the parameter a in each phase, the condition $\Gamma_{\rm th} = 1 + a/b$ then fixes the value of b.

To infer reasonable values for the parameters a and c in both phases, we determine values of these parameters from the EoS tables of the hadronic DD2F and the hybrid DD2F-SF models using the pressures and the chemical potentials. Considering the temperature range from 10 MeV to 50 MeV, we find values of a from 0.1 to 1.5 and values of c from 0.4 to 20 for the DD2F EoS in the density interval from $0.1 \times \rho_{\rm nuc}$ to $3.5 \times \rho_{\rm nuc}$. In the DD2F-SF sample, we observe that a lies between 0.1 to 0.85 and c between 0.9 and 11 in density interval from $3.5 \times \rho_{\rm nuc}$ to $7.0 \times \rho_{\rm nuc}$ and same temperature range.

Motivated by these observations, we pick two different sets of parameters leading to two different phase boundaries. For the first, set we choose $a_h = 1.060$ and $c_h = 8.456$ and $a_q = 0.707$ and $c_q = 6.256$. For the second parameterizations, we set $a_h = 1.167$ and $c_h = 7.356$ and $a_q = 0.658$ and $c_q = 7.356$.

With these descriptions of the cold and the thermal parts of our two EoS phases, we construct the phase boundaries at finite temperatures using Eq. (4.35) and Eq. (4.36). To also determine the boundaries in the $\epsilon_{\rm th} - n$ plane, we calculate the energies at the phase boundaries with Eq. (4.37) and Eq. (4.38).

We plot the two newly constructed and the original boundaries in the $\epsilon_{\rm th}$-n-plane in Fig. 4.11 in

blue, red and black, respectively. Dashed (solid) lines mark the beginning (end) of the coexistence phase. For comparisons, we refer to the boundaries from the original DD2F-SF-7 EoS as "model true".

We see that our first parameterization produces boundaries that shift the coexistence region to lower densities compared to model true, hence we refer to this model as "model low". This behavior mimics an "earlier" onset of quark deconfinement compared to the original EoS. As an example, at $\epsilon = 0.04$ we find $\rho_{\text{on}} = 0.50 \times \rho_{\text{nuc}}$ and $\rho_{\text{fin}} = 2.92 \times \rho_{\text{nuc}}$, whereas model true has $\rho_{\text{on}} = 1.64 \times \rho_{\text{nuc}}$ and $\rho_{\text{fin}} = 3.25 \times \rho_{\text{nuc}}$.

The second parameterization moves the onset of quark deconfinement at finite thermal energies to larger densities, while keeping the onset of pure quark matter almost identical to the original boundaries. This model hence describes a "later" deconfinement onset at finite temperature. We will refer to this result as "model high". At $\epsilon = 0.04$, we have $\rho_{\text{on}} = 2.31 \times \rho_{\text{nuc}}$ and $\rho_{\text{fin}} = 3.25 \times \rho_{\text{nuc}}$.

We also remark that, as desired, all three sets of boundaries approach each other at small ϵ_{th} and thus result in identical $\rho_{\text{on},0}$ and $\rho_{\text{fin},0}$.

Merger simulations

We now perform neutron star simulations employing the two newly constructed sets of finite-temperature phase boundaries (models low and high) together with the barotropic DD2F-SF-7 EoS slice. As before, we simulate symmetric binaries with total system masses of $2.7\ M_\odot$. We plot results from these two simulations together with the results from "model true", i.e. when using the true phase boundaries of the DD2F-SF-7 EoS in our effPT scheme, in Fig. 4.12.

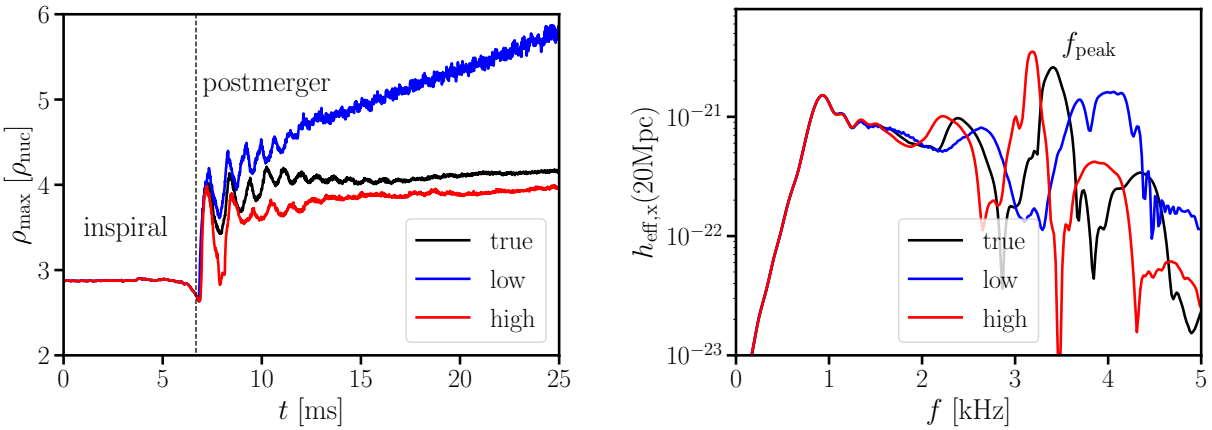

(a) (b)

Figure 4.12.: (a): Evolution of the maximum rest-mass density for the merger of two $1.35\ M_\odot$ NSs using the DD2F-SF-7 EoS. Different colors represent the different assumed shapes of the phase boundaries at finite temperature as shown in Fig. 4.11. The EoS at zero temperature is identical for all three cases. (b): Gravitational-wave spectrum of the cross polarization at a distance of 20 Mpc along the polar axis for the same simulations as in (a). Both figures adapted from Ref. [361].

Fig. 4.12(a) shows the time evolution of the maximum densities during the simulations. We see that in the inspiral phase the densities in all three models are identical. This is plausible, as

the systems remains cold in this stage of the simulations. After the merger, the densities begin to deviate from each other.

As expected, we find that the model low leads to larger and model high to smaller postmerger densities compared to model true due to the "earlier"/"later" onset of quark deconfinement at finite temperatures. Figure 4.12(b) depicts the corresponding gravitational-wave spectra for all three simulations. We see that the differences in remnant structure clearly manifest themselves in the gravitational-wave signals. While the low frequency inspiral parts (roughly below 1.5 kHz) of the spectra are almost identical, strong differences emerge at higher frequencies caused by postmerger emission. Namely, we find that f_{peak} of model low is about 650 kHz larger than of model true. Conversely, the value of model high is about 220 kHz smaller than the f_{peak} of model true making it comparable to the result from the ideal-gas scheme (compare Table 4.2). These shifts are considerably larger than finite temperature effects reported in works considering purely nucleonic models, see e.g. [22, 352, 353, 354, 355].

Our results demonstrate that the exact behavior of a first-order phase transition at finite temperatures can potentially have a large impact on postmerger observables such as f_{peak}. Therefore, the shape of the phase boundaries should be regarded as a crucial degree of freedom in neutron star mergers, as can be very important to correctly link merger observations to the microphysical EoS.

4.4.3. Example 2: piecewise polytropic models with low onset densities

We now consider EoS models from the literature, as our eff PT approach provides the flexibility to be used alongside any cold, hybrid model. This means that we can equip models studied in other works with potentially more realistic finite-temperature phase boundaries than simply assuming constant onset densities and fixed density jumps at all temperatures. As we have already established, the behavior of the hadron-quark phase transition can have a considerable impact on the postmerger dynamics in neutron star mergers. It is therefore interesting to study how the findings from other works change, when different phase boundary shapes are assumed.

We start by considering the EoS from Ref. [319]. In this work, the authors construct a piecewise-polytropic model to represent a hybrid EoS with a relatively low onset density of $2.085\ \rho_{\text{nuc}}$ followed by a large, soft coexisting phase and a stiff pure quark phase beginning at $4.072\ \rho_{\text{nuc}}$. The hadronic phase below the coexistence region is described by a piecewise polytropic representation of the relativistic mean field model FSU2H [419, 387]. Thermal effects were included with the ideal-gas approach using a constant $\Gamma_{\text{th}} = 1.75$ at all densities.

With this model, the authors observe a so-called delayed phase transition scenario in a small mass range. In these systems, the phase transition occurs in the remnant a few milliseconds after the merger resulting in a rapid density increase. This delayed transition produced a sudden increase in the dominant postmerger GW frequency leading to two distinct peaks in the spectrum. Such a strong shift could serve as a clear, observational indication to identify a phase transition in the remnant complementary to ideas from [52, 53] based on combining observations from pre- and postmerger GWs.

Since we also observe such a delayed transition in Sect. 4.3.2 for some DD2F-SF models when employing the ideal-gas approach, but not when using the 3D EoS table or the eff PT scheme, we investigate the impact of different phase boundaries on this model with our eff PT scheme.

Phase boundary model

Since this EoS only exists as a piecewise polytropic model, no microphysical finite temperature description and hence no true phase boundaries of this model are available. Furthermore, the phase transition was not constructed in a consistent way, i.e. matching pressure and chemical potential of both phases. We find a difference of about 80 MeV in the chemical potential at the borders of the coexistence phase. Because of these inconsistent chemical potentials, we cannot employ our thermal toy model to construct phase boundaries as these would not converge to the given boundaries at zero temperature. Instead, we pick a functional form somewhat similar to the form of the DD2F-SF boundaries. For the onset of quark deconfinement, we pick a hyperbola

$$\epsilon_{\mathrm{on}}(\rho) = \frac{1}{a_{\mathrm{on}}\rho + b_{\mathrm{on}}} + c_{\mathrm{on}} \quad \forall \rho < \rho_{\mathrm{on}} \ , \tag{4.48}$$

where ρ refers to the rest-mass density. As in the previous section, we test two different sets of parameters for the phase boundaries. For the first set of parameters we choose $a_{\mathrm{on}} = 10065.12$, $b_{\mathrm{on}} = 3.420353$ and $c_{\mathrm{on}} = -0.083468$, we refer to this set as "eff PTlow".

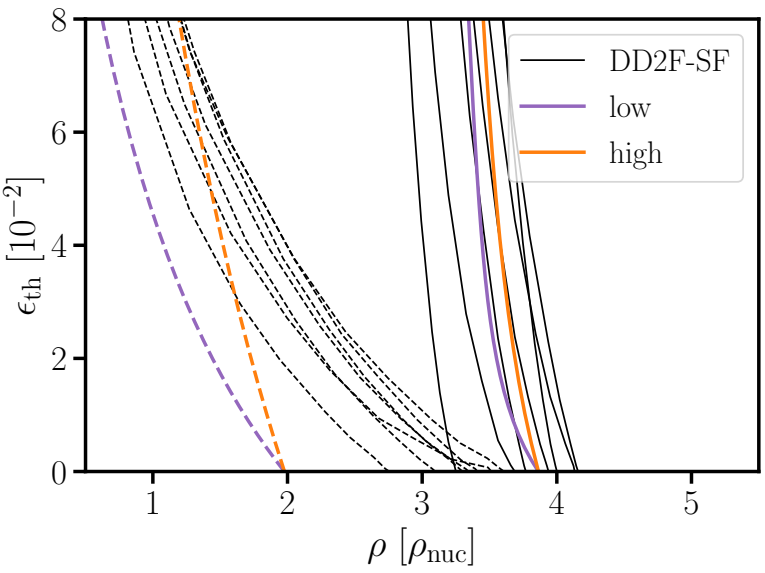

Figure 4.13.: Two newly developed phase boundaries in the n-ϵ_{th}-plane for the piecewise polytropic EoS of Ref. [319]. See text for details on the functional form. Different colors refer to different phase boundaries. Dashed lines mark the beginning of the coexisting phases and solid lines display the onset of pure deconfined quark matter. The thin black lines show the boundaries of the DD2F-SF EoSs for comparison.

For the second set of parameters we pick $a_{\mathrm{on}} = 4065.12$, $b_{\mathrm{on}} = 1.420353$ and $c_{\mathrm{on}} = -0.205015$. This results in a weaker bending of the phase boundaries towards lower densities with increasing ϵ_{th} compared to our first choice. We refer to these boundaries as "eff PThigh". Both choices reproduce the correct onset density of the cold EoS $\rho_{\mathrm{on},0} = 2.085 \times \rho_{\mathrm{nuc}}$.

Recall that the eff PT scheme uses linear interpolation to construct the pressure in the coexistence phase at finite ϵ_{th} (see Sect. 4.2.2). When picking the phase boundaries by hand, this can easily result in a negative slope of the EoS at finite ϵ_{th}. We therefore construct the boundary of the pure

deconfined quark matter phase by setting the slope of this linear interpolation at every $\epsilon_{\rm th}$ equal to the slope of the EoS in the coexisting phases at $T = 0$, i.e.

$$\frac{P_{\rm fin}(\epsilon_{\rm th}) - P_{\rm on}(\epsilon_{\rm th})}{\rho_{\rm fin}(\epsilon_{\rm th}) - \rho_{\rm on}(\epsilon_{\rm th})} = \frac{P_{\rm fin,0} - P_{\rm on,0}}{\rho_{\rm fin,0} - \rho_{\rm on,0}} \quad \forall \epsilon_{\rm th} \ . \tag{4.49}$$

This ensures that for a fixed $\epsilon_{\rm th}$ the pressures constructed by the eff PT scheme never decrease with density.

We plot the two resulting phase boundaries in the $\rho - \epsilon_{\rm th}$ plane with different colors in Fig. 4.13. For comparison, we also show the boundaries of all DD2F-SF models with thin, dashed lines. As indicated before, the eff PTlow set leads to a stronger shift of the boundaries towards lower densities compared to the eff PThigh set. As an example, at $\epsilon_{\rm th} = 0.03$ we infer $\rho_{\rm on} = 1.24 \times \rho_{\rm nuc}$ and $\rho_{\rm fin} = 3.51 \times \rho_{\rm nuc}$ for the eff PTlow boundaries and $\rho_{\rm on} = 1.62 \times \rho_{\rm nuc}$ and $\rho_{\rm fin} = 3.63 \times \rho_{\rm nuc}$ for the eff PThigh boundaries. We also see that although the model of Ref. [319] has a lower onset density and a larger coexistence region at $T = 0$ than the DD2F-SF EoSs, the phase boundaries we have chosen follow the general trend of the DD2F-SF boundaries at $\epsilon_{\rm th} > 0$ relatively well.

Merger simulations

We perform two simulations with the EoS from Ref. [319] and our eff PT approach using the two boundaries eff PTlow and eff PThigh presented in the previous subsection. We refer to these simulations as eff PTLow and eff PTHigh simulations, respectively.

Additionally, we perform one simulation with the ideal-gas scheme, where we employ three different values of $\Gamma_{\rm th}$ according to the phase of the cold EoS at the considered density (as in Sect. 4.3.1). We refer to this simulation as $\Gamma_{\rm th}$ simulation. As before, we simulate symmetric binaries with total system masses of $2.7\ M_\odot$ in all three simulations.

We plot the results from the three simulations in Fig. 4.14 with different colors. The lower panel of Fig. 4.14(a) shows the time evolution of the maximum density in all cases. Dashed horizontal lines mark the edges of the coexistence phase at zero temperature. As expected, we see that the densities are virtually identical during the inspiral, while differences emerge after the merger. Using the $\Gamma_{\rm th}$ framework, we see a similar trend as the authors of Ref [319]. Around 3 milliseconds after the initial density increase at the merger, a delayed phase transition occurs in the remnant indicated by the strong density increase crossing the value of $\rho_{\rm on,0}$. For the eff PTLow simulation, we observe a different behavior. Here, matter enters the pure deconfined quark phase right after the merger. The densities in this simulation are also larger than in the $\Gamma_{\rm th}$ simulation. This finding is similar to our observations in Fig. 4.7(a) with the DD2F-SF-7 EoS. For the eff PThigh simulation, we also see a delayed transition in the remnant, however, in this model the time between the merger and the appearance of quark matter in the remnant is shorter compared to the $\Gamma_{\rm th}$ simulation.

These differences in the postmerger remnant behavior also manifest themselves in the gravitational-wave signal. We show the spectra of all three simulations in Fig. 4.14(b). The $\Gamma_{\rm th}$ simulation produces a large peak at 2.65 kHz and several smaller peaks at larger frequencies up to 3.68 kHz. For the eff PThigh simulation, we observe a similar spectrum as the authors of Ref [319]. We find two distinct peaks, where one peak sits at a frequency of 2.72 kHz and is hence very close to the peak in the spectrum of the $\Gamma_{\rm th}$ simulation. The second peak is at significantly higher frequencies of 4.08 kHz. For the eff PThigh simulation, where matter enters the quark phase right after the merger, we find that the high frequency part of the spectrum is significantly shifted towards larger frequencies compared to the $\Gamma_{\rm th}$ simulation. In contrast to the eff PThigh simulation, we do not

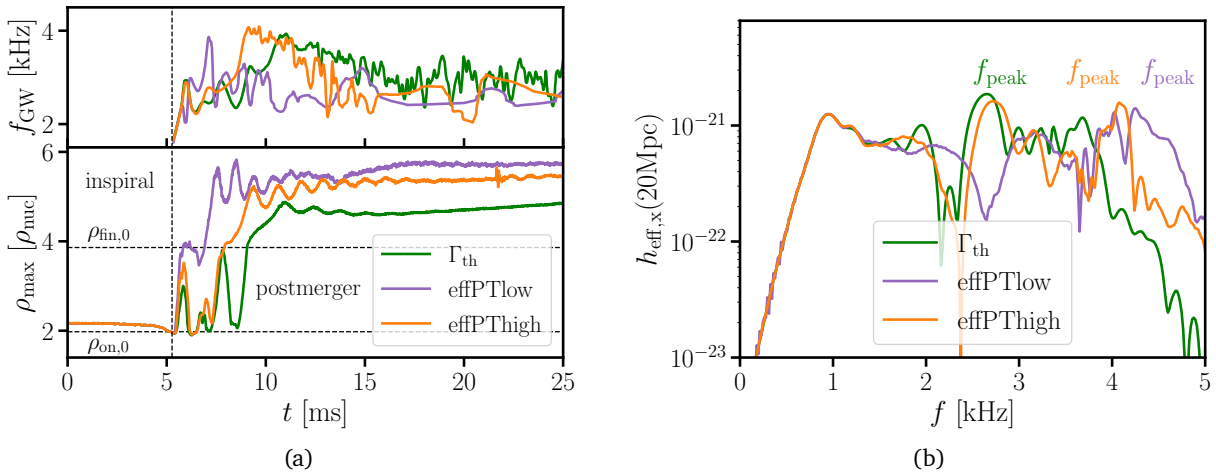

Figure 4.14.: (a): Top: Instantaneous gravitational-wave frequency for the merger of two $1.35\ M_\odot$ NSs using the piecewise polytropic EoS model of [319]. Different colors represent the different frameworks outlined in the text to model the finite-temperature EoS regime. Bottom: Corresponding evolution of the maximum rest-mass density. (b): Gravitational-wave spectrum of the cross polarization at a distance of 20 Mpc along the polar axis from the same simulations as in (a). Both Figures adapted from Ref. [361].

find two distinct peaks. Instead, we observe a split peak structure at 4.24 kHz and 4.03 kHz, which is close to the high frequency peak from the effPTlow simulation. These frequencies are roughly 1.6 kHz larger than $f_{\rm peak}$ of the $\Gamma_{\rm th}$ simulation. This is much greater shift than the differences we found for the DD2F-SF models when employing the effPT and the $\Gamma_{\rm th}$ framework. The reason for this larger increase could be related to the properties of this model, in particular the larger extend of the mixed phase, or to our choice of phase boundaries.

In addition to the delayed phase transition, Refs. [420, 421] report that the oscillations observed in the maximum density are correlated with the instantaneous GW frequency $f_{\rm GW}$. To see how this correlation may be affected by the finite-temperature phase boundaries, we calculate $f_{\rm GW} = \frac{1}{2\pi}\frac{{\rm d}(\phi(t))}{{\rm d}t}$ with $\phi(t) = \arctan({\rm h}_\times(t)/{\rm h}_+(t))$, where $\rm h_\times$ and $\rm h_+$ are the cross and the plus polarized components of the GW signal for all three cases. The upper panel of Fig. 4.14(a) shows the results. We do see similarities in the general trends of $f_{\rm GW}$ and $\rho_{\rm max}$ and find that some peaks in $f_{\rm GW}$ coincide with local maxima of the density. However, the overall correlation between $f_{\rm GW}$ and $\rho_{\rm max}$ is not too strong, in particular for the effPTlow simulation. Reference [421] also noted that the detailed behavior of $\rho_{\rm max}$ is very sensitive to numerical details.

The results from this section clearly show that the occurrence and timescale of a delayed phase transition in the merger remnant as well its impact on the GW signal critically depend on the phase boundaries at finite $\epsilon_{\rm th}$. Hence, simulations with hybrid models that do not account for finite-temperature effects beyond the ideal-gas approach are potentially neglecting important physics, which cannot be captured with this simplified treatment.

4.4.4. Example 3: Models with high onset densities and unstable hybrid branch

So far, we have considered EoS models allowing for stable hybrid stars. We demonstrated that the finite-temperature behavior of the phase boundaries can significantly affect the dynamics and observables of a neutron star merger such as f_{peak}. In this section, we consider the EoS of Ref. [327] where the onset of the phase transition occurs at very high densities and no stable hybrid stars exist. This model is a piecewise polytropic EoS with a large density jump mimicking a first-order phase transition. The parameters of the hadronic and the deconfined quark phase are chosen to agree with current constraints from perturbative QCD and nuclear physics constrains. The phase transition is modeled by requiring equal pressure in the deconfined quark and the hadronic phase at a pressure of 0.5 GeV/fm^3 and assuming a constant pressure in the coexistence region. The onset of quark deconfinement occurs at relatively large densities ($\rho_{\mathrm{on},0} = 5.36 \times \rho_{\mathrm{nuc}}$), which corresponds to the central density of a $2.29\ M_\odot$ NS.

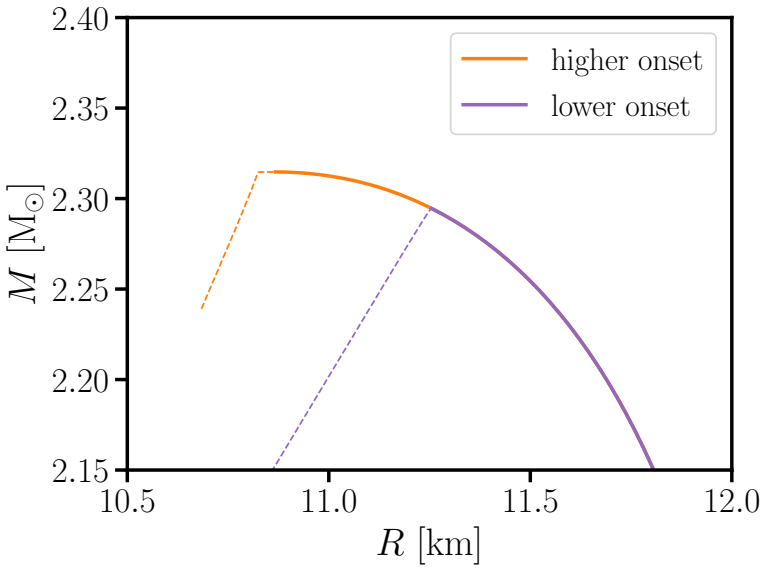

Figure 4.15.: Mass-radius relations for the piecewise polytropic model of Ref. [327] (lower onset) mimicking a strong first-order phase transition to deconfined quark matter that ends the mass-radius curve. In addition, we show a modified version of this EoS with higher onset of quark deconfinement (higher onset), where the phase transition sets in just after the maximum mass is reached. See text for details. Dashed lines mark unstable configurations. Figure adapted from Ref. [361].

Based on this model, we create an additional EoS by shifting the onset density to $\rho_{\mathrm{on},0} = 6.22 \times \rho_{\mathrm{nuc}}$. By matching the pressure of the hadronic part at this density to the pressure of the deconfined quark phase we find $\rho_{\mathrm{fin},0} = 11.99 \times \rho_{\mathrm{nuc}}$.

We refer to this modified model as "higher onset" and to the original EoS from Ref. [327] as "lower onset". Fig. 4.15 shows the mass-radius curves of both EoSs, unstable stars are marked by dashed lines and stable stars by solid lines. We find that for the lower onset EoS, the beginning of the phase transition ends the mass-radius curve due to the sudden strong softening of the EoS. Since no stable hybrid stars exist for this EoS, the mass-radius relation of stable stars does not reach the typical high-mass regime where $\frac{dM}{dR}$ smoothly approaches zero (compare e.g. Fig. 3.1). Such a sudden end of stable, non-rotating NSs could in principle be measured and hence reveal

the presence of deconfined quark matter. However, this would require very precise mass-radius measurements in a very narrow mass range, which will pose a serious challenge.

On the other hand, for the higher onset model we see that the mass-radius curve does approach the maximum mass with $\frac{dM}{dR}$ smoothly going to zero. In this case, no observations of isolated neutron star could reveal the onset density of the quark hadron phase transition.

The general expectation for models with no stable quark branch is that the merger remnant should collapse once the onset densities are reached. The authors of Ref. [327] find no impact of the phase transition in their simulations, as the onset densities are not reached in the system. We will now explore this scenario for the case of strongly shifting phase boundaries at finite temperatures.

Phase boundary model

As in our second example (Sect.4.4.3), the two models we consider only exist as a barotropic, piecewise polytropic EoSs and hence no true phase boundaries are available. The phase transitions were also not constructed by matching pressure and chemical potential. Therefore, we use same procedure as in Sect.4.4.3 to calculate the finite-$\epsilon_{\rm th}$ phase boundaries for these models. For the lower onset model, we pick the parameters $a_{\rm on} = 10065.12$, $b_{\rm on} = 3.420353$ and $c_{\rm on} = -0.037540$ for Eq. (4.48) to ensure the correct $\rho_{\rm on,0} = 5.36 \times \rho_{\rm nuc}$ and $\rho_{\rm fin,0} = 8.91 \times \rho_{\rm nuc}$. For the higher onset EoS, we set $a_{\rm on} = 10065.12$, $b_{\rm on} = 3.420353$ and $c_{\rm on} = -0.032931$ reproducing $\rho_{\rm on,0} = 6.22 \times \rho_{\rm nuc}$ and $\rho_{\rm fin,0} = 11.99 \times \rho_{\rm nuc}$ as $\epsilon_{\rm th} \to 0$.

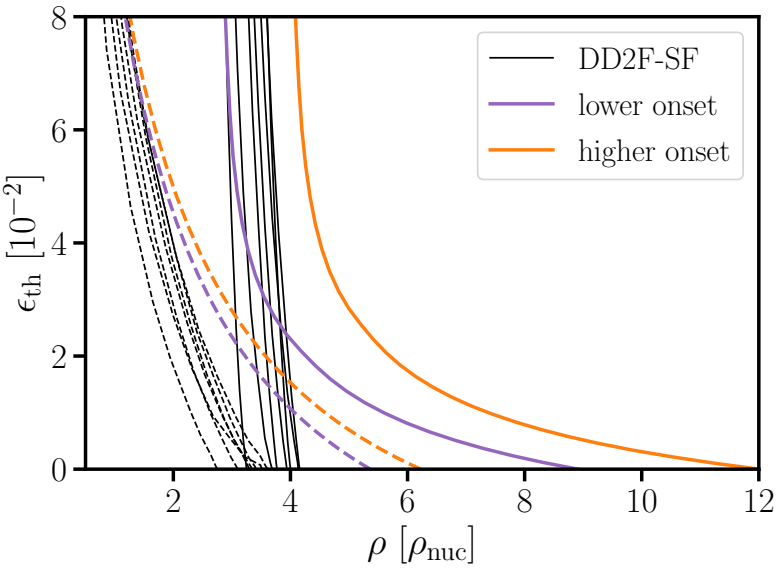

Figure 4.16.: Two newly constructed phase boundaries in the n-$\epsilon_{\rm th}$-plane for the piecewise polytropic EoS of Ref. [327] (lower onset) and a modified version with higher onset density (higher onset). See text for details on the construction. Dashed lines mark the beginning of the coexisting phases and solid lines display the onset of pure deconfined quark matter. The thin dashed lines show the boundaries of the DD2F-SF EoSs for comparison.

We plot the resulting phase boundaries with different colors in the ρ-$\epsilon_{\rm th}$ plane in Fig. 4.16. Dashed lines mark the onset of quark deconfinement and solid lines the beginning of the pure quark phase.

For comparison, we also plot the boundaries of the DD2F-SF EoSs. We see that our parameterization strongly shifts the phase boundaries to lower densities at finite $\epsilon_{\rm th}$ and reduces the size of the coexistence phase. For example, at $\epsilon_{\rm th} = 0.03$ we find $\rho_{\rm on} = 2.63 \times \rho_{\rm nuc}$ and $\rho_{\rm fin} = 3.57 \times \rho_{\rm nuc}$ for the lower onset model and $\rho_{\rm on} = 2.88 \times \rho_{\rm nuc}$ and $\rho_{\rm fin} = 4.91 \times \rho_{\rm nuc}$ for the higher onset model. At larger $\epsilon_{\rm th}$, the boundaries somewhat approach those of the DD2F-SF models.

Merger simulations

To explore the high onset scenario with strongly shifted phase boundaries, we perform three additional simulations. In the first simulation, we employ the traditional $\Gamma_{\rm th}$ approach with the EoS from Ref. [327], i.e. the lower onset model. However, as in the previous sections we pick $\Gamma_{\rm th} = 1.75$, $\Gamma_{\rm th} = 1.4$ and $\Gamma_{\rm th} = 4/3$ at densities corresponding to the hadronic, the coexistence and the deconfined quark phase. Hence, in this simulations we do not account for temperature-dependent onset densities. We omit to simulate the higher onset model with the $\Gamma_{\rm th}$ approach as $\rho_{\rm on,0}$ would not be reached in this scheme. In the two other simulations, we employ the lower and the higher onset density model with our effPT scheme using the phase boundaries we calculated in the previous subsection for each EoS. We simulate 1.4-1.4 $M_\odot$ NSs mergers in all simulations.

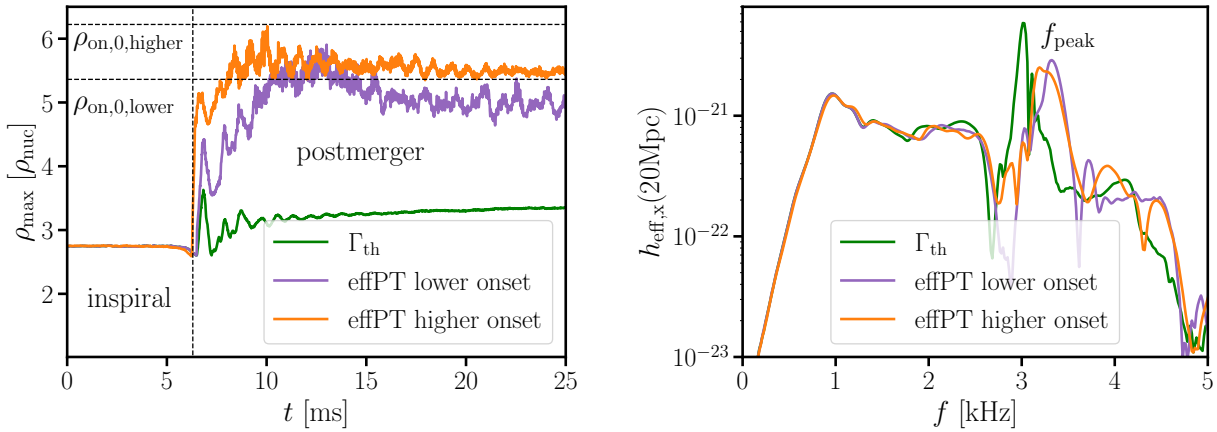

(a) (b)

Figure 4.17.: (a): Top: Evolution of the maximum rest-mass density for the merger of two $1.4\ M_\odot$ NSs using the piecewise polytropic EoS model of [327] (lower onset) and a modified version with higher onset density using the effPT approach for modeling the finite temperature effects. The employed finite-temperature phase boundaries are shown in Fig. 4.16. Horizontal, dashed lines mark the onset densities of both EoSs at $\epsilon_{\rm th} = 0$. Additionally, we plot a results from a simulation employing the $\Gamma_{\rm th}$ framework. In this approach, no differences between the two EoS emerge. (b): Gravitational-wave spectrum of the cross polarization at a distance of 20 Mpc along the polar axis from the same simulations as in (a).

In Fig. 4.17(a), we show the maximum densities in the systems as a function of time. Additionally, we mark the onset densities at $\epsilon_{\rm th} = 0$ with horizontal dashed lines. As in previous sections, we find that prior to the merger the densities are identical as different finite temperature treatments are inconsequential in this evolution stage. After the merger, the curves start to deviate from each other. For the simulations employing the $\Gamma_{\rm th}$, we see that the densities stay well below $\rho_{\rm on,0}$ of

the EoS models. Since the two EoS models are identical at densities below $\rho = 5.36 \times \rho_{\text{nuc}}$ in this framework and these densities are not reached in the system, the results from both simulations with the Γ_{th} approach would be identical.

For the simulations with the eff PT scheme, we see a strong density increase at the merger. This increase is significantly larger than for the Γ_{th} simulation. We find that the higher onset EoS leads to larger densities than the lower onset EoS. Both simulations also show more pronounced oscillation in the maximum density than the Γ_{th} approach.

Fig. 4.17(b) shows the gravitational-wave spectra of all three simulations. As expected, we find that the low frequency parts are very similar, but differences emerge in the high frequency part namely in the dominant postmerger frequency. For the Γ_{th} simulation, we infer $f_{\text{peak}} = 3.02$ kHz, for the eff PT lower onset model we get $f_{\text{peak}} = 3.32$ kHz and for the eff PT higher onset system, we obtain $f_{\text{peak}} = 3.19$ kHz.

The increased postmerger densities and postmerger GW frequencies when employing the eff PT scheme compared to the Γ_{th} approach clearly indicate that deconfined quark matter is present in the remnants of the eff PT simulations for both EoSs. This is interesting, as both models do not permit stable cold, non-rotating NSs containing deconfined quark matter. The reason for this behavior is the strong decrease in the onset density caused by our phase boundaries and hence the "earlier" onset of quark deconfinement. Our finding is especially intriguing for the higher onset EoS as it demonstrates that even if the quark hadron phase transition takes place at densities not present in stable NSs at $T = 0$, it could still be accessible in NS mergers. The requirement is that the onset densities are lowered significantly at the temperatures reached in merger remnants. Again, these results demonstrate the relevance of finite temperature effects of the QCD phase diagram for interpreting GW signals from NS mergers.

To further corroborate our finding, we perform two additional simulations with symmetric binaries employing the higher onset EoS at a slightly larger binary mass of $2.86\ M_{\odot}$ using the eff PT and the Γ_{th} scheme, respectively. Here we find $f_{\text{peak}} = 3.06$ kHz in the Γ_{th} simulation and $f_{\text{peak}} = 3.42$ kHz in the eff PT simulation, i.e. the difference in dominant postmerger frequency is even more pronounced than at a binary mass of $2.8\ M_{\odot}$.

Threshold mass for prompt collapse

In addition to comparing dominant gravitational-wave frequencies with and without temperature-dependent phase boundaries, we also determine the threshold mass M_{thres} for direct black hole formation at merger for both EoSs with the eff PT and the Γ_{th} approach, respectively. A prompt collapse of the remnant is characterized by a continuous decrease of the lapse function after the two stars collide with no oscillatory behavior. For the lower onset EoS, we get $M_{\text{thres}} = 3.07\ M_{\odot}$ with the Γ_{th} approach and $M_{\text{thres}} = 2.97\ M_{\odot}$ with the eff PT scheme. For the higher onset EoS, we find $M_{\text{thres}} = 3.07\ M_{\odot}$ with the ideal-gas approach and $M_{\text{thres}} = 3.01\ M_{\odot}$ with the eff PT framework. We see that in both cases M_{thres} is slightly reduced in the eff PT simulations compared to the Γ_{th} simulations. Also note that M_{thres} is identical for both EoSs when employing the traditional Γ_{th} treatment. In these simulations, we find that no stable remnants with quark matter exist and the maximum densities in systems not directly collapsing are too low to reveal differences between the lower and higher onset model.

In a next step, we compare the inferred threshold masses with the bilinear fits of Ref. [29]. These fits relate M_{thres} to different quantities of nonrotating star such as NS radii, tidal deformabilities and the maximum mass M_{max}. We consider the fits from a set of purely hadronic EoS compatible with current observations (set "b" in Ref. [29]) to search for deviations that could be indicative of

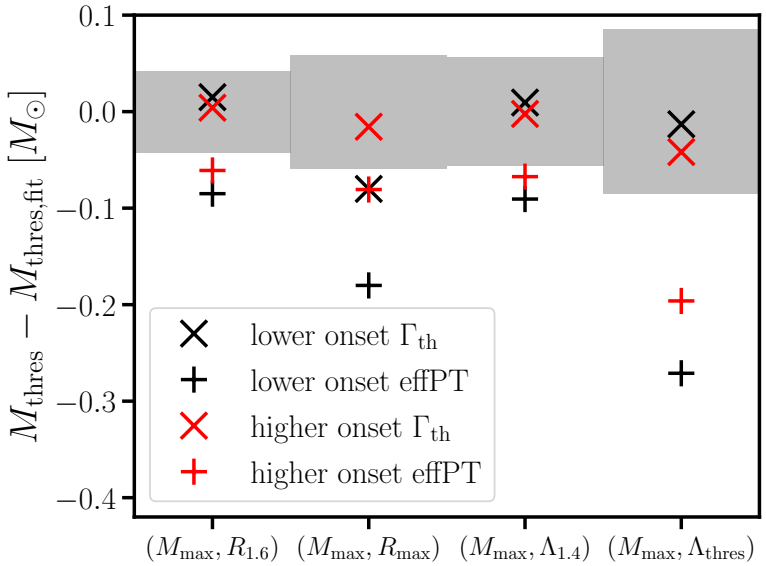

Figure 4.18.: Deviations of $M_{\rm thres}$ from different bilinear fits $M_{\rm thres,fit}(X, Y)$ with X being $M_{\rm max}$ and Y being either $R_{1.6}$, $R_{\rm max}$, $\Lambda_{1.4}$ or $\Lambda_{\rm thres}$. Fits are taken from [29]. The gray bands indicate the respective maximum residual of the fit for purely hadronic EoS models (see [29] for details). The respective pair of independent variables (X, Y) is given on the x-axis. Black symbols display the differences for the EoS from Ref. [327] (lower onset), red symbols refer to the modified version with higher onset density. Crosses indicate the calculations with the $\Gamma_{\rm th}$ approach. Results with the effPT scheme, i.e. with temperature-dependent phase boundaries, are displayed by plus signs. Figure adapted from Ref. [361].

the presence of deconfined quark matter in the systems.

We plot the differences between $M_{\rm thres}$ we infer from our simulations and the value predicted by the 4 different bilinear relations from Ref. [29] for the higher and lower onset EoS with both the $\Gamma_{\rm th}$ and the effPT scheme, respectively, in Fig. 4.18. Additionally, we mark the maximum residuals of each fit given in Ref. [29] to quantify the range of threshold masses hadronic EoS are expected to provide. We see that when employing the $\Gamma_{\rm th}$ scheme, i.e. not accounting for different onset densities at finite temperatures, $M_{\rm thres}$ generally agrees well with the values predicted by the bilinear relations for both EoSs. In this case, the presence of deconfined quarks in the EoSs could not be inferred from a measurement of the threshold mass. This is understandable, as in these systems no deconfined quark matter is present prior to the onset of collapse.

When using the effPT approach together with our choice of phase boundaries, we find that $M_{\rm thres}$ is systematically reduced compared to what one would expect for purely hadronic EoS. A precise measurement of $M_{\rm thres}$ in combination with properties of cold, isolated neutron stars could hence reveal the presence of deconfined quark matter in merger remnants even in cases of a high onset density of quark deconfinement. This is particularly interesting since signatures of deconfined quark matter would be very difficult or even impossible to detect from the observation of isolated NSs. This would, however, require a relatively strong shift of the onset densities at finite temperatures.

These findings demonstrate that postmerger features such as $f_{\rm peak}$ and $M_{\rm thres}$ enlarge the param-

eter range where deconfined quark matter may be detectable. We remark that similar effects are expected in a less extreme scenario, where a small, but stable hybrid branch of neutron stars exist. In this case, the most massive NSs will contain a quark matter core, however, clear signatures of deconfined quark matter would likely still be challenging to detect. Also, such massive stars are not expected to be very common. One can anticipate that in this case temperature-dependent phase boundaries will have a similar impact on merger remnants and hence affect the postmerger GW signal in a similar way.

5. Results: Impact of thermal effects in neutron star mergers for hyperonic EoS

In this chapter, we perform a comprehensive study on the effect of hyperons in neutron star mergers. In particular, we focus on the differences at finite temperatures compared to purely nucleonic models. Based on our findings, we will discuss potential observable signatures which can be directly linked to the presence of hyperons in merger remnants. This is of particular interest, as the hyperon puzzle (see Sect. 1.2.2) is still unresolved in the sense that it is still not know whether hyperons occur in neutron stars (NSs). The content of this chapter is based on the results presented in Ref. [360].

5.1. Mass-radius curves of hyperonic and nucleonic EoSs

In Fig. 5.1(a), we plot the mass-radius MR curves of all equations of state (EoSs) from the purely nucleonic sample introduced in Sect. 3.2 and the hyperonic sample presented in Sect. 3.3 with black and green lines, respectively.

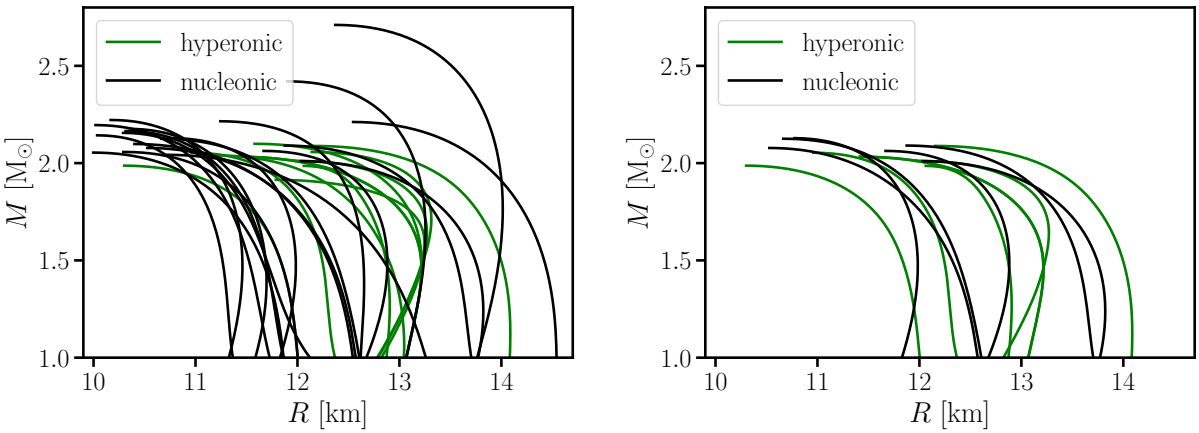

Figure 5.1.: (a): Mass-radius relations for all EoSs from the nucleonic sample (Sect. 3.2) in black and the hyperonic sample (Sect. 3.3) in green. Figure adapted from Ref. [360] (b): Same as (a) but for a selection of models from both samples with similar curves.

We see that based on the MR curves alone, it is very difficult to distinguish both samples. In general, hyperonic EoSs tend to produce relatively large radii at lower masses and also have smaller maximum masses, while some nucleonic models allow for considerably larger masses. Hence, there is a region of the MR diagram not populated by current hyperonic models. On the other hand,

several nucleonic models with very similar features as the EoSs in our hyperonic sample exist. This becomes even clearer from Fig. 5.1(b), where we show a selection of similar EoSs from both samples. Namely, here we plot the nucleonic models DD2F, DSH LR, FSU2R, GS2, SFHx and TMA and the hyperonic EoSs DD2Y, DNS, FSU2H*, QMA, R(DD2YDelta) 1.2-1.1, R(DD2YDelta) 1.2-1.3 and SFHoY.

From our observations, we conclude that even with very precise mass-radius measurements of NSs at several different masses, it will be not straightforward to tell if hyperons are present in some or all NSs. As no direct information on the matter composition can be inferred from observing stellar parameters, additional features are highly desirable to help solving the hyperon puzzle.

5.2. Hyperonic and nucleonic EoSs at finite temperatures

A possible approach to tell nucleonic and hyperonic EoSs apart may come from their different behavior at finite temperatures. Similarly to the hybrid EoSs containing deconfined quark matter discussed in Chapter 4, the onset density for the appearance of hyperons is temperature-dependent with hyperons appearing at lower densities for higher temperatures. This reduces the thermal pressure. In Fig. 5.2, we plot the effective ideal-gas index $\Gamma_{\rm th}$ (Eq. (2.28)) as a function of density for the hyperonic models FSU2H* and DD2Y (dashed lines) and the nucleonic models FSU2R and DD2 at temperatures of 20 MeV (Fig. 5.2(a)) and 30 MeV (Fig. 5.2(b)). At each density, Y_e corresponds to the composition of cold matter in neutrinoless beta-equilibrium.

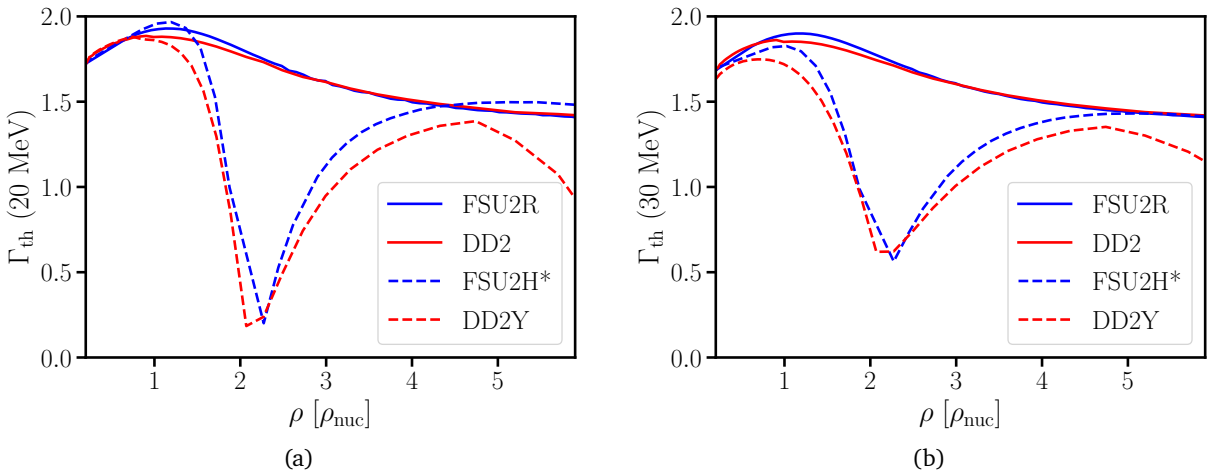

Figure 5.2.: (a): Effective ideal-gas index as defined by Eq. (2.28) of two nucleonic and two hyperonic EoSs as a function of density for a fixed temperature of 20 MeV. At each density, Y_e corresponds to the respective value of the cold EoS in neutrinoless beta-equilibrium composition. (b): Same as (a) but at a temperature of 30 MeV.

We see that at both temperatures, $\Gamma_{\rm th}$ increases at lower densities for all models reaching a maximum of roughly $\Gamma_{\rm th} \approx 1.8 - 1.9$ at around $\rho = 1.5 \times \rho_{\rm nuc}$. For the nucleonic EoSs this is followed by a gradual decrease towards $\Gamma_{\rm th} \approx 1.5$ at $\rho = 6 \times \rho_{\rm nuc}$. For the hyperonic models on the other hand, the local maximum in $\Gamma_{\rm th}$ is followed by a steep drop associated with the appearance of hyperons and a local minimum at around $\rho = 2 \times \rho_{\rm nuc}$. Hence, the hyperonic EoS are softer than the nucleonic models at finite temperatures. Here, $\Gamma_{\rm th}$ is even below 1 meaning that the pressure

is smaller at finite temperatures than at zero temperature. This is similar to our observations when discussing deconfined quark models (compare Fig. 4.5) albeit the effect is not as pronounced as for the hybrid EoSs discussed in Chapter 4. At higher densities, $\Gamma_{\rm th}$ rises again reaching similar values as the nucleonic models for densities around $\rho = 5 \times \rho_{\rm nuc}$. We also see that the drop in $\Gamma_{\rm th}$ sets in at lower densities at $T = 30$ MeV than at $T = 20$ MeV, but is also less pronounced.

Motivated by the observed behavior of $\Gamma_{\rm th}$, we investigate how this softening of hyperonic EoSs compared to nucleonic models impacts observables of NS mergers as temperatures of several tens of MeV can be reached in these systems. For this, we perform binary neutron star (BNS) merger simulations with every EoS from the nucleonic and the hyperonic sample using the fully temperature- and $Y_{\rm e}$-dependent tables. Additionally, we perform simulations restricted to the cold EoS slice in beta-equilibrium composition and the ideal-gas scheme (see Sect. 2.2) with $\Gamma_{\rm th} = 1.75$. We will refer to the simulations using the full EoS table as "3D" simulations and simulations using the barotropic slice with the ideal-gas scheme as "$\Gamma_{\rm th}$" simulations. In most cases, we consider symmetric binaries at total system masses of $M_{\rm tot} = 2.8\ M_\odot$. We perform additional simulations with both thermal schemes for the hyperonic models DD2Y and FSU2H* and the nucleonic EoSs DD2 and FSU2R with a total binary mass of $2.8\ M_\odot$ and a mass ratio of $q = 0.8$ to also test asymmetric systems. We apply the additional radial velocity after the initial relaxation as described in App. A to reduce the eccentricity during the inspiral in all simulations.

As noted in Chapter 4, assuming a constant $\Gamma_{\rm th}$ at all densities is insensitive to changes in the EoS at finite temperatures. It is apparent from Fig. 5.2 that using the ideal-gas approach with constant $\Gamma_{\rm th} = 1.75$ will overestimate the thermal pressure for hyperonic EoSs. This should result in lower gravitational-wave frequencies compared to a consistent, microphysical inclusion of finite-temperature effects. On the other hand, the ideal-gas approach as been shown to reproduce GW frequencies from nucleonic EoSs very well. Differences seen between employing the two approaches for capturing thermal effects in hyperonic EoSs can therefore be linked to the different thermal behavior compared to nucleonic EoS. Our goal is to quantify the strength of this effect using a representative sample of hyperonic models. In addition, we want to verify that the ideal-gas approach with $\Gamma_{\rm th} = 1.75$ remains a good approximation for nucleonic EoSs by testing it using our entire nucleonic sample.

Our approach can also be understood in the following way: Since the ideal-gas approach with $\Gamma_{\rm th} = 1.75$ mimics the thermal behavior of a nucleonic model, equipping a cold, hyperonic EoS with this scheme assumes that this cold EoS was actually produced by purely nucleonic matter. This is motivated by our earlier observation that cold hyperonic EoS may not have any features clearly distinguishing them from nucleonic models. By performing two sets of simulations with and effectively without the thermal influence of hyperons, we investigate how much the different thermal behavior of hyperons impacts neutron star merger observables and if hyperons can be potentially be identified in future postmerger GW observations.

5.3. Simulation results

To demonstrate the different thermal behaviors of hyperonic EoSs compared to nucleonic EoSs in 3D simulations, we calculate an average thermal index $\Gamma_{\rm th}^{\rm av}$ for all systems. For this, we invert Eq. (2.28) and determine the effective $\Gamma_{{\rm th},i}$ for each fluid element i. We then average this quantity over all SPH particles $\Gamma_{\rm th}^{\rm av} = \sum m_i \Gamma_{{\rm th},i} / \sum m_i$, where we set $\Gamma_{{\rm th},i} = 1$ for particles at the lowest tabulated temperature (typically 0.1 MeV). In Fig. 5.3(a), we show $\Gamma_{\rm th}^{\rm av}$ from simulations with symmetric binaries as a function of time for all EoS in the hyperonic set in different colors. Dashed lines mark results from hyperonic EoS also containing Δ-Baryons. Additionally, we show $\Gamma_{\rm th}^{\rm av}$ of two

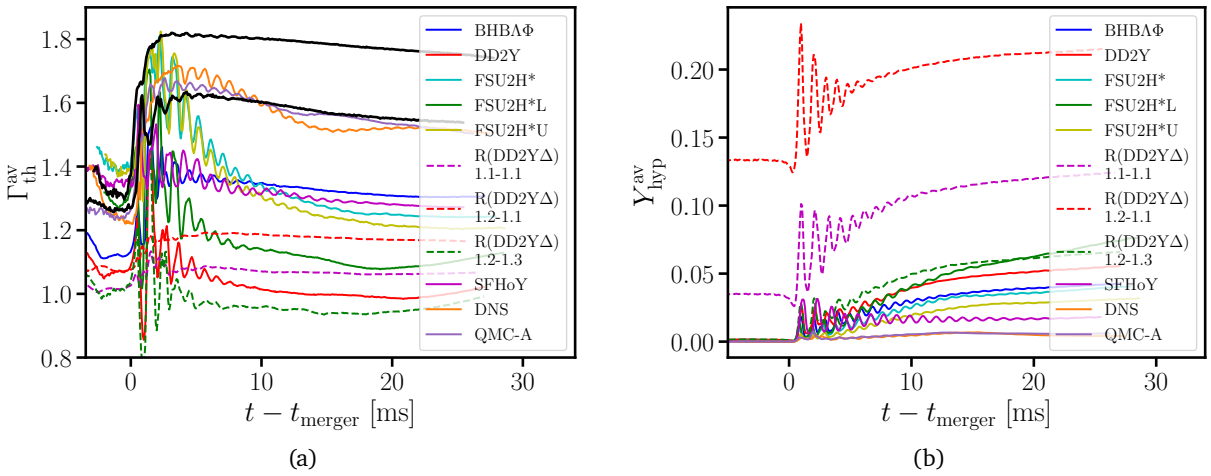

Figure 5.3.: (a): Time evolution of the mass-averaged ideal-gas index $\Gamma_{\rm th}^{\rm av}$ in $1.4 - 1.4\ M_\odot$ merger simulations with the hyperonic EoS sample. Different EoSs are displayed with different colors, the dashed lines mark models also considering Δ-baryons. For comparison the two black lines show the nucleonic models FSU2R and SFHo. (b): Time evolution of the mass-averaged hyperon fraction $Y_{\rm hyp}^{\rm av}$ in $1.4 - 1.4\ M_\odot$ merger simulations for all EoSs in the hyperonic sample. Same coloring as in (a). In both panels $t = 0$ corresponds to the time of merging.

simulations employing the nucleonic EoSs FSU2R and SFHo with black lines for comparison. Here, FSU2R leads to larger $\Gamma_{\rm th}^{\rm av}$ than SFHo.

The first observation we make is that values of $\Gamma_{\rm th}^{\rm av}$ are already larger than 1 during the late inspiral. This is mainly caused by small numeric heating meaning that in parts of the system temperatures are already slightly (up to a few MeV) above the lowest temperatures in the EoS tables prior to merging.

After the merger, we see that $\Gamma_{\rm th}^{\rm av}$ increases for all EoSs as more matter in the system is heated up. This is followed by an oscillatory behavior likely linked to the radial modes of the remnant and a general decrease. While we find that the general trend of $\Gamma_{\rm th}^{\rm av}$ is similar for all EoS, the values are quite different. A few milliseconds after merger most hyperonic EoS have $\Gamma_{\rm th}^{\rm av}$ between 1.0 and 1.4. The two nucleonic models on the other hand have values around 1.8 and 1.6, respectively, which are higher than most hyperonic EoSs. An exception are DNS and QMC-A. These models have relatively high onset densities at $T = 0$, which are not reached in our simulations. We find average thermal indices of around 1.6 for both EoSs, which are similar to results from our nucleonic sample. We also note that the three R(DD2YDelta) EoS have $\Gamma_{\rm th}^{\rm av}$ values on the lower side of our sample, but still within the range of models not including Δ baryons.

From the EoS tables, we also infer the hyperon fraction $Y_{{\rm hyp},i}^{\rm av}$ for each fluid element and calculate a mass-averaged hyperon fraction of the remnant $Y_{\rm hyp}^{\rm av}$ analogously to $\Gamma_{\rm th}^{\rm av}$. In Fig. 5.3(b), we show the time evolution of $Y_{\rm hyp}^{\rm av}$ for every hyperonic 3D simulation with symmetric binaries using the same colors as in Fig. 5.3(a). We see that during the inspiral, most systems do not contain hyperons as the densities and temperatures in the systems are too low. The only exception are the R(DD2YDelta)1.1-1.1 and R(DD2YDelta)1.2-1.1 EoSs, where substantial amounts of hyperons are present prior to the merger. At the collision, we find that $Y_{\rm hyp}^{\rm av}$ increases in all systems followed by

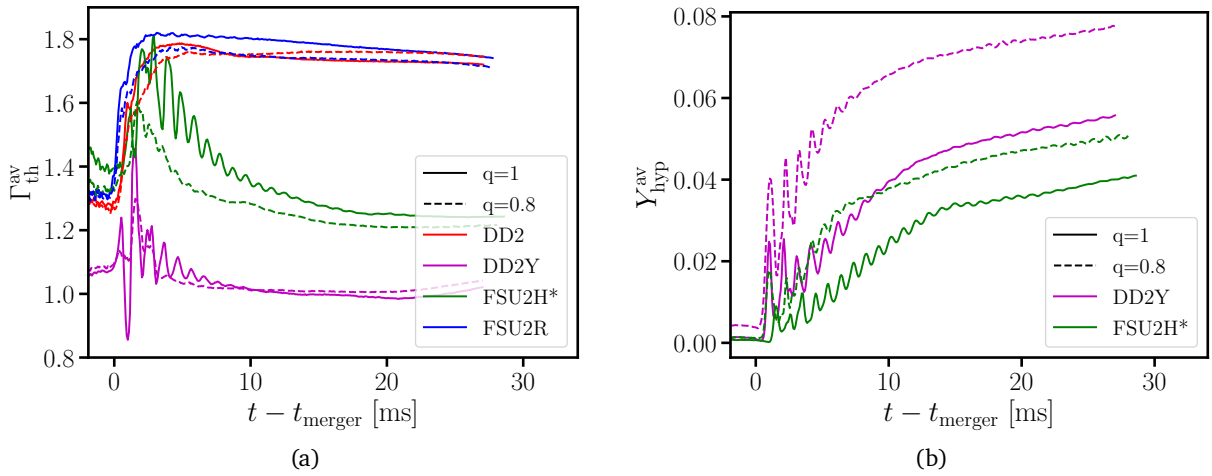

Figure 5.4.: (a): Time evolution of the mass-averaged ideal-gas index $\Gamma_{\rm th}^{\rm av}$ for two hyperonic and two nucleonic EoSs in merger simulations with total system masses of $2.8\,M_\odot$. Solid lines show results from symmetric binaries and dashed lines depict results from systems with a mass ratio of $q = 0.8$. (b): Time evolution of the mass-averaged hyperon fraction $Y_{\rm hyp}^{\rm av}$ for the simulations with hyperonic EoSs shown in (a). In both panels $t = 0$ corresponds to the time of merging.

an oscillatory behavior with an overall increasing trend. We also observe that all EoS lead to at least some amount of hyperons present in the system. This includes DNS and QMC-A, despite the maximum densities being lower than the onset density of hyperons at $T = 0$ for these two models. This is caused by thermal effects lowering the threshold for hyperon production.

In Fig. 5.4(a), we compare the evolution of $\Gamma_{\rm th}^{\rm av}$ in simulations of asymmetric systems with the results from the same EoS in symmetric binaries. We find that generally $\Gamma_{\rm th}^{\rm av}$ shows a very similar behavior for $q = 1$ and $q = 0.8$. For the nucleonic DD2 and the hyperonic DD2Y models, $\Gamma_{\rm th}^{\rm av}$ is almost identical in both cases. For the nucleonic FSU2R and the hyperonic FSU2H* EoSs, $\Gamma_{\rm th}^{\rm av}$ is slightly decreased in the asymmetric system compared to the simulation with $q = 1$, the general trend is however still similar. We also compare the time evolution of $Y_{\rm hyp}^{\rm av}$ in the symmetric and the asymmetric systems for the DD2Y and the FSU2H* EoSs in Fig. 5.4(b). Here, we find a similar increasing trend after the merger in both cases, however the asymmetric systems always contain larger amounts of hyperons than systems with $q = 1$.

In a next step we directly compare simulations with the two different thermal treatments for a fixed EoS model. Fig. 5.5(a) shows the time evolution of the maximum rest-mass density $\rho_{\rm max}$ for the FSU2H* EoS employing the 3D table and the $\Gamma_{\rm th}$ approach.

We see that prior to the merger, the densities in both simulations are practically identical, which is understandable since the temperatures are low at this stage. After the merger, we find that the $\Gamma_{\rm th}$ simulation leads to lower densities in the first and the third local maximum of $\rho_{\rm max}$. Once the density oscillations have settled down, the two curves depart more clearly from each other with the 3D simulation producing larger remnant densities. This finding corresponds to our earlier observation that a constant $\Gamma_{\rm th} = 1.75$ overestimates the thermal pressure in the remnant, as for this EoS we observe $\Gamma_{\rm th}^{\rm av} < 1.75$.

We show the corresponding GW spectra of both simulations in Fig. 5.5(b). For the low frequency

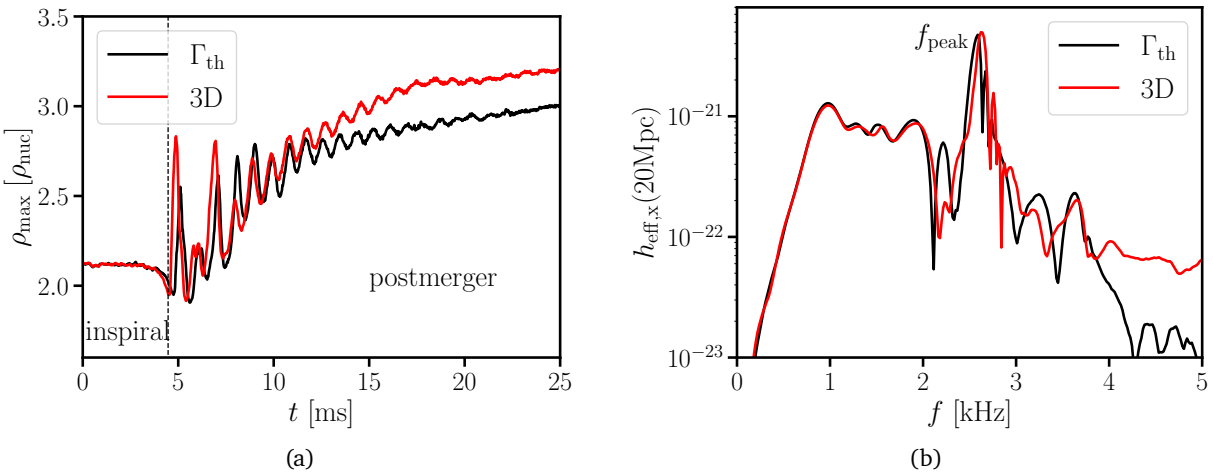

Figure 5.5.: (a): Evolution of the maximum rest-mass density for the merger of two $1.4\ M_\odot$ NSs using the hyperonic FSU2H* EoS with the full 3D EoS table (red) and the barotropic EoS slice employing the ideal-gas approach with $\Gamma_{\rm th} = 1.75$ (black) to include finite temperature effects. (b): Gravitational-wave spectrum of the cross polarization at a distance of 20 Mpc along the polar axis from the same simulations as in (a).

part from the inspiral, where the system is still at low temperatures, we find that the spectra are matching almost exactly. In the postmerger range, we see that the 3D simulation leads to slightly higher frequencies, namely for $f_{\rm peak}$ we find a difference of about 40 Hz. This corresponds to our finding that including thermal effects of hyperons consistently leads to more compact merger remnants.

We now perform the same comparison for the purely nucleonic FSU2R model. From Fig. 5.3(a), we see that this EoS has $\Gamma_{\rm th}^{\rm av}$ close to 1.75. Hence, we expect a better agreement than for FSU2H*. The evolution of the maximum densities for the 3D and the $\Gamma_{\rm th}$ simulation are plotted in Fig. 5.6(a). As anticipated, we generally see very good agreement of the two curves. The only major difference is a second larger density spike shortly after the merger in the $\Gamma_{\rm th}$ simulation, which is absent in the 3D simulation. Still, for this model the ideal-gas approach with $\Gamma_{\rm th} = 1.75$ is a very good approximation for the thermal EoS part. The corresponding GW spectra are shown in Fig. 5.6(b). Again, we see good agreement between the two simulations. In particular, the $f_{\rm peak}$ coincide within a few Hz.

We summarize simulation results for all models in the hyperonic and the nucleonic EoS sample in Table 5.1 and Table 5.2, respectively. We present $f_{\rm peak}$ with both approaches for the thermal EoSs as well as the maximum rest-mass density within the first 5 ms after the merger $\rho^{\rm max}$. For the hyperonic sample, we also tabulate the maximum density at the beginning of the simulation $\rho_{\rm init}^{\rm max}$ and underline values larger than the respective onset density of hyperons (see Table. 3.2), i.e. systems containing hyperons before the merger. We also present the mass- and time-averaged hyperon fraction $\bar{Y}_{\rm hyp}$, which we calculate by averaging $Y_{\rm hyp}^{\rm av}$ over 5 ms starting 2.5 ms after the merger. Additionally, we calculate a mass- and time-averaged thermal index of the remnant $\bar{\Gamma}_{\rm th}$ for both samples, which we obtain from $\Gamma_{\rm th}^{\rm av}$ analogous to $\bar{Y}_{\rm hyp}$.

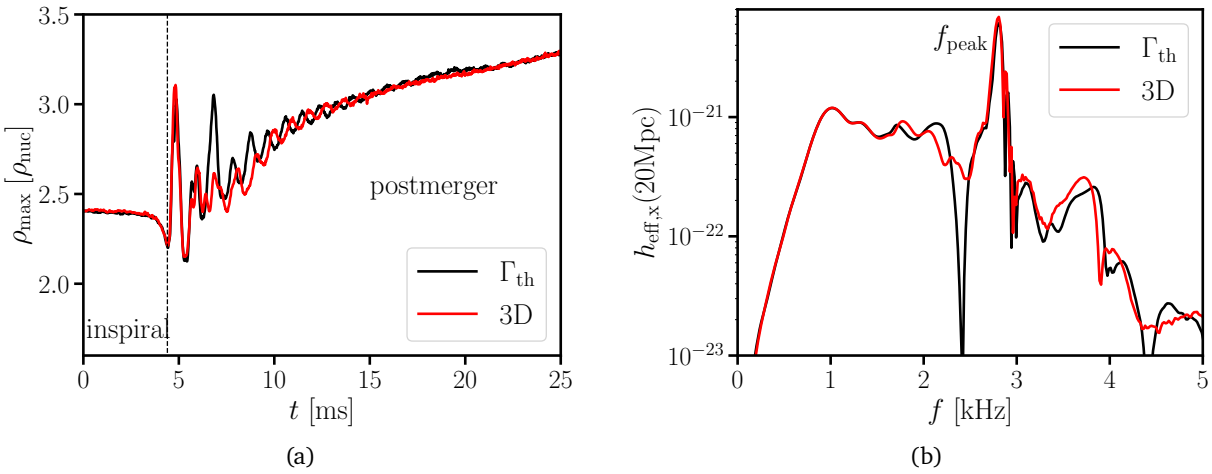

Figure 5.6.: (a): Evolution of the maximum rest-mass density for the merger of two $1.4\ M_\odot$ NSs using the nucleonic FSU2R EoS with the full 3D EoS table (red) and the barotropic EoS slice employing the ideal-gas approach with $\Gamma_{\rm th} = 1.75$ (black) to include finite temperature effects. (b): Gravitational-wave spectrum of the cross polarization at a distance of 20 Mpc along the polar axis from the same simulations as in (a).

5.3.1. Systematic investigation of thermal effects

To systematically compare $f_{\rm peak}$ between our two sets of simulations using the full 3D EoS table and the barotropic EoS with the ideal-gas approach for both EoS samples, we define the quantity $\Delta f \equiv f^{\rm 3D}_{\rm peak} - f^{\rm 1.75}_{\rm peak}$, i.e. the difference in $f_{\rm peak}$ when using our two approaches for the thermal effects. Hence, Δf quantifies how well the finite-temperature behavior of a 3D EoS table is modeled in a merger simulation using the ideal-gas scheme with $\Gamma_{\rm th} = 1.75$. This can also be understood as measuring how much a given model deviates from the prediction of an idealized "nucleonic" thermal behavior. Note that Δf itself is not an observable quantity, but has to be inferred with the help of numerical simulations.

We plot Δf as a function of $f^{\rm 3D}_{\rm peak}$ for all or hyperonic (colored) and nucleonic (black) models in Fig. 5.7(a). While the absolute values of $f_{\rm peak}$ vary by about 1kHz between all considered EoSs, we see that results from purely nucleonic EoSs scatter around $\Delta f = 0$ with a maximum difference of around 50 Hz. This confirms that the ideal-gas approach with $\Gamma_{\rm th} = 1.75$ is a good choice for nucleonic matter (but see discussion in Sec. 5.4). Note that this EoS sample also contains recently published models for which the ideal-gas approach has not been tested previously.

For hyperonic models, we find that Δf lies roughly between 40 Hz and 140 Hz for most models meaning that the ideal-gas approach mimicking a nucleonic thermal behavior consistently slightly underestimates $f_{\rm peak}$ compared to the simulations employing the full 3D table. Such a shift is small, but may be possible to infer with future GW detectors (see discussion below). The only exception are DNS and QMC-A, which have negative Δf, i.e. the ideal-gas approach somewhat overestimates $f_{\rm peak}$, and generally agree well with results from the nucleonic sample.

The coloring of the hyperonic results indicates the ratio between $\rho^{\rm max}$ and $\rho_{\rm onset}$. Note that the coloring looks very similar if we directly indicate the hyperon content in the remnant or the mass-averaged thermal ideal-gas index as these quantities are correlated with $\rho^{\rm max}/\rho_{\rm onset}$ (see Fig. 5.8(b)).

Table 5.1.: Simulation results for the sample of EoSs including hyperonic degrees of freedom. Second and third column report the dominant postmerger GW frequency $f_{\rm peak}$ from simulations using either the full temperature-dependent EoS table or the barotropic EoS table together with the ideal-gas approximation for thermal pressure and $\Gamma_{\rm th} = 1.75$. $\bar{\Gamma}_{\rm th}$ and $\bar{Y}_{\rm hyp}$ refer to the mass- and time-averaged thermal ideal-gas index and hyperon fraction of the remnant, respectively. $\rho^{\rm max}_{\rm init}$ is the maximum rest-mass density at the beginning of the simulation and $\rho^{\rm max}$ the maximum rest-mass density within the first 5 ms after merger. Underlined values of $\rho^{\rm max}_{\rm init}$ highlight systems with hyperons present prior to merging. Table adapted from Ref. [360].

EoS	$f^{\rm 3D}_{\rm peak}$ [kHz]	$f^{1.75}_{\rm peak}$ [kHz]	$\bar{\Gamma}_{\rm th}$	$\bar{Y}_{\rm hyp}$	$\rho^{\rm max}_{\rm init}$ [$\rho_{\rm nuc}$]	$\rho^{\rm max}$ [$\rho_{\rm nuc}$]
BHB$\Lambda\phi$	2.76	2.68	1.37	0.018	<u>2.22</u>	2.97
DD2Y	2.82	2.73	1.08	0.022	<u>2.26</u>	3.01
DD2Y(q=0.8)	2.76	2.63	1.04	0.050	<u>2.56</u>	3.76
DNS	2.51	2.54	1.69	0.003	2.07	2.48
FSU2H*	2.63	2.59	1.52	0.012	2.07	2.82
FSU2H*(q=0.8)	2.76	2.69	1.37	0.025	2.26	3.27
FSU2H*L	2.68	2.62	1.24	0.018	2.03	2.86
FSU2H*U	2.62	2.56	1.51	0.008	2.03	2.63
QMC-A	2.91	2.98	1.65	0.003	2.48	3.42
R(DD2YΔ) 1.1-1.1	3.03	2.93	1.08	0.083	<u>2.60</u>	3.58
R(DD2YΔ) 1.2-1.1	3.26	3.14	1.18	0.185	<u>2.90</u>	4.37
R(DD2YΔ) 1.2-1.3	2.82	2.72	0.99	0.029	<u>2.26</u>	3.16
SFHoY	3.60	3.46	1.38	0.015	3.20	5.80

From the coloring, we infer that the onset densities of hyperons at $T = 0$ are not reached in our simulations for DNS and QMC-A, while they are for all other hyperonic EoSs. This is in agreement with our findings from Fig. 5.3(a), where we noted that these two models have $\Gamma^{\rm av}_{\rm th}$ more similar to EoSs from the nucleonic sample and larger than in the hyperonic sample. It is hence understandable that Δf of these two EoS deviate from all other hyperonic models and are more comparable to results from nucleonic EoSs. Note however, that despite $\rho^{\rm max}$ being smaller than $\rho_{\rm onset}$ tiny amounts of hyperons are still present in these systems after merger, as can be seen from Fig. 5.3(b). This is due to finite temperature effects lowering the onset density of hyperon formation.

In Fig. 5.7(b), we show the shift in $f_{\rm peak}$ as a function of the mass- and time-averaged thermal index of the remnant $\bar{\Gamma}_{\rm th}$ for all employed EoS models. We see that the hadronic EoSs have $\bar{\Gamma}_{\rm th}$ in the range of roughly 1.5-1.8 with a cluster around 1.75 and a few results at lower values. This demonstrates that $\Gamma_{\rm th} = 1.75$ is a good choice to model the thermal behavior of nucleonic EoSs. For these models, we do not observe a clear correlation between the shift in $f_{\rm peak}$ and $\bar{\Gamma}_{\rm th}$.

For the hyperonic EoSs on the other hand, we see that $\bar{\Gamma}_{\rm th}$ is smaller and generally lies in the range of 1.0-1.5 for models with $\rho^{\rm max} > \rho_{\rm onset}$ (compare Fig. 5.3(a)). Here, we observe that models with smaller $\bar{\Gamma}_{\rm th}$, i.e. lower thermal pressure, also tend to produce larger frequency shifts. However, this correlation is not very strong. In particular, we find that the SFHoY EoS, which produces the

Table 5.2.: Simulation results for the sample of purely nucleonic EoSs. Second and third column report the dominant postmerger GW frequency $f_{\rm peak}$ from simulations using either the full temperature-dependent EoS table or the barotropic EoS table together with the ideal-gas approximation for thermal pressure with $\Gamma_{\rm th} = 1.75$. $\bar{\Gamma}_{\rm th}$ refers to the mass- and time-averaged thermal ideal-gas index of the remnant. $\rho^{\rm max}$ is the maximum rest-mass density within the first 5 ms after merger. Table adapted from Ref. [360].

EoS	$f_{\rm peak}^{\rm 3D}$ [kHz]	$f_{\rm peak}^{1.75}$ [kHz]	$\bar{\Gamma}_{\rm th}$	$\rho^{\rm max}$ [$\rho_{\rm nuc}$]
APR	3.51	3.46	1.74	5.31
DD2	2.64	2.68	1.78	2.67
DD2(q=0.8)	2.68	2.69	1.74	2.75
DD2F	3.30	3.30	1.66	4.22
DSH F	3.44	3.40	1.77	4.82
DSH LM	2.93	2.91	1.79	3.20
DSH LSL	3.51	3.46	1.52	5.19
DSH LR	3.16	3.18	1.72	4.06
DSH SSL	3.31	3.33	1.76	4.55
DSH SR	3.62	3.60	1.72	6.25
FSU2R	2.80	2.81	1.81	3.12
FSU2R(q=0.8)	2.69	2.70	1.76	3.43
FTNS	3.34	3.40	1.73	4.74
GS2	2.73	2.70	1.76	2.75
LPB	3.23	3.23	1.68	3.80
LS220	3.09	3.06	1.54	3.76
LS375	2.44	2.44	1.63	2.22
SFHo	3.43	3.45	1.62	5.34
SFHx	3.16	3.18	1.82	4.10
SLy4	3.51	3.50	1.78	5.38
TM1	2.38	2.40	1.82	2.07
TMA	2.58	2.57	1.74	2.48

largest shift (140 Hz), has a moderate $\bar{\Gamma}_{\rm th} = 1.38$. We remark that the results from asymmetric systems agree well with the findings from symmetric binaries.

We further investigate the behavior of Δf for hyperonic models in Fig. 5.8. Here, we plot Δf as a function of the ratio $\rho^{\rm max}/\rho_{\rm onset}$ (Fig. 5.8(a)) and the mass and time-averaged hyperon fraction $\bar{Y}_{\rm hyp}$ of the system (Fig. 5.8(b)). Both values are taken from the simulations with the 3D EoS tables.

We see that at low ratios $\rho^{\rm max}/\rho_{\rm onset}$ (up to about 1.5) Δf rises very rapidly reaching values of just above 100 Hz. For higher densities, this effect saturates and we find no further correlation of Δf with $\rho^{\rm max}/\rho_{\rm onset}$. Again, we find similar results for asymmetric systems. The dependence of Δf on $\bar{Y}_{\rm hyp}$ looks analogous. For low hyperon fractions in the system, the frequency shift between the two thermal methods increases strongly but this effect quickly levels out at around 100 Hz. On the one hand, this implies that a small amount of hyperons in the merger remnant could already be sufficient to leave a noticeable imprint on the GW signal. The densities in the system do not have to exceed the onset density of hyperons by much to allow for an inference of hyperons. Considering that Refs. [52, 53] demonstrated a tight correlation of $f_{\rm peak}$ with the maximum densities reached

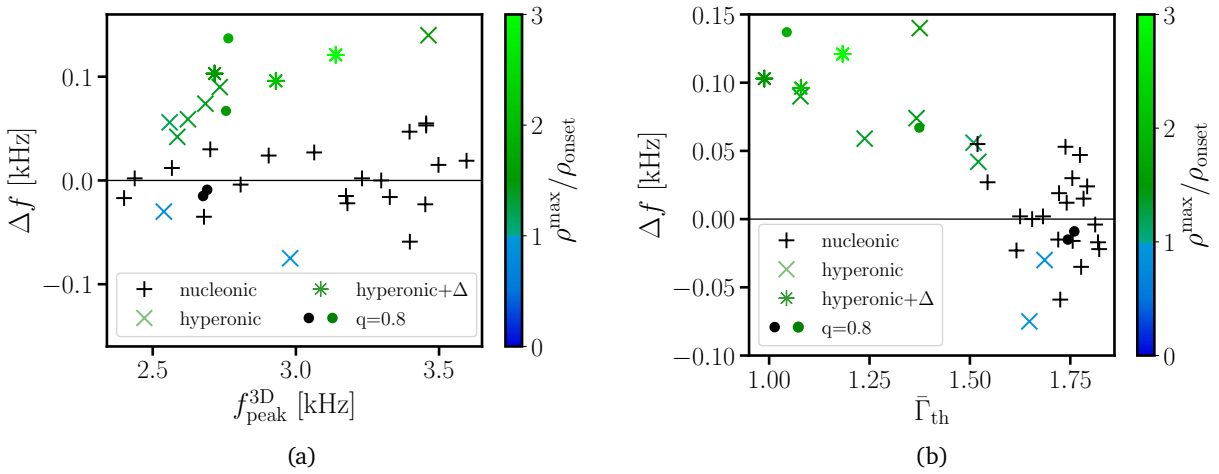

Figure 5.7.: (a): Difference $\Delta f = f^{\mathrm{3D}}_{\mathrm{peak}} - f^{1.75}_{\mathrm{peak}}$ between dominant postmerger GW frequency of simulations with fully temperature-dependent EoSs and calculations with same EoS models restricted to zero temperature and supplemented with an ideal-gas treatment of thermal effects, which mimics the behavior of purely nucleonic EoSs by choosing a thermal ideal-gas index of $\Gamma_{\mathrm{th}} = 1.75$. Shown as function of $f^{\mathrm{3D}}_{\mathrm{peak}}$. Black symbols depict purely nucleonic models. Crosses display hyperonic models, where the coloring indicates the ratio between the maximum rest-mass density in the postmerger remnant and the onset rest-mass density of hyperon production at zero temperature. Asterisks refer to models which additionally include Δ-baryons and circles to results from asymmetric binaries. (b): Δf as function of mass- and time-averaged thermal index of the merger remnant in simulations employing the temperature-dependent EoSs. Same symbols and color scheme as in (a). Both figures adapted from Ref. [360].

in merger remnants for hadronic EoSs, this could help constraining the onset density of hyperons. On the other hand, our finding seems to suggest that this effect may not be significantly larger when more hyperons are present in the system, e.g. at higher masses. Frequency shifts of only about 100 Hz in f_{peak} are small compared to the variation of f_{peak} with the EoS and the FWHM of the peaks. It will hence be very challenging to infer the presence of hyperons from the GW signal. However, it may still be potentially sizable enough for a detection. Recent GW injection studies (as e.g. [41, 422, 423, 424, 425, 426, 427, 54, 428, 429]) show that such a precision is in principle achievable making the impact of hyperons detectable. This would also require a sufficiently accurate determination of the cold EoS. Employing the empirical relation of Ref. [336] which connects f_{peak} to the radius of cold, non-rotating NSs, we infer that a frequency shift of 100 Hz corresponds to a change in radius of about 250 m. This provides a coarse estimate on the required precision needed for the cold EoS.

Additionally, reliable simulation tools are necessary to predict a reference value of $f^{1.75}_{\mathrm{peak}}$ a measured f_{peak} can then be compared to. Both prerequisites are not given currently, but may be achievable in the future despite clearly posing great challenges.

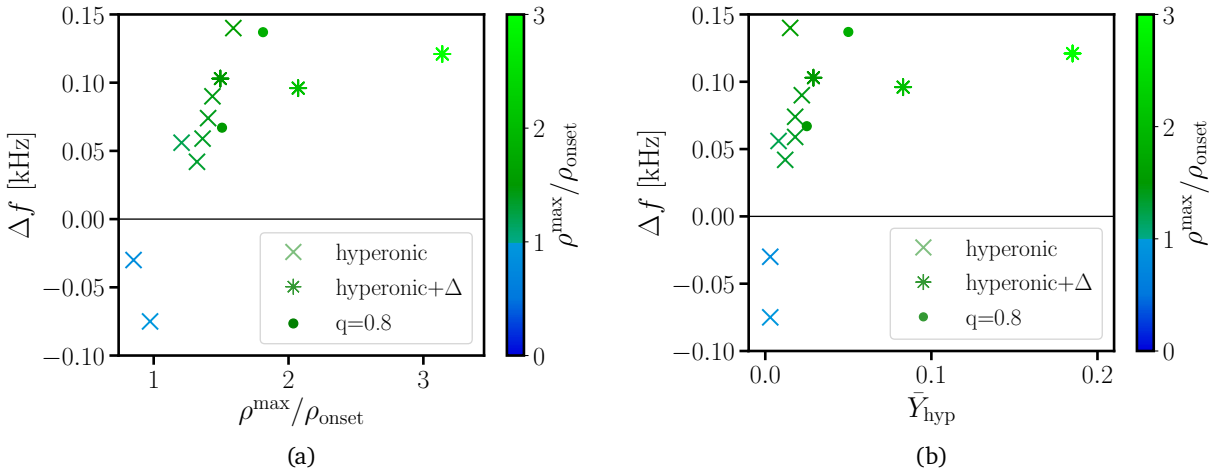

Figure 5.8.: (a): Difference $\Delta f = f_{\text{peak}}^{\text{3D}} - f_{\text{peak}}^{1.75}$ between the dominant postmerger GW frequency of simulations with the fully temperature-dependent EoSs and calculations with same EoS models restricted to zero temperature and supplemented with an ideal-gas treatment of thermal effects with $\Gamma_{\text{th}} = 1.75$ as a function of the ratio between the maximum density shortly after merging and the onset density of hyperons at $T = 0$ for the hyperonic EoS sample. Asterisks refer to models which additionally include Δ-baryons and circles display results from asymmetric binaries. (b): Δf as a function of the mass- and time-averaged hyperon fraction $\bar{Y}_{\text{hyp}}$.

5.3.2. Empirical relation

To further investigate the possibility of identifying hyperons, we consider relations between two observable quantities, namely f_{peak} and the tidal deformability Λ_{M} of a NS with mass M (see Sect. 3.1 for the definition of Λ). As mentioned earlier, Λ is a quantity directly characterizing the cold EoS that can be inferred from the GW signal emitted in the inspiral phase. Note that due to higher detector sensitivity at lower frequencies, the combined tidal deformability $\tilde{\Lambda}$ of the system will be measured with higher precision than f_{peak} in future detections.

As we mainly consider $1.4 - 1.4\ M_{\odot}$ binaries, relating f_{peak} to the tidal deformability $\Lambda_{1.4}$ would be a natural choice. However, as pointed out by Ref. [430], when relating f_{peak} and Λ_{M}, the mass M at can in principle be chosen freely and the choice will affect the accuracy of the relation. Similar to Ref. [430], we relate $f_{\text{peak}} - \Lambda_{\text{M}}$ at several different M and compare the scatter of the different relations. For this, we fit a second-order polynomial to $f_{\text{peak}}^{\text{3D}}$ of the nucleonic sample from the symmetric binaries with a least-squares fit. In Fig. 5.9, we show the mean and the maximum deviation of the data sample from the respective fit.

As expected, we see that the accuracy of the relation depends on M. The maximum deviation has a minimum of only 55 Hz at $M = 1.75\ M_{\odot}$ indicated by the dashed, vertical line. At this mass, the average scatter of the relation is as low as 28 Hz. Hence, we compare results from the hyperonic sample to the $f_{\text{peal}} - \Lambda_{1.75}$ relation. Note that a variation of 55 Hz is comparable to the scatter we find for Δf using nucleonic EoSs.

In Fig. 5.10, we plot $f_{\text{peak}}^{\text{3D}}$ as a function of $\Lambda_{1.75}$ for all EoS in both samples. The black line is the quadratic fit to the results from nucleonic models and the gray-shaded area visualizes the maximum scatter of 55 Hz. We explicitly show the deviations of all $f_{\text{peak}}^{\text{3D}}$ from this relation in Fig. 5.10(b)

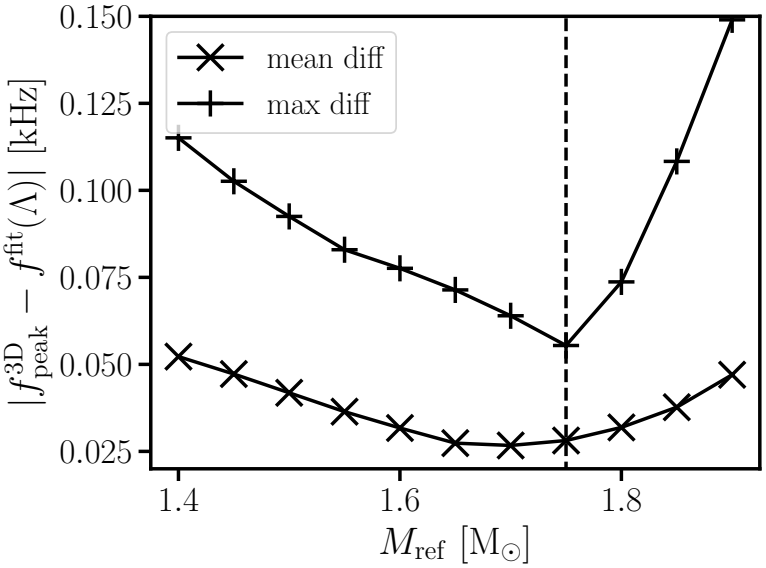

Figure 5.9.: Mean and maximum deviation of our data from symmetric binaries for purely nucleonic EoSs from quadratic $f_{\rm peak} - \Lambda_M$ least-squares fits for different reference masses M at which Λ is evaluated. The dashed vertical line indicates the minimum of the maximum deviation at $M = 1.75$. Figure adapted from Ref. [360].

as a function of the mass- and time-averaged thermal index $\bar{\Gamma}_{\rm th}$ of the respective remnant. The horizontal, dashed lines mark the maximum scatter of 55 Hz we infer for the nucleonic results.

We see that results from hyperonic models (colored symbols) are slightly increased and lie mostly above the maximum scatter of the results from nucleonic EoSs. This suggests that at least in principle the presence of hyperons could be deduced by an increased postmerger GW frequency compared to $\Lambda_{1.75}$ which no nucleonic model can reach. As before, results from the DNS and QMC-A EoSs agree very well with the nucleonic sample due to the very low amount of hyperons present in these systems. For the two simulations employing nucleonic EoSs in asymmetric binaries, we find a somewhat larger scatter from the relation. This could imply that $f_{\rm peak} - \Lambda$ relations may simply be not as tight in the case of asymmetric binaries or that a different reference mass should be used for these systems. This finding should be further investigated in future work.

We remark that in this relation some models containing fairly large amounts of hyperons and the three EoSs containing Δ-baryons do not stand out clearly from models with a smaller hyperon fraction. Especially, we see that in contrast to Fig. 5.7(b) there is no apparent correlation of the deviation hyperonic models show from the $f_{\rm peal} - \Lambda_{1.75}$ relation and $\bar{\Gamma}_{\rm th}$. From Fig. 5.7(a), we see that these models do in fact result in a sizable frequency shift Δf caused by the softening induced by hyperons at finite temperatures. However, employing the ideal-gas approach with these models leads to frequencies on the lower edge of the gray band, as can be inferred from Fig. 5.7(a). Hence, the frequency shift only compensates this effect. The location of hyperonic models with respect to the fit in Fig. 5.10 is therefore not directly linked to the total amount of hyperons in the system. It is instead a superposition of the thermal effects of hyperons and the properties of the cold EoS not directly captured by $\Lambda_{1.75}$.

Generally, the frequency increase of $f_{\rm peak}$ with respect to the $f_{\rm peak}-\Lambda_{1.75}$ relation is small and only marginally larger than the intrinsic scatter of this relation. To improve the prospects of inferring

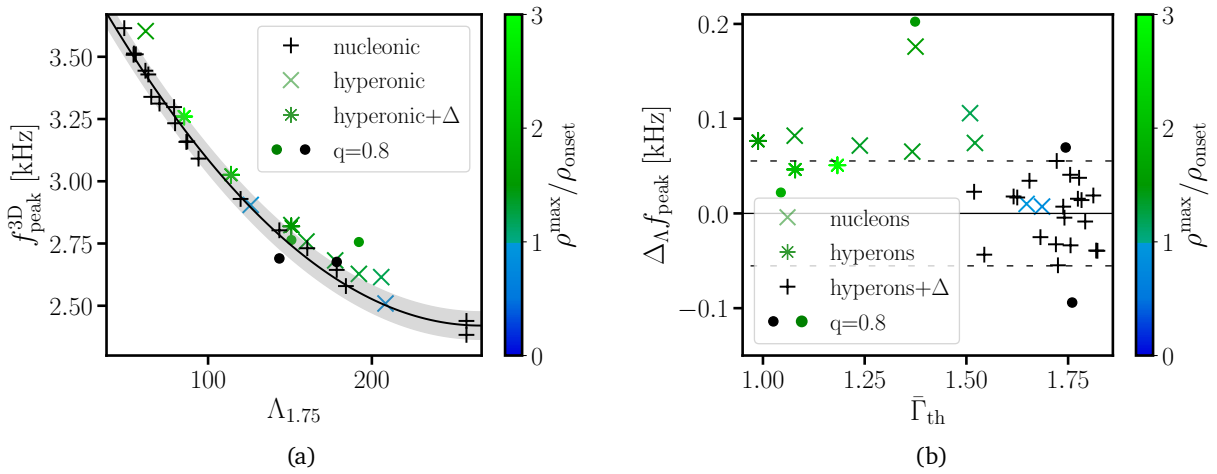

Figure 5.10.: (a): Dominant postmerger GW frequency of 2.8 $M_\odot$ mergers using the 3D EoS tables as function of tidal deformability of a 1.75 $M_\odot$ NS. Symbols and color scheme as in Fig. 5.7(a). Black curve shows least-squares fit to symmetric binaries with purely nucleonic models. Grey band indicates maximum residual of symmetric purely nucleonic models from the fit. (b): Difference between the dominant postmerger GW frequency of 2.8 $M_\odot$ mergers and the frequency given by the least-squares fit of $f_{\rm peak}(\Lambda_{1.75})$ for purely nucleonic models (see Fig. 5.10) as function of the mass- and time averaged thermal ideal-gas index of the remnant. Same symbols and color scheme as in Fig. 5.7(a). Dashed lines indicate maximum residual of the fit to purely nucleonic EoSs. Both figures adapted from Ref. [360].

the presence of hyperons, it is hence important to further explore such empirical relation and gain a better understanding of the scatter.

5.4. χEFT-inspired toy model

Recent calculations based on chiral effective field theory (χEFT) suggest that a drop in the thermal index with increasing density could also be present in purely nucleonic matter [431, 432]. In these state-of-the art nuclear matter calculations, the strong three body force within χEFT increases the effective nucleon mass reducing the thermal index (see Eq. (41) in [431]) and hence the pressure at finite temperatures. Current calculations with χEFT are however limited to densities below roughly $2 \times \rho_{\rm nuc}$ and temperatures smaller than 30 MeV [131]. The resulting EoS is hence not directly applicable in neutron star merger simulations and it is not clear, in which density and temperature range this effect is present. Additionally, exotic degrees of freedom such as hyperons are not included in the χEFT framework of Refs. [431, 432]. A drop in $\Gamma_{\rm th}$ as seen in these χEFT calculations could in principle mimic the effects we observed for hyperonic matter in this chapter. Especially, if this result turns out to be a generic feature within a larger density range, it may be difficult to disentangle our findings on hyperonic EoSs from properties of nucleonic matter. Therefore, we apply a toy model to explore how the additional appearance of hyperons would affect an EoS in which the nucleonic part already shows a drop in $\Gamma_{\rm th}$ as suggested by the χEFT calculations of [431, 432]. This model was developed by Hristijan Kochankovski during the collaborative work

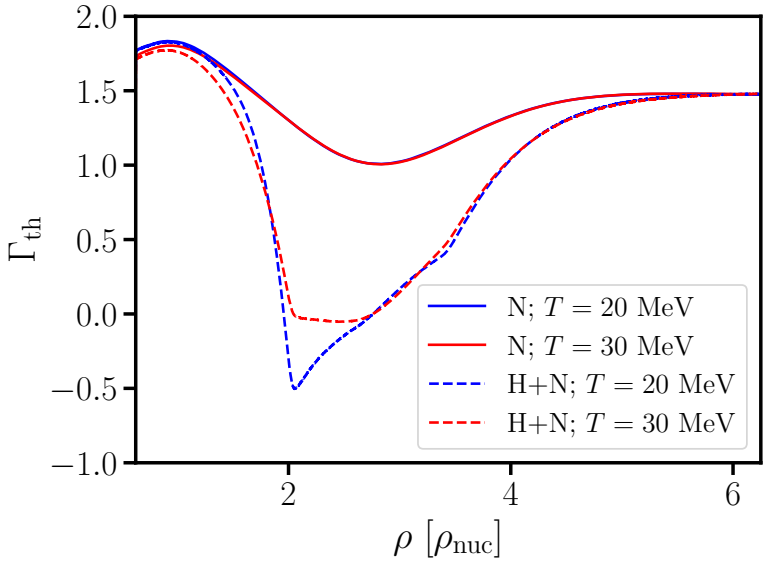

Figure 5.11.: The thermal index for nucleonic (solid lines) and hyperonic matter (dashed lines) at two different temperatures, $T = 20$ MeV (blue lines) and $T = 30$ MeV (red lines) for a toy model inspired by recent χEFT calculations. See text for details. The results shown in this plot were provided by Hristijan Kochankovski. Figure adapted from Ref. [360].

on this project.

We set up this toy model within the relativistic mean field framework with the DDME2 interaction [433]. Hyperons are included using the density-dependent couplings as defined in Ref. [434]. To achieve a drop in the thermal index, we modify the functional density dependence of the σ-meson coupling for the nucleons. This leads to minimum of their effective mass close to saturation density. The other meson couplings remain unchanged. It is important to note that the EoS we construct this way is incompatible with current constraints from the properties of nuclear matter and nuclei, heavy ion collisions at high energies and astrophysical constraints (see Sect.1.2.1). This approach should therefore be regarded as a toy model with the sole purpose of analyzing thermal effects when additionally adding hyperons to a nucleonic EoS already featuring a thermal index $\Gamma_{\rm th} < 4/3$. This is meant to resemble the results from the aforementioned χEFT calculations with the inclusion of hyperons.

In Fig. 5.11, we plot $\Gamma_{\rm th}$ of our toy model in beta-equilibrium composition as a function of density with and without including hyperons at temperatures of 20 MeV and 30 MeV. For purely nucleonic matter, we clearly see the anticipated decrease in $\Gamma_{\rm th}$ for densities larger than roughly 0.2 fm^{-3} reaching minimum values of around 1. In matter additionally containing hyperons, the drop in $\Gamma_{\rm th}$ is significantly larger even reaching minimum values below zero. This is also a more significant impact on $\Gamma_{\rm th}$ than in the microphysical hyperonic EoSs employed in our study (compare Fig. 5.2). As in these models, the additional softening of the thermal EoS can be attributed to the loss of degeneracy pressure as hyperons appear. Our toy model suggests that this effect could also be present if the nucleonic interactions already permit a decreasing $\Gamma_{\rm th}$. The findings from our study would in principle still hold in this case, as hyperonic models would still be distinguishable from nucleonic models through their different thermal behavior.

However, we remark a few caveats. As already discussed, our toy model is incompatible with current astrophysical observations and nuclear matter properties. The impact of a decreasing thermal index in nuclear matter on EoSs containing hyperons should hence be further investigated in the future with more realistic approaches. We also remark that in the relativistic mean field approach of our toy model, the effective masses of hyperons and nucleons are correlated as the coupling constants for both species are related by symmetry relations. This results in the same functional dependence of the effective masses for hyperons and nucleons, which is not necessarily the case in a more realistic model and may influence on the size of the additional drop of Γ_{th} caused by hyperons.

The further investigation of these caveats is beyond the scope of this work. Hence, we conclude at the moment that one can expect the main findings regarding the influence of hyperons on GW signals from BNS mergers to hold in a scenario suggested by current χEFT calculations where nucleonic matter permits a substantial drop in Γ_{th}. However, the issues we mentioned should be addressed in future work with more realistic models to further analyze the behavior of the thermal index with density in NS matter with and without hyperons.

6. Summary, discussion and outlook

In this thesis, we explore the finite-temperature behavior of matter phases containing hyperons or deconfined quarks in the context of neutron star (NS) mergers. For this, we perform general-relativistic hydrodynamics simulations with a comprehensive equation of state (EoS) sample featuring hyperonic degrees of freedom in Chapter 5 as well as hybrid models with a first-order phase transition to deconfined quark matter in Chapter 4. The main goal is to disentangle the impact of the finite-temperature EoS on the postmerger gravitational-wave (GW) signal from the influence coming from the cold EoS part. We highlight the differences caused by these more exotic phases of matter at finite temperatures by comparing our findings to results from different purely nucleonic EoSs.

6.1. Thermal effects in hybrid equations of state

First, we investigate thermal effects of deconfined quark matter in NS mergers for hybrid EoSs with a Maxwell-type behavior, i.e. EoSs with a hadronic and deconfined quark matter phase connected by a coexistence region with almost constant pressure. As the transition density to quark matter is expected to be temperature-dependent, we show with the microphysical DD2F-SF EoS sample that this can lead to a reduced pressure at finite temperatures compared to the pressure of cold matter. The reduction in pressure is caused by the "earlier" onset of quark deconfinement and the abrupt change of the EoS once the phase transition sets in. Hence, hybrid EoSs are more complex to model than purely hadronic models as not only a thermal component but also the phase boundaries have to be considered. A more thorough study of this effect is currently not straightforward due to the sparse number of hybrid EoS consistently including finite-temperature treatments.

Because of this limited availability, barotropic, hybrid EoS in combination with the approximate ideal-gas thermal scheme are still commonly used in astrophysical simulations. However, as we clearly show, this treatment cannot reproduce the decrease of the thermal pressure in hybrid models we observe in the DD2F-SF models. The reason is that this approach does not account for shifting phase boundaries at finite temperatures, which results in qualitatively different thermal EoS features.

We then present an extension of the ideal-gas approach to supplement a barotropic, hybrid EoS. This new effective phase transition scheme (eff PT) requires a quantitative description of the phase boundaries as a function of specific thermal energy density ϵ_{th} that needs to be provided. The main idea is then to interpolate the coexistence region using the boundaries of this phase and two different values of the ideal-gas index Γ_{th} for both phases of matter. In pure deconfined quark matter this value is expected to be lower than in the hadronic phase and close to 4/3. We demonstrate that the eff PT scheme is able to capture general EoS features at non-zero temperatures very well. By direct comparison, we show that when reconstructing the DD2F-SF models at various temperatures and densities from a barotropic EoS slice, the eff PT performs significantly better than the traditional ideal-gas approach with the mean relative errors in the pressure being about an order of magnitude smaller.

In a second step, we further validate our novel effPT approach by simulating NS mergers with all seven DD2F-SF models and comparing the results to simulations employing the traditional ideal-gas approach and simulations with the fully temperature- and composition-dependent EoS tables. We find that the evolution of the merger remnant is strongly influenced by the EoS changes at finite temperature. In particular, we observe that the dominant postmerger GW frequencies $f_{\rm peak}$ are consistently underestimated by several hundred Hz with the traditional ideal-gas scheme, i.e. when the temperature dependence of the phase boundaries is not considered. We also find that this approach does not reproduce the remnant evolution correctly. For instance, in some simulations we find a delayed transition to quark matter in the remnant and a corresponding shift of $f_{\rm peak}$ several milliseconds after the merger. These features are absent in simulations employing the full EoS tables. We hence caution the usage of the traditional ideal-gas scheme for hybrid EoSs in astrophysical simulations. Employing this approach implicitly makes the assumptions that the phase boundaries do not vary with temperature and that the thermal nucleonic and quark phases behave the same.

On the other hand, we find that the novel effPT scheme captures the effects of the shifting phase boundaries well, i.e. a lower onset of quark deconfinement at finite thermal energies. We find good agreement in the GW frequencies and the overall remnant dynamics compared to the simulations employing the full EoS tables. As a more rigorous test, we also simulate mergers with different system masses covering a range of regimes from systems with no or hardly any deconfined quark matter to systems close to prompt black hole formation. We find that the effPT scheme performs well in all cases. These tests demonstrate that the effPT scheme is well suited to incorporate thermal effects of hybrid models.

After validating our novel scheme, we employ it to test the impact varying phase boundaries at finite temperatures can potentially have in NS mergers for a fixed barotropic EoS. As our effPT approach requires knowledge of the phase boundaries, we use the parametric model presented in Sect. 4.4.1 to add a thermal component to both phases and model the phase transition with a Maxwell construction. A specific choice of parameters then completely determines the transition at finite $\epsilon_{\rm th}$. This also demonstrates that the knowledge of the cold EoS does not definitively fix the EoS at finite temperatures and varying onset densities are still possible in this regime. We pick the barotropic slice of the DD2F-SF-7 model [52, 283] and supplement it with two different finite-temperature phase boundaries. We find that this has a considerable impact on the overall remnant structure and the resulting GW signal. In particular, we observe changes up to roughly 650 Hz in $f_{\rm peak}$ between the two sets of phase boundaries. We stress again that these shifts fully emerge from the differences at finite temperatures as the cold EoS is identical in these models.

We then employ our effPT scheme to investigate EoSs from the literature. First, we consider the piecewise-polytropic model of Ref. [319]. In this work, the authors report a delayed onset of the phase transition in the remnant shortly after the merger which results in a characteristic frequency shift of the GW signal. We show that different shapes of the phase boundary can influence the timescale of the delayed transition or even remove this feature entirely in the sense that the formation of the quark core occurs directly after merger. We also find that even moderate shifts of the finite-temperature phase boundaries can drastically alter the inferred GW frequencies. We observe differences in $f_{\rm peak}$ of about 1600 Hz when comparing the $\Gamma_{\rm th}$ and the effPT scheme with the phase boundaries we have assumed.

We then explore a scenario where no stable hybrid stars exist meaning that the onset density of quark deconfinement at $T = 0$ has to be very large. We find that even in this case, deconfined quark matter could still be present in temporarily stable merger remnants and result in a characteristic increase of the postmerger GW frequencies compared to nucleonic EoSs. The requirement for such

an outcome is that the phase boundaries are strongly shifted to lower densities at temperatures reached in NS mergers. We consider two different scenarios here. In the first, the onset of quark deconfinement abruptly ends the mass-radius curve. This implies that very precise measurements of several high mass neutron stars in the future could still have the potential to reveal the transition providing complementary constraints. In the second case we consider, the unstable mass branch already begins before the onset density of quark matter is reached. Here, no observation of isolated neutron stars can reveal information on the QCD phase transition. Our results show that even in the second scenario, deconfined quark matter could still be present in NS merger remnants and proto-NSs. We also find that if this is the case, the threshold mass for prompt black hole formation may be characteristically reduced. Given current relations for nucleonic EoS and precise measurements of NS properties, this reduction in $M_{\rm thres}$ could be observable and would hence indicate the presence of deconfined quark matter in BNS merger remnants.

All these findings show that thermal effects in hybrid EoS are more important and complex than in purely hadronic EoS. The variations of the phase boundaries at finite temperatures can qualitatively change the EoS and hence the merger observables such as $f_{\rm peak}$. This explicitly shows the importance of GW frequencies to infer properties of the QCD phase diagram at finite temperatures complementary to the cold EoS, which can be inferred during the late inspiral phase. On the other hand, these findings also highlight the importance of heavy-ion collision experiment such as HADES [174] and future at facilities like FAIR [177, 179, 178] and NICA [180, 181] in providing complementary information on the QCD phase diagram to help interpreting observations from NS mergers. For example, the exclusion of deconfinement in a certain regime can provide important constraints for our approach.

Our eff PT scheme provides the flexibility to combine any barotropic cold EoS with different phase boundaries at finite temperatures. In particular, this includes parametric EoS like piecewise polytropic models or constant speed of sound parameterizations. Therefore, the eff PT scheme will be useful for systematic explorations of quark matter in NS mergers, as a large set of cold hybrid EoS can easily be constructed. Such a systematic study can help interpreting future merger observations to provide constraints on the zero- and finite-temperature region of the QCD phase diagram.

We recall that the eff PT scheme explicitly assumes a Maxwell-type phase transition behavior with a flat coexistence phase. Alternative constructions for the phase transition only requiring global charge conservation and allowing for charged, coexisting phases with a more complex pressure behavior also exist [252, 254, 255]. Crossover scenarios with a continuous transition from one phase to the other are another possibility. More consistent general-purpose EoSs of these scenarios are required to study their behavior at finite temperatures. Once available, the ideal-gas approach may be extended to these kinds of transitions. This may for example help solving the masquerade problem [261], i.e. a scenario where deconfined quark matter is present in cold stars, but does not exhibit any features distinct from purely hadronic stars.

Currently, we do not consider the effect of different Y_e on the EoS. As we have demonstrated, for the microphysical DD2F-SF EoS neglecting Y_e effects does not have a large impact as it still reproduces results from fully 3D tables well. However, the impact of Y_e on the onset densities may be underestimated by the DD2F-SF models, hence an extension of the eff PT scheme to also include different electron fractions is desirable.

Future work should also include performing simulations including magnetic fields as these may influence the overall dynamics [435, 436]. A more sophisticated treatment of composition effects out of weak equilibrium and the inclusion of neutrinos can also be studied in this context. As we have focused solely on the changes the thermal EoS has on the GW signal, it will also prove

interesting to explore how other merger properties such as the ejected mass and hence the resulting kilonova may be influenced by the "earlier" onset of quark deconfinement. This could also have implications for our understanding of r-process nucleosynthesis sites.

6.2. Thermal effects in equations of state containing hyperons

In the second part of this thesis, we provide the first comprehensive study to single out the differences between hyperonic and nucleonic EoS at finite temperatures and the corresponding impact on NS mergers. For this, we perform simulations with several hyperonic and purely nucleonic models employing fully temperature- and composition-dependent EoS tables as well as simulations using the ideal-gas approach with $\Gamma_{\rm th} = 1.75$ together with the respective cold EoS slice in beta-equilibrium composition. The second approach equips a cold EoS with an approximate thermal treatment suited for nucleonic models. We find that for all nucleonic models in our sample, the ideal-gas approach reproduces the dominant postmerger GW frequencies $f_{\rm peak}$ of the simulations employing the 3D table with good accuracy (within about 60 Hz). This finding demonstrates that the ideal-gas scheme remains a good approximation for currently available nucleonic EoSs.

For hyperonic models on the other hand, we find that this thermal approximation consistently overestimates $f_{\rm peak}$ by 50 Hz to 100 Hz if a non-negligible hyperon fraction is present in the systems. This difference can be attributed to the softening of hyperonic EoS at finite temperatures compared to nucleonic models. As the frequency shift is relatively small, the identification of hyperons from their thermal behavior will be very challenging and require precise measurements of postmerger frequencies only achievable with next-generation GW detectors such as the Einstein Telescope [93] or Cosmic Explorer [94]. Since the presence or absence of hyperons in neutron star is an important question for our understanding of the dense matter EoS, this illustrates the demand for new, enhanced GW observation techniques. We have also performed simulations with a mass ratio of $q = 0.8$ for two nucleonic and two hyperonic models. The results from these systems are in agreement with our finding from symmetric binaries.

Additionally, we explore how the results from hyperonic EoSs differ from an empirical relation between the tidal deformability of a $1.75\ M_\odot$ NS and $f_{\rm peak}$ for purely nucleonic EoSs. Again, we find that results from models with hyperons show slightly larger deviations than nucleonic models. It is however not straightforward to relate these differences to properties of the hyperonic EoSs as they are influenced both the hyperon and the nucleon interactions within the model.

We also show that the frequency shift correlates with the amount of hyperons present in the merger remnant. This amount depends on the mass of the system and also on the onset density of hyperon production. Very small admixtures of hyperons, i.e. high onset densities, do not lead to changes compared to purely nucleonic models and hyperons remain undetected. However, we demonstrate that in our hyperonic EoS sample relatively small hyperon fractions in the remnant $\bar{Y}_{\rm hyp} < 5\%$ are sufficient to produce a larger shift Δf than all our nucleonic EoSs. This implies that the threshold of hyperon production does not need to be exceeded by much to result in observable signatures of hyperons. For larger $\bar{Y}_{\rm hyp}$, we observe a saturation in the GW frequency shifts attributed to hyperons. This could indicate that even for systems at higher masses or lower onset densities, which would contain substantial amounts of hyperons, the effect on the GW signal may not be significantly more pronounced than in our study.

We recall that the frequency shifts we observe are not directly observable quantities themselves. Since only one true neutron star EoS exists, a specific binary configuration will only provide a single value of $f_{\rm peak}$. To infer shifts, an observed value has to be compared to models with different thermal approaches. This requires accurate simulations, a good knowledge of the cold EoS and

a sophisticated understanding of scatter in empirical relations. As we demonstrate, this effort is motivated by the difficulties to infer the presence of hyperons from the cold EoS alone since their impact on stellar structure may be hard to distinguish from a purely nucleonic model. Attempts to detect the possible influence of hyperons from the observation of isolated neutron star may thus require similar or even higher precision. Any observational feature that can be linked to hyperons is therefore highly desirable.

To quantify the impact of hyperons on the thermal EoS behavior, we assume that the cold EoS does not allow for any conclusions on the presence of hyperons at all. This is of course a very conservative and actually incorrect assumption. Any further constraints on the EoS at zero temperature will help narrowing down the model space, which will increase our knowledge on which scenarios including or excluding hyperons are still compatible with observations.

Such constraints will also come from advances on experimental determination of interactions involving nucleons and hyperons at CLAS [219], LHC [224, 225, 226, 227, 228, 229], J-PARC [220, 221, 222] or the future FAIR facility [177, 178, 179] and further progress on theoretical models [4, 202, 205] and can be included in upcoming analyses. Also ab-initio calculations considering hyperons as relevant degrees of freedom [200, 201, 203, 204] and other astronomical observations like cooling neutron stars [160, 162, 163, 197, 235, 237, 236, 238, 239, 8, 9] or core-collapse supernovae [231, 232, 233, 234] may provide further insights.

As we limit ourselves to a fixed system mass and mostly symmetric binaries, a straightforward extension to our study would be to investigate different masses and mass ratios. Additionally, one could explore the impact hyperons have on other observable quantities apart from $f_{\rm peak}$ such as secondary GW peaks or the threshold mass to prompt black hole formation. It will also be advantageous to compare our findings to other simulations codes employing different numerical treatments to test the robustness of our results. In particular, these should include neutrino treatments as hyperonic EoSs allow for more weak reactions to take place than nucleonic EoSs. Recent works have also shown the importance of weak processes for NS mergers in the context of varying bulk viscosity [437, 438, 439], as this can influence the temperatures in the remnant and hence the GW frequencies. Future work can also extend these analyses to hyperonic EoSs, as changes in the bulk viscosity are expected in this case [440].

We also remark that a frequency shift incompatible with purely nucleonic matter is a general indication of additional degrees of freedom that do not necessarily have to be hyperons. As we discuss in Chapter 4, deconfined quark matter at zero and finite temperatures can also affect the GW frequencies. In the examples we consider in this work, the shifts in $f_{\rm peak}$ are more significant than those caused by hyperons. It may hence be possible to disentangle the effects of hyperons and a strong phase transition to deconfined quark matter as the latter case would produce shifts incompatible with both nucleons and hyperons. For other cases with a more continuous transition or a crossover scenario, this is likely not so straightforward. As hyperons appear smoothly one may even speculate that the impact of a crossover scenario to deconfined quark matter could result in similar effects as we found in this work. Likewise pions could affect the EoS as recently shown in [441]. To help discriminating these possibilities, a combination of lab experiments, astronomical observations, numerical simulations and theoretical calculations will be needed.

Lastly, we address our findings in the light of recent state-of-the-art calculations from chiral effective field theory (χEFT). These calculations suggest that purely nucleonic matter could also have $\Gamma_{\rm th}$ significantly lower than 1.75, potentially even below 1, which would result in negative thermal pressure [431, 432]. As χEFT only produces reliable results up to around two times saturation density, the resulting EoS currently cannot be used in merger simulations. To explore this scenario, we develop a toy model that mimics the suggested behavior of $\Gamma_{\rm th}$ in nuclear matter and additionally

includes hyperons. We find that hyperons produce an additional EoS softening at finite temperatures. Hence, a similar frequency shift relative to the nuclear model is likely to occur. From this, we conclude that the findings of this work should still hold in the case where nuclear matter already features a reduction in thermal pressure. We also remark that phenomenological models developed to extrapolate the EoS from χEFT calculations suggest $\Gamma_{\rm th}$ may rise again at higher densities [442]. This could potentially result in an average thermal index in the remnant not too different from the values we find in our nucleonic EoS sample. This topic also needs to be further explored with more realistic microscopical calculation in future work.

A. Improved inspiral

During the work on this thesis, the initial conditions at the start if the simulation were modified. As described in Sect. 2.1, in the original code version the angular velocities of the stars are adjusted during the initial relaxation phase in such a way to maintain circular orbits. As the backreaction scheme mimicking gravitational-wave emission is switched off at this stage, the stars have zero radial velocity at the beginning of the simulation phase. Only once the backreaction is turned on, the stars begin to approach each other. We find that this scheme leads to eccentric orbits during the inspiral.

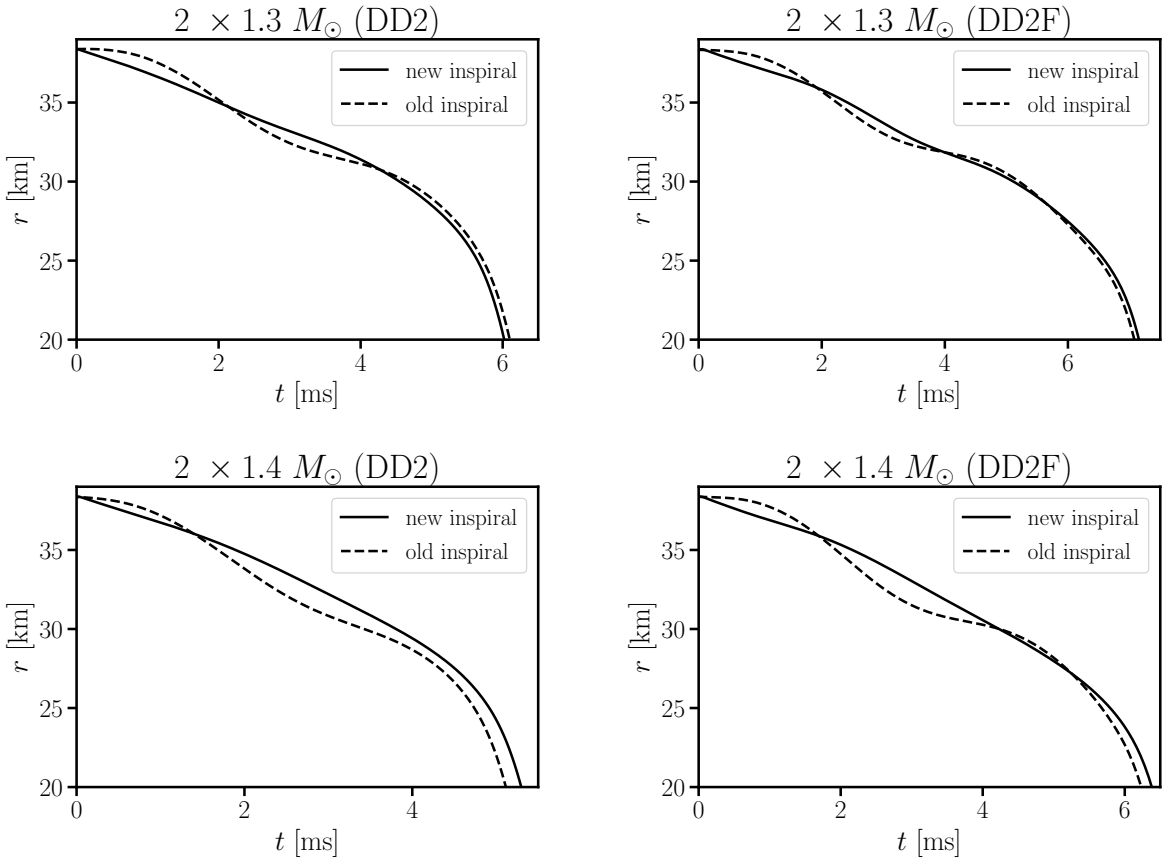

Figure A.1.: Evolution of the coordinate separation (center-to-center) from two inspiraling neutron stars. Different panels show results from different system mass configurations and equations of state. $t = 0$ corresponds to the end of the relaxation phase. Dashed lines show results from simulations with purely tangetial velocities of the stars after the end of the relaxation and solid lines depict inspirals with the new scheme applying an initial radial velocity. See text for details.

To reduce this eccentricity, we follow the ideas of [443] and add an additional radial velocity to the system at the end of the initial relaxation phase to provide a more realistic system configuration We find that the empirical linear expression

$$\frac{\mathrm{d}r}{\mathrm{d}t} = -0.00628M + 0.01134 + 3.839 \times 10^{-5}(r - 26) \ , \tag{A.1}$$

with $M = M_1 + M_2$ works well for most EoS models and system configurations. Here, r is the binary coordinate separation (center-to-center) and $M_{1,2}$ are the gravitational masses of the two stars at infinite orbital separation. The second terms slightly adjusts the radial velocity if larger initial separations are chosen.

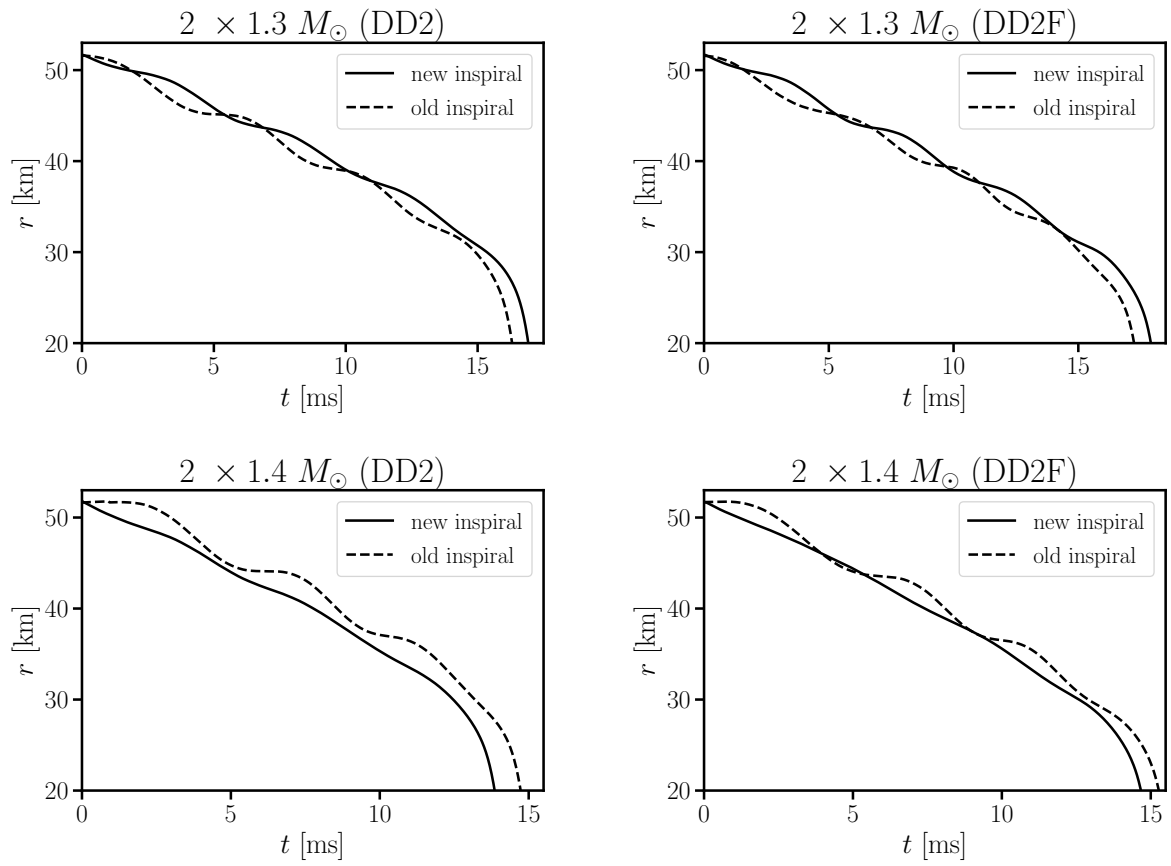

Figure A.2.: Same as Fig. A.1, but at a larger initial binary separation.

We add these radial velocity by switching on the backreaction scheme and applying a damping force to each particle to move the system to the desired velocity. After each time step, we manually set the system back onto the circular orbit. At this stage we also need to enforce an angular velocity.

For this, we use the post-Newtonian expression from Ref. [444] assuming zero spins for both stars

$$\Omega = \frac{M^{1/2}}{r^{3/2}}\left[1 - \frac{1}{2}\frac{3q^2+5q+3}{(1+q)^2}\frac{M}{r} + \frac{1}{16}\frac{24q^4+103q^3+164q^2+103q+24}{(1+q)^4}\left(\frac{M}{r}\right)^2 + \left(\frac{167\pi^2 q}{128(1+q)^2} - \frac{120q^6+2744q^5+10049q^4+14820q^3+10049q^2+2744q+120}{96(1+q)^6}\right) \times \left(\frac{M}{r}\right)^2\right]. \tag{A.2}$$

In this expression, Ω is the primitive angular coordinate velocity $q = M_2/M_1 < 1$ is the binary mass ratio. Both velocities are applied such that the coordinate center of mass calculated with the gravitational masses of the stars remains at zero velocity.

In Fig. A.1, we plot the center-to-center coordinate separation of the inspiraling stars from $1.3 - 1.3\ M_\odot$ and $1.4 - 1.4\ M_\odot$ binary neutron star merger simulations with the two equation of state (EoS) models DD2 and DD2F, respectively. In all cases, the initial separation of the two stars is $r = 26$. Dashed lines show the results with the old code version and no initial radial velocities while solid lines show results with new inpiral scheme. We clearly see the orbital eccentricity in the inspiral from the old code version as oscillations in r. The new inspiral scheme on the other hand generally shows smaller eccentricity. For the DD2F model, we see that our approach performs slightly worse than for the DD2 EoS, but still better than the old code version.

We perform additional simulations with the same EoSs and system masses, but with a larger initial center-to-center separation of $r = 35$. We plot the evolution of r in Fig. A.2. As before, we find that our new approach reduces the eccentricity compared to simulations with no initial radial velocity. However, at this separation we see some remaining oscillations in the $1.3-1.3\ M_\odot$ systems for both EoSs. In order to allow for manual adjustments, hand-picked values of Ω and $\mathrm{d}r/\mathrm{d}t$ can also be set at the beginning of the simulation. If provided, these will be used instead of the formulas in Eq. (A.1) and Eq. (A.2)

Bibliography

[1] H.-T. Janka, "Explosion Mechanisms of Core-Collapse Supernovae," *Ann. Rev. Nucl. Part. Sci.*, vol. 62, pp. 407–451, 2012.

[2] F. Özel and P. Freire, "Masses, Radii, and the Equation of State of Neutron Stars," *Ann. Rev. Astron. Astrophys.*, vol. 54, pp. 401–440, 2016.

[3] M. Oertel, M. Hempel, T. Klähn, and S. Typel, "Equations of state for supernovae and compact stars," *Rev. Mod. Phys.*, vol. 89, no. 1, p. 015007, 2017.

[4] K. Hebeler, "Three-nucleon forces: Implementation and applications to atomic nuclei and dense matter," *Phys. Rept.*, vol. 890, pp. 1–116, 2021.

[5] G. F. Burgio, H. J. Schulze, I. Vidana, and J. B. Wei, "Neutron stars and the nuclear equation of state," *Prog. Part. Nucl. Phys.*, vol. 120, p. 103879, 2021.

[6] V. A. Ambartsumyan and G. S. Saakyan, "The Degenerate Superdense Gas of Elementary Particles," *Sov. Astron.*, vol. 4, p. 187, 1960.

[7] D. Blaschke and N. Chamel, "Phases of dense matter in compact stars," *Astrophys. Space Sci. Libr.*, vol. 457, pp. 337–400, 2018.

[8] A. Sedrakian, J.-J. Li, and F. Weber, "Hyperonization in Compact Stars," in *Astrophysics in the XXI Century with Compact Stars.* (C. Vasconcellos, ed.), pp. 153–199, Singapore: World Scientific, 2022.

[9] A. Sedrakian, J.-J. Li, and F. Weber, "Heavy baryons in compact stars," *Prog. Part. Nucl. Phys.*, vol. 131, p. 104041, 2023.

[10] R. F. Sawyer, "Condensed pi- phase in neutron star matter," *Phys. Rev. Lett.*, vol. 29, pp. 382–385, 1972.

[11] A. Akmal and V. R. Pandharipande, "Spin - isospin structure and pion condensation in nucleon matter," *Phys. Rev. C*, vol. 56, pp. 2261–2279, 1997.

[12] T. Malik, S. Banik, and D. Bandyopadhyay, "New equation of state involving Bose–Einstein condensate of antikaon for supernova and neutron star merger simulations," *Eur. Phys. J. ST*, vol. 230, no. 2, pp. 561–566, 2021.

[13] V. B. Thapa, M. Sinha, J. J. Li, and A. Sedrakian, "Massive Δ-resonance admixed hypernuclear stars with antikaon condensations," *Phys. Rev. D*, vol. 103, no. 6, p. 063004, 2021.

[14] A. R. Bodmer, "Collapsed nuclei," *Phys. Rev. D*, vol. 4, pp. 1601–1606, 1971.

[15] G. Baym, T. Hatsuda, T. Kojo, P. D. Powell, Y. Song, and T. Takatsuka, "From hadrons to quarks in neutron stars: a review," *Rept. Prog. Phys.*, vol. 81, no. 5, p. 056902, 2018.

[16] M. G. Alford, S. Han, and K. Schwenzer, "Signatures for quark matter from multi-messenger observations," *J. Phys. G*, vol. 46, no. 11, p. 114001, 2019.

[17] M. G. Orsaria, G. Malfatti, M. Mariani, I. F. Ranea-Sandoval, F. García, W. M. Spinella, G. A. Contrera, G. Lugones, and F. Weber, "Phase transitions in neutron stars and their links to gravitational waves," *J. Phys. G*, vol. 46, no. 7, p. 073002, 2019.

[18] K. A. Postnov and L. R. Yungelson, "The Evolution of Compact Binary Star Systems," *Living Rev. Rel.*, vol. 17, p. 3, 2014.

[19] T. M. Tauris *et al.*, "Formation of Double Neutron Star Systems," *Astrophys. J.*, vol. 846, no. 2, p. 170, 2017.

[20] D. Radice, S. Bernuzzi, and A. Perego, "The Dynamics of Binary Neutron Star Mergers and GW170817," *Ann. Rev. Nucl. Part. Sci.*, vol. 70, pp. 95–119, 2020.

[21] R. Oechslin, H. T. Janka, and A. Marek, "Relativistic neutron star merger simulations with non-zero temperature equations of state. 1. Variation of binary parameters and equation of state," *Astron. Astrophys.*, vol. 467, p. 395, 2007.

[22] A. Bauswein, H. T. Janka, and R. Oechslin, "Testing Approximations of Thermal Effects in Neutron Star Merger Simulations," *Phys. Rev. D*, vol. 82, p. 084043, 2010.

[23] M. Shibata and K. Hotokezaka, "Merger and Mass Ejection of Neutron-Star Binaries," *Ann. Rev. Nucl. Part. Sci.*, vol. 69, pp. 41–64, 2019.

[24] H.-T. Janka and A. Bauswein, *Dynamics and Equation of State Dependencies of Relevance for Nucleosynthesis in Supernovae and Neutron Star Mergers*, pp. 1–98. Singapore: Springer Nature Singapore, 2023.

[25] S. Bernuzzi, "Neutron Star Merger Remnants," *Gen. Rel. Grav.*, vol. 52, no. 11, p. 108, 2020.

[26] M. Shibata, "Constraining nuclear equations of state using gravitational waves from hypermassive neutron stars," *Phys. Rev. Lett.*, vol. 94, p. 201101, 2005.

[27] S. Köppel, L. Bovard, and L. Rezzolla, "A General-relativistic Determination of the Threshold Mass to Prompt Collapse in Binary Neutron Star Mergers," *Astrophys. J. Lett.*, vol. 872, no. 1, p. L16, 2019.

[28] A. Bauswein, S. Blacker, V. Vijayan, N. Stergioulas, K. Chatziioannou, J. A. Clark, N.-U. F. Bastian, D. B. Blaschke, M. Cierniak, and T. Fischer, "Equation of state constraints from the threshold binary mass for prompt collapse of neutron star mergers," *Phys. Rev. Lett.*, vol. 125, no. 14, p. 141103, 2020.

[29] A. Bauswein, S. Blacker, G. Lioutas, T. Soultanis, V. Vijayan, and N. Stergioulas, "Systematics of prompt black-hole formation in neutron star mergers," *Phys. Rev. D*, vol. 103, no. 12, p. 123004, 2021.

[30] M. Hempel and J. Schaffner-Bielich, "Statistical Model for a Complete Supernova Equation of State," *Nucl. Phys. A*, vol. 837, pp. 210–254, 2010.

[31] A. W. Steiner, M. Hempel, and T. Fischer, "Core-collapse supernova equations of state based on neutron star observations," *Astrophys. J.*, vol. 774, p. 17, 2013.

[32] B. P. Abbott *et al.*, "GW170817: Observation of Gravitational Waves from a Binary Neutron Star Inspiral," *Phys. Rev. Lett.*, vol. 119, no. 16, p. 161101, 2017.

[33] B. P. Abbott *et al.*, "GW190425: Observation of a Compact Binary Coalescence with Total Mass $\sim 3.4 M_{\odot}$," *Astrophys. J. Lett.*, vol. 892, no. 1, p. L3, 2020.

[34] T. Dietrich, T. Hinderer, and A. Samajdar, "Interpreting Binary Neutron Star Mergers: Describing the Binary Neutron Star Dynamics, Modelling Gravitational Waveforms, and Analyzing Detections," *Gen. Rel. Grav.*, vol. 53, no. 3, p. 27, 2021.

[35] L. S. Finn and D. F. Chernoff, "Observing binary inspiral in gravitational radiation: One interferometer," *Phys. Rev. D*, vol. 47, pp. 2198–2219, 1993.

[36] E. E. Flanagan and T. Hinderer, "Constraining neutron star tidal Love numbers with gravitational wave detectors," *Phys. Rev. D*, vol. 77, p. 021502, 2008.

[37] T. Hinderer, "Tidal Love numbers of neutron stars," *Astrophys. J.*, vol. 677, pp. 1216–1220, 2008.

[38] T. Hinderer, B. D. Lackey, R. N. Lang, and J. S. Read, "Tidal deformability of neutron stars with realistic equations of state and their gravitational wave signatures in binary inspiral," *Phys. Rev. D*, vol. 81, p. 123016, 2010.

[39] K. Chatziioannou, "Neutron star tidal deformability and equation of state constraints," *Gen. Rel. Grav.*, vol. 52, no. 11, p. 109, 2020.

[40] M. Shibata and K. Taniguchi, "Merger of binary neutron stars to a black hole: disk mass, short gamma-ray bursts, and quasinormal mode ringing," *Phys. Rev. D*, vol. 73, p. 064027, 2006.

[41] J. Clark, A. Bauswein, L. Cadonati, H. T. Janka, C. Pankow, and N. Stergioulas, "Prospects For High Frequency Burst Searches Following Binary Neutron Star Coalescence With Advanced Gravitational Wave Detectors," *Phys. Rev. D*, vol. 90, no. 6, p. 062004, 2014.

[42] H. Bandyopadhyay, D. Radice, A. Prakash, A. Dhani, D. Logoteta, A. Perego, and R. Kashyap, "Do black holes remember what they are made of?," *arXiv e-prints*, p. arXiv:2312.11620, 2023.

[43] N. Stergioulas, A. Bauswein, K. Zagkouris, and H.-T. Janka, "Gravitational waves and nonaxisymmetric oscillation modes in mergers of compact object binaries," *Mon. Not. Roy. Astron. Soc.*, vol. 418, p. 427, 2011.

[44] A. Bauswein, H. T. Janka, K. Hebeler, and A. Schwenk, "Equation-of-state dependence of the gravitational-wave signal from the ring-down phase of neutron-star mergers," *Phys. Rev. D*, vol. 86, p. 063001, 2012.

[45] K. Hotokezaka, K. Kiuchi, K. Kyutoku, H. Okawa, Y.-i. Sekiguchi, M. Shibata, and K. Taniguchi, "Mass ejection from the merger of binary neutron stars," *Phys. Rev. D*, vol. 87, p. 024001, 2013.

[46] K. Takami, L. Rezzolla, and L. Baiotti, "Constraining the Equation of State of Neutron Stars from Binary Mergers," *Phys. Rev. Lett.*, vol. 113, no. 9, p. 091104, 2014.

[47] S. Bernuzzi, T. Dietrich, and A. Nagar, "Modeling the complete gravitational wave spectrum of neutron star mergers," *Phys. Rev. Lett.*, vol. 115, no. 9, p. 091101, 2015.

[48] A. Bauswein and N. Stergioulas, "Unified picture of the post-merger dynamics and gravitational wave emission in neutron star mergers," *Phys. Rev. D*, vol. 91, no. 12, p. 124056, 2015.

[49] T. Soultanis, A. Bauswein, and N. Stergioulas, "Analytic models of the spectral properties of gravitational waves from neutron star merger remnants," *Phys. Rev. D*, vol. 105, no. 4, p. 043020, 2022.

[50] L. Baiotti, "Gravitational waves from neutron star mergers and their relation to the nuclear equation of state," *Prog. Part. Nucl. Phys.*, vol. 109, p. 103714, 2019.

[51] A. Bauswein and N. Stergioulas, "Spectral classification of gravitational-wave emission and equation of state constraints in binary neutron star mergers," *J. Phys. G*, vol. 46, no. 11, p. 113002, 2019.

[52] A. Bauswein, N.-U. F. Bastian, D. B. Blaschke, K. Chatziioannou, J. A. Clark, T. Fischer, and M. Oertel, "Identifying a first-order phase transition in neutron star mergers through gravitational waves," *Phys. Rev. Lett.*, vol. 122, no. 6, p. 061102, 2019.

[53] S. Blacker, N.-U. F. Bastian, A. Bauswein, D. B. Blaschke, T. Fischer, M. Oertel, T. Soultanis, and S. Typel, "Constraining the onset density of the hadron-quark phase transition with gravitational-wave observations," *Phys. Rev. D*, vol. 102, no. 12, p. 123023, 2020.

[54] M. Wijngaarden, K. Chatziioannou, A. Bauswein, J. A. Clark, and N. J. Cornish, "Probing neutron stars with the full premerger and postmerger gravitational wave signal from binary coalescences," *Phys. Rev. D*, vol. 105, no. 10, p. 104019, 2022.

[55] J. Aasi *et al.*, "Advanced LIGO," *Class. Quant. Grav.*, vol. 32, p. 074001, 2015.

[56] F. Acernese *et al.*, "Advanced Virgo: a second-generation interferometric gravitational wave detector," *Class. Quant. Grav.*, vol. 32, no. 2, p. 024001, 2015.

[57] B. P. Abbott *et al.*, "Properties of the binary neutron star merger GW170817," *Phys. Rev. X*, vol. 9, no. 1, p. 011001, 2019.

[58] B. P. Abbott *et al.*, "Search for Post-merger Gravitational Waves from the Remnant of the Binary Neutron Star Merger GW170817," *Astrophys. J. Lett.*, vol. 851, no. 1, p. L16, 2017.

[59] A. Goldstein *et al.*, "An Ordinary Short Gamma-Ray Burst with Extraordinary Implications: Fermi-GBM Detection of GRB 170817A," *Astrophys. J. Lett.*, vol. 848, no. 2, p. L14, 2017.

[60] V. Savchenko *et al.*, "INTEGRAL Detection of the First Prompt Gamma-Ray Signal Coincident with the Gravitational-wave Event GW170817," *Astrophys. J. Lett.*, vol. 848, no. 2, p. L15, 2017.

[61] B. P. Abbott *et al.*, "Gravitational Waves and Gamma-rays from a Binary Neutron Star Merger: GW170817 and GRB 170817A," *Astrophys. J. Lett.*, vol. 848, no. 2, p. L13, 2017.

[62] B. P. Abbott *et al.*, "Multi-messenger Observations of a Binary Neutron Star Merger," *Astrophys. J. Lett.*, vol. 848, no. 2, p. L12, 2017.

[63] D. A. Coulter *et al.*, "Swope Supernova Survey 2017a (SSS17a), the Optical Counterpart to a Gravitational Wave Source," *Science*, vol. 358, p. 1556, 2017.

[64] S. Valenti, D. J. Sand, S. Yang, E. Cappellaro, L. Tartaglia, A. Corsi, S. W. Jha, D. E. Reichart, J. Haislip, and V. Kouprianov, "The discovery of the electromagnetic counterpart of GW170817: kilonova AT 2017gfo/DLT17ck," *Astrophys. J. Lett.*, vol. 848, no. 2, p. L24, 2017.

[65] M. Soares-Santos *et al.*, "The Electromagnetic Counterpart of the Binary Neutron Star Merger LIGO/Virgo GW170817. I. Discovery of the Optical Counterpart Using the Dark Energy Camera," *Astrophys. J. Lett.*, vol. 848, no. 2, p. L16, 2017.

[66] M. Nicholl *et al.*, "The Electromagnetic Counterpart of the Binary Neutron Star Merger LIGO/VIRGO GW170817. III. Optical and UV Spectra of a Blue Kilonova From Fast Polar Ejecta," *Astrophys. J. Lett.*, vol. 848, no. 2, p. L18, 2017.

[67] V. A. Villar *et al.*, "The Combined Ultraviolet, Optical, and Near-Infrared Light Curves of the Kilonova Associated with the Binary Neutron Star Merger GW170817: Unified Data Set, Analytic Models, and Physical Implications," *Astrophys. J. Lett.*, vol. 851, no. 1, p. L21, 2017.

[68] I. Andreoni *et al.*, "Follow up of GW170817 and its electromagnetic counterpart by Australian-led observing programs," *Publ. Astron. Soc. Austral.*, vol. 34, p. e069, 2017.

[69] L.-X. Li and B. Paczynski, "Transient events from neutron star mergers," *Astrophys. J. Lett.*, vol. 507, p. L59, 1998.

[70] B. D. Metzger, G. Martinez-Pinedo, S. Darbha, E. Quataert, A. Arcones, D. Kasen, R. Thomas, P. Nugent, I. V. Panov, and N. T. Zinner, "Electromagnetic Counterparts of Compact Object Mergers Powered by the Radioactive Decay of R-process Nuclei," *Mon. Not. Roy. Astron. Soc.*, vol. 406, p. 2650, 2010.

[71] D. Kasen, B. Metzger, J. Barnes, E. Quataert, and E. Ramirez-Ruiz, "Origin of the heavy elements in binary neutron-star mergers from a gravitational wave event," *Nature*, vol. 551, p. 80, 2017.

[72] B. D. Metzger, "Kilonovae," *Living Rev. Rel.*, vol. 23, no. 1, p. 1, 2020.

[73] C. J. Horowitz *et al.*, "r-Process Nucleosynthesis: Connecting Rare-Isotope Beam Facilities with the Cosmos," *J. Phys. G*, vol. 46, no. 8, p. 083001, 2019.

[74] T. Kajino, W. Aoki, A. B. Balantekin, R. Diehl, M. A. Famiano, and G. J. Mathews, "Current status of r -process nucleosynthesis," *Prog. Part. Nucl. Phys.*, vol. 107, pp. 109–166, 2019.

[75] J. J. Cowan, C. Sneden, J. E. Lawler, A. Aprahamian, M. Wiescher, K. Langanke, G. Martínez-Pinedo, and F.-K. Thielemann, "Origin of the heaviest elements: The rapid neutron-capture process," *Rev. Mod. Phys.*, vol. 93, no. 1, p. 15002, 2021.

[76] D. Watson *et al.*, "Identification of strontium in the merger of two neutron stars," *Nature*, vol. 574, no. 7779, pp. 497–500, 2019.

[77] J. M. Lattimer and D. N. Schramm, "Black-hole-neutron-star collisions," *Astrophys. J. Lett.*, vol. 192, p. L145, 1974.

[78] E. Symbalisty and D. N. Schramm, "Neutron Star Collisions and the r-Process," *Astrophys. Lett.*, vol. 22, p. 143, 1982.

[79] N. Farrow, X.-J. Zhu, and E. Thrane, "The mass distribution of Galactic double neutron stars," *Astrophys. J.*, vol. 876, no. 1, p. 18, 2019.

[80] M. W. Coughlin *et al.*, "GROWTH on S190425z: Searching thousands of square degrees to identify an optical or infrared counterpart to a binary neutron star merger with the Zwicky Transient Facility and Palomar Gattini IR," *Astrophys. J. Lett.*, vol. 885, no. 1, p. L19, 2019.

[81] R. Dudi, A. Adhikari, B. Brügmann, T. Dietrich, K. Hayashi, K. Kawaguchi, K. Kiuchi, K. Kyutoku, M. Shibata, and W. Tichy, "Investigating GW190425 with numerical-relativity simulations," *Phys. Rev. D*, vol. 106, no. 8, p. 084039, 2022.

[82] A. Camilletti, L. Chiesa, G. Ricigliano, A. Perego, L. C. Lippold, S. Padamata, S. Bernuzzi, D. Radice, D. Logoteta, and F. M. Guercilena, "Numerical relativity simulations of the neutron star merger GW190425: microphysics and mass ratio effects," *Monthly Notices of the Royal Astronomical Society*, vol. 516, no. 4, pp. 4760–4781, 2022.

[83] B. P. Abbott *et al.*, "GWTC-1: A Gravitational-Wave Transient Catalog of Compact Binary Mergers Observed by LIGO and Virgo during the First and Second Observing Runs," *Phys. Rev. X*, vol. 9, no. 3, p. 031040, 2019.

[84] R. Abbott *et al.*, "GWTC-2: Compact Binary Coalescences Observed by LIGO and Virgo During the First Half of the Third Observing Run," *Phys. Rev. X*, vol. 11, p. 021053, 2021.

[85] R. Abbott *et al.*, "GWTC-2.1: Deep extended catalog of compact binary coalescences observed by LIGO and Virgo during the first half of the third observing run," *Phys. Rev. D*, vol. 109, no. 2, p. 022001, 2024.

[86] R. Abbott *et al.*, "GWTC-3: Compact Binary Coalescences Observed by LIGO and Virgo during the Second Part of the Third Observing Run," *Phys. Rev. X*, vol. 13, no. 4, p. 041039, 2023.

[87] R. Abbott *et al.*, "Observation of Gravitational Waves from Two Neutron Star–Black Hole Coalescences," *Astrophys. J. Lett.*, vol. 915, no. 1, p. L5, 2021.

[88] T. Baker, E. Bellini, P. G. Ferreira, M. Lagos, J. Noller, and I. Sawicki, "Strong constraints on cosmological gravity from GW170817 and GRB 170817A," *Phys. Rev. Lett.*, vol. 119, no. 25, p. 251301, 2017.

[89] B. P. Abbott *et al.*, "A gravitational-wave standard siren measurement of the Hubble constant," *Nature*, vol. 551, no. 7678, pp. 85–88, 2017.

[90] T. Akutsu *et al.*, "KAGRA: 2.5 Generation Interferometric Gravitational Wave Detector," *Nature Astron.*, vol. 3, no. 1, pp. 35–40, 2019.

[91] B. P. Abbott *et al.*, "Prospects for observing and localizing gravitational-wave transients with Advanced LIGO, Advanced Virgo and KAGRA," *Living Rev. Rel.*, vol. 21, no. 1, p. 3, 2018.

[92] B. Iyer, T. Souradeep, C. Unnikrishnan, S. Dhurandhar, S. Raja, and A. Sengupta, "Ligo-india," tech. rep., Technical Report M1100296-v2, IndIGO, India https://dcc.ligo.org/LIGO-M1100296/public, 2011.

[93] M. Punturo *et al.*, "The Einstein Telescope: A third-generation gravitational wave observatory," *Class. Quant. Grav.*, vol. 27, p. 194002, 2010.

[94] D. Reitze *et al.*, "Cosmic Explorer: The U.S. Contribution to Gravitational-Wave Astronomy beyond LIGO," *Bull. Am. Astron. Soc.*, vol. 51, no. 7, p. 035, 2019.

[95] B. P. Abbott *et al.*, "Exploring the Sensitivity of Next Generation Gravitational Wave Detectors," *Class. Quant. Grav.*, vol. 34, no. 4, p. 044001, 2017.

[96] T. Fischer, S. C. Whitehouse, A. Mezzacappa, F. K. Thielemann, and M. Liebendorfer, "Protoneutron star evolution and the neutrino driven wind in general relativistic neutrino radiation hydrodynamics simulations," *Astron. Astrophys.*, vol. 517, p. A80, 2010.

[97] E. O'Connor and C. D. Ott, "Black Hole Formation in Failing Core-Collapse Supernovae," *Astrophys. J.*, vol. 730, p. 70, 2011.

[98] Y. Sekiguchi, K. Kiuchi, K. Kyutoku, and M. Shibata, "Dynamical mass ejection from binary neutron star mergers: Radiation-hydrodynamics study in general relativity," *Phys. Rev. D*, vol. 91, no. 6, p. 064059, 2015.

[99] A. R. Raduta, F. Nacu, and M. Oertel, "Equations of state for hot neutron stars," *Eur. Phys. J. A*, vol. 57, no. 12, p. 329, 2021.

[100] S. Typel, M. Oertel, and T. Klähn, "CompOSE CompStar online supernova equations of state harmonising the concert of nuclear physics and astrophysics compose.obspm.fr," *Phys. Part. Nucl.*, vol. 46, no. 4, pp. 633–664, 2015.

[101] S. Typel *et al.*, "CompOSE Reference Manual," *Eur. Phys. J. A*, vol. 58, no. 11, p. 221, 2022.

[102] W. Greiner, S. Schramm, and E. Stein, *Quantum chromodynamics*. Berlin, Heidelberg: Springer Berlin Heidelberg, 2007.

[103] N. Brambilla *et al.*, "QCD and Strongly Coupled Gauge Theories: Challenges and Perspectives," *Eur. Phys. J. C*, vol. 74, no. 10, p. 2981, 2014.

[104] J. J. Ethier and E. R. Nocera, "Parton Distributions in Nucleons and Nuclei," *Ann. Rev. Nucl. Part. Sci.*, vol. 70, pp. 43–76, 2020.

[105] G. Fiorella Burgio and A. F. Fantina, "Nuclear Equation of state for Compact Stars and Supernovae," *Astrophys. Space Sci. Libr.*, vol. 457, pp. 255–335, 2018.

[106] G. F. Burgio and I. Vidana, "The Equation of State of Nuclear Matter : from Finite Nuclei to Neutron Stars," *Universe*, vol. 6, no. 8, p. 119, 2020.

[107] B. D. Serot, "Quantum hadrodynamics," *Rept. Prog. Phys.*, vol. 55, pp. 1855–1946, 1992.

[108] T. Niksic, D. Vretenar, and P. Ring, "Relativistic Nuclear Energy Density Functionals: Mean-Field and Beyond," *Prog. Part. Nucl. Phys.*, vol. 66, pp. 519–548, 2011.

[109] T. H. R. Skyrme, "CVII. The nuclear surface," *Phil. Mag.*, vol. 1, pp. 1043–1054, 1956.

[110] D. Vautherin and D. M. Brink, "Hartree-Fock calculations with Skyrme's interaction. 1. Spherical nuclei," *Phys. Rev. C*, vol. 5, pp. 626–647, 1972.

[111] P. Quentin and H. Flocard, "Self-consistent calculations of nuclear properties with phenomenological effective forces," *Ann. Rev. Nucl. Part. Sci.*, vol. 28, pp. 523–594, 1978.

[112] M. Dutra, O. Lourenco, J. S. Sa Martins, A. Delfino, J. R. Stone, and P. D. Stevenson, "Skyrme Interaction and Nuclear Matter Constraints," *Phys. Rev. C*, vol. 85, p. 035201, 2012.

[113] J. Decharge and D. Gogny, "Hartree-Fock-Bogolyubov calculations with the D1 effective interactions on spherical nuclei," *Phys. Rev. C*, vol. 21, pp. 1568–1593, 1980.

[114] R. Sellahewa and A. Rios, "Isovector properties of the Gogny interaction," *Phys. Rev. C*, vol. 90, no. 5, p. 054327, 2014.

[115] T. Krüger, I. Tews, K. Hebeler, and A. Schwenk, "Neutron matter from chiral effective field theory interactions," *Phys. Rev. C*, vol. 88, p. 025802, 2013.

[116] I. E. Lagaris and V. R. Pandharipande, "PHENOMENOLOGICAL TWO NUCLEON INTERACTION OPERATOR," *Nucl. Phys. A*, vol. 359, pp. 331–348, 1981.

[117] R. Brockmann and R. Machleidt, "Relativistic nuclear structure. 1: Nuclear matter," *Phys. Rev. C*, vol. 42, pp. 1965–1980, 1990.

[118] R. Schiavilla, V. R. Pandharipande, and R. B. Wiringa, "Momentum distributions in a A = 3 and 4 nuclei," *Nucl. Phys. A*, vol. 449, pp. 219–242, 1986.

[119] R. B. Wiringa, V. G. J. Stoks, and R. Schiavilla, "An Accurate nucleon-nucleon potential with charge independence breaking," *Phys. Rev. C*, vol. 51, pp. 38–51, 1995.

[120] B. S. Pudliner, V. R. Pandharipande, J. Carlson, and R. B. Wiringa, "Quantum Monte Carlo calculations of A <= 6 nuclei," *Phys. Rev. Lett.*, vol. 74, pp. 4396–4399, 1995.

[121] Z. H. Li and H. J. Schulze, "Neutron star structure with modern nucleonic three-body forces," *Phys. Rev. C*, vol. 78, p. 028801, 2008.

[122] Z. H. Li, U. Lombardo, H. J. Schulze, and W. Zuo, "Consistent nucleon-nucleon potentials and three-body forces," *Phys. Rev. C*, vol. 77, p. 034316, 2008.

[123] M. Baldo, "Nuclear Methods And The Nuclear Equation Of State," *International Review of Nuclear Physics*, vol. 8, 1999.

[124] M. Baldo and H. J. Schulze, "Proton pairing in neutron stars," *Phys. Rev. C*, vol. 75, p. 025802, 2007.

[125] W. H. Dickhoff and D. V. Van Neck, *Many-body theory exposed! Propagator description of quantum mechanics in many-body systems, Second Edition*. Singapore: World Scientific, 2008.

[126] H. Togashi and M. Takano, "Variational study for the equation of state of asymmetric nuclear matter at finite temperatures," *Nucl. Phys. A*, vol. 902, pp. 53–73, 2013.

[127] J. Carlson, S. Gandolfi, F. Pederiva, S. C. Pieper, R. Schiavilla, K. E. Schmidt, and R. B. Wiringa, "Quantum Monte Carlo methods for nuclear physics," *Rev. Mod. Phys.*, vol. 87, p. 1067, 2015.

[128] H. Müther, F. Sammarruca, and Z. Ma, "Relativistic Effects and Three-Nucleon Forces in Nuclear Matter and Nuclei," *Int. J. Mod. Phys. E*, vol. 26, p. 173001, 2017.

[129] K. Hebeler, J. D. Holt, J. Menendez, and A. Schwenk, "Nuclear forces and their impact on neutron-rich nuclei and neutron-rich matter," *Ann. Rev. Nucl. Part. Sci.*, vol. 65, pp. 457–484, 2015.

[130] E. Epelbaum, H. Krebs, and P. Reinert, "High-precision nuclear forces from chiral EFT: State-of-the-art, challenges and outlook," *Front. in Phys.*, vol. 8, p. 98, 2020.

[131] C. Drischler, J. W. Holt, and C. Wellenhofer, "Chiral Effective Field Theory and the High-Density Nuclear Equation of State," *Ann. Rev. Nucl. Part. Sci.*, vol. 71, pp. 403–432, 2021.

[132] E. Epelbaum, H. Krebs, and U. G. Meißner, "Improved chiral nucleon-nucleon potential up to next-to-next-to-next-to-leading order," *Eur. Phys. J. A*, vol. 51, no. 5, p. 53, 2015.

[133] J. S. Read, B. D. Lackey, B. J. Owen, and J. L. Friedman, "Constraints on a phenomenologically parameterized neutron-star equation of state," *Phys. Rev. D*, vol. 79, p. 124032, 2009.

[134] M. G. Alford and S. Han, "Generic Conditions for Stable Hybrid Stars," *EPJ Web Conf.*, vol. 80, p. 00038, 2014.

[135] R. C. Tolman, "Static solutions of Einstein's field equations for spheres of fluid," *Phys. Rev.*, vol. 55, pp. 364–373, 1939.

[136] J. R. Oppenheimer and G. M. Volkoff, "On massive neutron cores," *Phys. Rev.*, vol. 55, pp. 374–381, 1939.

[137] J. M. Weisberg and J. H. Taylor, "Relativistic binary pulsar B1913+16: Thirty years of observations and analysis," *ASP Conf. Ser.*, vol. 328, p. 25, 2005.

[138] P. Demorest, T. Pennucci, S. Ransom, M. Roberts, and J. Hessels, "Shapiro Delay Measurement of A Two Solar Mass Neutron Star," *Nature*, vol. 467, pp. 1081–1083, 2010.

[139] J. Antoniadis *et al.*, "A Massive Pulsar in a Compact Relativistic Binary," *Science*, vol. 340, p. 6131, 2013.

[140] E. Fonseca *et al.*, "Refined Mass and Geometric Measurements of the High-mass PSR J0740+6620," *Astrophys. J. Lett.*, vol. 915, no. 1, p. L12, 2021.

[141] J. M. Lattimer and A. W. Steiner, "Neutron Star Masses and Radii from Quiescent Low-Mass X-ray Binaries," *Astrophys. J.*, vol. 784, p. 123, 2014.

[142] S. Guillot and R. E. Rutledge, "Rejecting proposed dense-matter equations of state with quiescent low-mass X-ray binaries," *Astrophys. J. Lett.*, vol. 796, no. 1, p. L3, 2014.

[143] T. E. Riley *et al.*, "A $NICER$ View of PSR J0030+0451: Millisecond Pulsar Parameter Estimation," *Astrophys. J. Lett.*, vol. 887, no. 1, p. L21, 2019.

[144] M. C. Miller *et al.*, "PSR J0030+0451 Mass and Radius from $NICER$ Data and Implications for the Properties of Neutron Star Matter," *Astrophys. J. Lett.*, vol. 887, no. 1, p. L24, 2019.

[145] T. E. Riley *et al.*, "A NICER View of the Massive Pulsar PSR J0740+6620 Informed by Radio Timing and XMM-Newton Spectroscopy," *Astrophys. J. Lett.*, vol. 918, no. 2, p. L27, 2021.

[146] M. C. Miller *et al.*, "The Radius of PSR J0740+6620 from NICER and XMM-Newton Data," *Astrophys. J. Lett.*, vol. 918, no. 2, p. L28, 2021.

[147] S. Vinciguerra *et al.*, "An updated mass-radius analysis of the 2017-2018 NICER data set of PSR J0030+0451," *arXiv e-prints*, p. arXiv:2308.09469, 2023.

[148] N. K. Glendenning, *Neutron Stars*, pp. 180–246. New York, NY: Springer US, 1997.

[149] R. W. Romani, D. Kandel, A. V. Filippenko, T. G. Brink, and W. Zheng, "PSR J0952−0607: The Fastest and Heaviest Known Galactic Neutron Star," *Astrophys. J. Lett.*, vol. 934, no. 2, p. L17, 2022.

[150] B. P. Abbott *et al.*, "GW170817: Measurements of neutron star radii and equation of state," *Phys. Rev. Lett.*, vol. 121, no. 16, p. 161101, 2018.

[151] B. Margalit and B. D. Metzger, "Constraining the Maximum Mass of Neutron Stars From Multi-Messenger Observations of GW170817," *Astrophys. J. Lett.*, vol. 850, no. 2, p. L19, 2017.

[152] A. Bauswein, O. Just, H.-T. Janka, and N. Stergioulas, "Neutron-star radius constraints from GW170817 and future detections," *Astrophys. J. Lett.*, vol. 850, no. 2, p. L34, 2017.

[153] M. Shibata, S. Fujibayashi, K. Hotokezaka, K. Kiuchi, K. Kyutoku, Y. Sekiguchi, and M. Tanaka, "Modeling GW170817 based on numerical relativity and its implications," *Phys. Rev. D*, vol. 96, no. 12, p. 123012, 2017.

[154] M. Ruiz, S. L. Shapiro, and A. Tsokaros, "GW170817, General Relativistic Magnetohydrodynamic Simulations, and the Neutron Star Maximum Mass," *Phys. Rev. D*, vol. 97, no. 2, p. 021501, 2018.

[155] D. Radice, A. Perego, F. Zappa, and S. Bernuzzi, "GW170817: Joint Constraint on the Neutron Star Equation of State from Multimessenger Observations," *Astrophys. J. Lett.*, vol. 852, no. 2, p. L29, 2018.

[156] L. Rezzolla, E. R. Most, and L. R. Weih, "Using gravitational-wave observations and quasi-universal relations to constrain the maximum mass of neutron stars," *Astrophys. J. Lett.*, vol. 852, no. 2, p. L25, 2018.

[157] D. Radice and L. Dai, "Multimessenger Parameter Estimation of GW170817," *Eur. Phys. J. A*, vol. 55, no. 4, p. 50, 2019.

[158] M. W. Coughlin, T. Dietrich, B. Margalit, and B. D. Metzger, "Multimessenger Bayesian parameter inference of a binary neutron star merger," *Mon. Not. Roy. Astron. Soc.*, vol. 489, no. 1, pp. L91–L96, 2019.

[159] M. Breschi, A. Perego, S. Bernuzzi, W. Del Pozzo, V. Nedora, D. Radice, and D. Vescovi, "AT2017gfo: Bayesian inference and model selection of multicomponent kilonovae and constraints on the neutron star equation of state," *Mon. Not. Roy. Astron. Soc.*, vol. 505, no. 2, pp. 1661–1677, 2021.

[160] M. Prakash, M. Prakash, J. M. Lattimer, and C. J. Pethick, "Rapid cooling of neutron stars by hyperons and Delta isobars," *Astrophys. J. Lett.*, vol. 390, p. L77, 1992.

[161] D. Page, M. Prakash, J. M. Lattimer, and A. Steiner, "Prospects of detecting baryon and quark superfluidity from cooling neutron stars," *Phys. Rev. Lett.*, vol. 85, pp. 2048–2051, 2000.

[162] D. Page, J. M. Lattimer, M. Prakash, and A. W. Steiner, "Minimal cooling of neutron stars: A New paradigm," *Astrophys. J. Suppl.*, vol. 155, pp. 623–650, 2004.

[163] D. G. Yakovlev and C. J. Pethick, "Neutron star cooling," *Ann. Rev. Astron. Astrophys.*, vol. 42, pp. 169–210, 2004.

[164] E. P. Liang, "Gamma-Ray Burst Annihilation Lines and Neutron Star Structure," *Astrophys. J.*, vol. 304, p. 682, 1986.

[165] C. Fuchs, A. Faessler, E. Zabrodin, and Y.-M. Zheng, "Probing the nuclear equation of state by K+ production in heavy ion collisions," *Phys. Rev. Lett.*, vol. 86, pp. 1974–1977, 2001.

[166] P. Danielewicz, R. Lacey, and W. G. Lynch, "Determination of the equation of state of dense matter," *Science*, vol. 298, pp. 1592–1596, 2002.

[167] J. Piekarewicz, "Unmasking the nuclear matter equation of state," *Phys. Rev. C*, vol. 69, p. 041301, 2004.

[168] E. Khan and J. Margueron, "Constraining the nuclear equation of state at subsaturation densities," *Phys. Rev. Lett.*, vol. 109, p. 092501, 2012.

[169] M. Oertel, C. Providência, F. Gulminelli, and A. R. Raduta, "Hyperons in neutron star matter within relativistic mean-field models," *J. Phys. G*, vol. 42, no. 7, p. 075202, 2015.

[170] A. Andronic, P. Braun-Munzinger, K. Redlich, and J. Stachel, "Hadron yields, the chemical freeze-out and the QCD phase diagram," *J. Phys. Conf. Ser.*, vol. 779, no. 1, p. 012012, 2017.

[171] B. T. Reed, F. J. Fattoyev, C. J. Horowitz, and J. Piekarewicz, "Implications of PREX-2 on the Equation of State of Neutron-Rich Matter," *Phys. Rev. Lett.*, vol. 126, no. 17, p. 172503, 2021.

[172] R. Kumar *et al.*, "Theoretical and Experimental Constraints for the Equation of State of Dense and Hot Matter," *arXiv e-prints*, p. arXiv:2303.17021, 2023.

[173] K. Aamodt *et al.*, "The ALICE experiment at the CERN LHC," *JINST*, vol. 3, p. S08002, 2008.

[174] J. Adamczewski-Musch *et al.*, "Probing dense baryon-rich matter with virtual photons," *Nature Phys.*, vol. 15, no. 10, pp. 1040–1045, 2019.

[175] B. A. Mecking *et al.*, "The CEBAF Large Acceptance Spectrometer (CLAS)," *Nucl. Instrum. Meth. A*, vol. 503, pp. 513–553, 2003.

[176] K. Agari *et al.*, "Secondary charged beam lines at the J-PARC hadron experimental hall," *PTEP*, vol. 2012, p. 02B009, 2012.

[177] B. Friman, C. Hohne, J. Knoll, S. Leupold, J. Randrup, R. Rapp, and P. Senger, eds., *The CBM physics book: Compressed baryonic matter in laboratory experiments*, vol. 814 of *Lecture Notes in Physics*. Berlin, Heidelberg: Springer Berlin Heidelberg, 2011.

[178] P. Senger, "Probing Dense Nuclear Matter in the Laboratory: Experiments at FAIR and NICA," *Universe*, vol. 7, no. 6, p. 171, 2021.

[179] M. Durante *et al.*, "All the fun of the FAIR: fundamental physics at the facility for antiproton and ion research," *Phys. Scripta*, vol. 94, no. 3, p. 033001, 2019.

[180] D. Blaschke, J. Aichelin, E. Bratkovskaya, V. Friese, M. Gazdzicki, J. Randrup, O. Rogachevsky, O. Teryaev, and V. Toneev, "Topical issue on Exploring Strongly Interacting Matter at High Densities - NICA White Paper," *European Physical Journal A*, vol. 52, no. 8, p. 267, 2016.

[181] V. Abgaryan *et al.*, "Status and initial physics performance studies of the MPD experiment at NICA," *Eur. Phys. J. A*, vol. 58, no. 7, p. 140, 2022.

[182] O. Komoltsev and A. Kurkela, "How Perturbative QCD Constrains the Equation of State at Neutron-Star Densities," *Phys. Rev. Lett.*, vol. 128, no. 20, p. 202701, 2022.

[183] T. Gorda, O. Komoltsev, and A. Kurkela, "Ab-initio QCD Calculations Impact the Inference of the Neutron-star-matter Equation of State," *Astrophys. J.*, vol. 950, no. 2, p. 107, 2023.

[184] O. Komoltsev, R. Somasundaram, T. Gorda, A. Kurkela, J. Margueron, and I. Tews, "Equation of state at neutron-star densities and beyond from perturbative QCD," *arXiv e-prints*, p. arXiv:2312.14127, 2023.

[185] C. D. Capano, I. Tews, S. M. Brown, B. Margalit, S. De, S. Kumar, D. A. Brown, B. Krishnan, and S. Reddy, "Stringent constraints on neutron-star radii from multimessenger observations and nuclear theory," *Nature Astron.*, vol. 4, no. 6, pp. 625–632, 2020.

[186] T. Dietrich, M. W. Coughlin, P. T. H. Pang, M. Bulla, J. Heinzel, L. Issa, I. Tews, and S. Antier, "Multimessenger constraints on the neutron-star equation of state and the Hubble constant," *Science*, vol. 370, no. 6523, pp. 1450–1453, 2020.

[187] M. Al-Mamun, A. W. Steiner, J. Nättilä, J. Lange, R. O'Shaughnessy, I. Tews, S. Gandolfi, C. Heinke, and S. Han, "Combining Electromagnetic and Gravitational-Wave Constraints on Neutron-Star Masses and Radii," *Phys. Rev. Lett.*, vol. 126, no. 6, p. 061101, 2021.

[188] G. Raaijmakers, S. K. Greif, K. Hebeler, T. Hinderer, S. Nissanke, A. Schwenk, T. E. Riley, A. L. Watts, J. M. Lattimer, and W. C. G. Ho, "Constraints on the Dense Matter Equation of State and Neutron Star Properties from NICER's Mass–Radius Estimate of PSR J0740+6620 and Multimessenger Observations," *Astrophys. J. Lett.*, vol. 918, no. 2, p. L29, 2021.

[189] S. Huth *et al.*, "Constraining Neutron-Star Matter with Microscopic and Macroscopic Collisions," *Nature*, vol. 606, pp. 276–280, 2022.

[190] S. Soma, L. Wang, S. Shi, H. Stöcker, and K. Zhou, "Reconstructing the neutron star equation of state from observational data via automatic differentiation," *Phys. Rev. D*, vol. 107, no. 8, p. 083028, 2023.

[191] T. Malik and C. Providência, "Bayesian inference of signatures of hyperons inside neutron stars," *Phys. Rev. D*, vol. 106, no. 6, p. 063024, 2022.

[192] P. T. H. Pang *et al.*, "An updated nuclear-physics and multi-messenger astrophysics framework for binary neutron star mergers," *Nature Commun.*, vol. 14, no. 1, p. 8352, 2023.

[193] C. Huang, G. Raaijmakers, A. L. Watts, L. Tolos, and C. Providência, "Constraining fundamental nuclear physics parameters using neutron star mass-radius measurements I: Nucleonic models," *arXiv e-prints*, p. arXiv:2303.17518, 2023.

[194] L. Tolos and L. Fabbietti, "Strangeness in Nuclei and Neutron Stars," *Prog. Part. Nucl. Phys.*, vol. 112, p. 103770, 2020.

[195] H. J. Schulze, A. Polls, A. Ramos, and I. Vidana, "Maximum mass of neutron stars," *Phys. Rev. C*, vol. 73, p. 058801, 2006.

[196] H. J. Schulze and T. Rijken, "Maximum mass of hyperon stars with the Nijmegen ES C-08 model," *Phys. Rev. C*, vol. 84, p. 035801, 2011.

[197] D. Chatterjee and I. Vidaña, "Do hyperons exist in the interior of neutron stars?," *Eur. Phys. J. A*, vol. 52, no. 2, p. 29, 2016.

[198] D. Logoteta, I. Vidana, and I. Bombaci, "Impact of chiral hyperonic three-body forces on neutron stars," *Eur. Phys. J. A*, vol. 55, no. 11, p. 207, 2019.

[199] D. Gerstung, N. Kaiser, and W. Weise, "Hyperon–nucleon three-body forces and strangeness in neutron stars," *Eur. Phys. J. A*, vol. 56, no. 6, p. 175, 2020.

[200] R. Wirth, D. Gazda, P. Navrátil, and R. Roth, "Hypernuclear No-Core Shell Model," *Phys. Rev. C*, vol. 97, no. 6, p. 064315, 2018.

[201] R. Wirth and R. Roth, "Similarity renormalization group evolution of hypernuclear Hamiltonians," *Phys. Rev. C*, vol. 100, no. 4, p. 044313, 2019.

[202] S. Petschauer, J. Haidenbauer, N. Kaiser, U.-G. Meißner, and W. Weise, "Hyperon-nuclear interactions from SU(3) chiral effective field theory," *Front. in Phys.*, vol. 8, p. 12, 2020.

[203] H. Le, J. Haidenbauer, U.-G. Meißner, and A. Nogga, "Jacobi no-core shell model for p-shell hypernuclei," *Eur. Phys. J. A*, vol. 56, no. 12, p. 301, 2020.

[204] H. Le, J. Haidenbauer, U.-G. Meißner, and A. Nogga, "Ab initio calculation of charge-symmetry breaking in A=7 and 8 Λ hypernuclei," *Phys. Rev. C*, vol. 107, no. 2, p. 024002, 2023.

[205] J. Haidenbauer, U.-G. Meißner, A. Nogga, and H. Le, "Hyperon–nucleon interaction in chiral effective field theory at next-to-next-to-leading order," *Eur. Phys. J. A*, vol. 59, no. 3, p. 63, 2023.

[206] B. D. Lackey, M. Nayyar, and B. J. Owen, "Observational constraints on hyperons in neutron stars," *Phys. Rev. D*, vol. 73, p. 024021, 2006.

[207] S. Banik, M. Hempel, and D. Bandyopadhyay, "New Hyperon Equations of State for Supernovae and Neutron Stars in Density-dependent Hadron Field Theory," *Astrophys. J. Suppl.*, vol. 214, no. 2, p. 22, 2014.

[208] M. Marques, M. Oertel, M. Hempel, and J. Novak, "New temperature dependent hyperonic equation of state: Application to rotating neutron star models and I-Q relations," *Phys. Rev. C*, vol. 96, no. 4, p. 045806, 2017.

[209] M. Fortin, M. Oertel, and C. Providência, "Hyperons in hot dense matter: what do the constraints tell us for equation of state?," *Publ. Astron. Soc. Austral.*, vol. 35, p. 44, 2018.

[210] J. R. Stone, V. Dexheimer, P. A. M. Guichon, A. W. Thomas, and S. Typel, "Equation of state of hot dense hyperonic matter in the Quark–Meson-Coupling (QMC-A) model," *Mon. Not. Roy. Astron. Soc.*, vol. 502, no. 3, pp. 3476–3490, 2021.

[211] H. Kochankovski, A. Ramos, and L. Tolos, "Equation of state for hot hyperonic neutron star matter," *Mon. Not. Roy. Astron. Soc.*, vol. 517, no. 1, pp. 507–517, 2022. [Erratum: Mon.Not.Roy.Astron.Soc. 518, 6376].

[212] A. R. Raduta, "Equations of state for hot neutron stars-II. The role of exotic particle degrees of freedom," *Eur. Phys. J. A*, vol. 58, no. 6, p. 115, 2022.

[213] C. Rappold *et al.*, "Hypernuclear spectroscopy of products from 6Li projectiles on a carbon target at 2 AGeV," *Nucl. Phys. A*, vol. 913, pp. 170–184, 2013.

[214] H. Tamura *et al.*, "Gamma-ray spectroscopy of hypernuclei - present and future," *Nucl. Phys. A*, vol. 914, pp. 99–108, 2013.

[215] A. Feliciello and T. Nagae, "Experimental review of hypernuclear physics: recent achievements and future perspectives," *Rept. Prog. Phys.*, vol. 78, no. 9, p. 096301, 2015.

[216] A. Gal, E. V. Hungerford, and D. J. Millener, "Strangeness in nuclear physics," *Rev. Mod. Phys.*, vol. 88, no. 3, p. 035004, 2016.

[217] E. Friedman and A. Gal, "Λ hypernuclear potentials beyond linear density dependence," *Nucl. Phys. A*, vol. 1039, p. 122725, 2023.

[218] R. Engelmann, H. Filthuth, V. Hepp, and E. Kluge, "Inelastic Σ^-p-interactions at low momenta ," *Phys. Lett.*, vol. 21, no. 5, pp. 587–589, 1966.

[219] J. Rowley *et al.*, "Improved Λp Elastic Scattering Cross Sections Between 0.9 and 2.0 GeV/c and Connections to the Neutron Star Equation of State," *Phys. Rev. Lett.*, vol. 127, no. 27, p. 272303, 2021.

[220] K. Miwa *et al.*, "Measurement of the differential cross sections of the $\Sigma^- p$ elastic scattering in momentum range 470 to 850 MeV/c," *Phys. Rev. C*, vol. 104, no. 4, p. 045204, 2021.

[221] K. Miwa *et al.*, "Precise measurement of differential cross sections of the $\Sigma^- p \to \Lambda n$ reaction in momentum range 470-650 MeV/c," *Phys. Rev. Lett.*, vol. 128, no. 7, p. 072501, 2022.

[222] T. Nanamura *et al.*, "Measurement of differential cross sections for Σ+p elastic scattering in the momentum range 0.44–0.80 GeV/c," *PTEP*, vol. 2022, no. 9, p. 093D01, 2022.

[223] J. Adamczewski-Musch *et al.*, "The $\boldsymbol{\Lambda p}$ interaction studied via femtoscopy in p + Nb reactions at $\sqrt{s_{NN}} = \mathbf{3.18\ GeV}$," *Phys. Rev. C*, vol. 94, no. 2, p. 025201, 2016.

[224] S. Acharya *et al.*, "p-p, p-Λ and Λ-Λ correlations studied via femtoscopy in pp reactions at $\sqrt{s} = 7$ TeV," *Phys. Rev. C*, vol. 99, no. 2, p. 024001, 2019.

[225] S. Acharya *et al.*, "Study of the Λ-Λ interaction with femtoscopy correlations in pp and p-Pb collisions at the LHC," *Phys. Lett. B*, vol. 797, p. 134822, 2019.

[226] S. Acharya *et al.*, "Investigation of the p–Σ0 interaction via femtoscopy in pp collisions," *Phys. Lett. B*, vol. 805, p. 135419, 2020.

[227] S. Acharya *et al.*, "First Observation of an Attractive Interaction between a Proton and a Cascade Baryon," *Phys. Rev. Lett.*, vol. 123, no. 11, p. 112002, 2019.

[228] S. Acharya *et al.*, "Exploring the NΛ–NΣ coupled system with high precision correlation techniques at the LHC," *Phys. Lett. B*, vol. 833, p. 137272, 2022.

[229] S. Acharya *et al.*, "Towards the understanding of the genuine three-body interaction for p–p–p and p–p–Λ," *Eur. Phys. J. A*, vol. 59, no. 7, p. 145, 2023.

[230] T. W. Baumgarte, S. A. Teukolsky, S. L. Shapiro, H. T. Janka, and W. Keil, "Delayed collapse of hot neutron stars to black holes via hadronic phase transitions," *Astrophys. J.*, vol. 468, pp. 823–833, 1996.

[231] K. Sumiyoshi, C. Ishizuka, A. Ohnishi, S. Yamada, and H. Suzuki, "Emergence of hyperons in failed supernovae: trigger of the black hole formation," *Astrophys. J. Lett.*, vol. 690, pp. L43–L46, 2009.

[232] K. Nakazato, S. Furusawa, K. Sumiyoshi, A. Ohnishi, S. Yamada, and H. Suzuki, "Hyperon Matter and Black Hole Formation in Failed Supernovae," *Astrophys. J.*, vol. 745, p. 197, 2012.

[233] B. Peres, M. Oertel, and J. Novak, "Influence of pions and hyperons on stellar black hole formation," *Phys. Rev. D*, vol. 87, no. 4, p. 043006, 2013.

[234] S. Banik, "Probing the metastability of a protoneutron star with hyperons in a core-collapse supernova," *Phys. Rev. C*, vol. 89, no. 3, p. 035807, 2014.

[235] A. R. Raduta, A. Sedrakian, and F. Weber, "Cooling of hypernuclear compact stars," *Mon. Not. Roy. Astron. Soc.*, vol. 475, no. 4, pp. 4347–4356, 2018.

[236] H. Grigorian, D. N. Voskresensky, and K. A. Maslov, "Cooling of neutron stars in "nuclear medium cooling scenario" with stiff equation of state including hyperons," *Nucl. Phys. A*, vol. 980, pp. 105–130, 2018.

[237] R. Negreiros, L. Tolos, M. Centelles, A. Ramos, and V. Dexheimer, "Cooling of Small and Massive Hyperonic Stars," *Astrophys. J.*, vol. 863, no. 1, p. 104, 2018.

[238] A. R. Raduta, J. J. Li, A. Sedrakian, and F. Weber, "Cooling of hypernuclear compact stars: Hartree–Fock models and high-density pairing," *Mon. Not. Roy. Astron. Soc.*, vol. 487, no. 2, pp. 2639–2652, 2019.

[239] M. Fortin, A. R. Raduta, S. Avancini, and C. Providência, "Thermal evolution of relativistic hyperonic compact stars with calibrated equations of state," *Phys. Rev. D*, vol. 103, no. 8, p. 083004, 2021.

[240] A. Bazavov *et al.*, "Chiral crossover in QCD at zero and non-zero chemical potentials," *Phys. Lett. B*, vol. 795, pp. 15–21, 2019.

[241] Y. Nambu and G. Jona-Lasinio, "Dynamical Model of Elementary Particles Based on an Analogy with Superconductivity. 1.," *Phys. Rev.*, vol. 122, pp. 345–358, 1961.

[242] P. Hasenfratz and J. Kuti, "The Quark Bag Model," *Phys. Rept.*, vol. 40, pp. 75–179, 1978.

[243] S. P. Klevansky, "The Nambu-Jona-Lasinio model of quantum chromodynamics," *Rev. Mod. Phys.*, vol. 64, pp. 649–708, 1992.

[244] M. Buballa, "NJL model analysis of quark matter at large density," *Phys. Rept.*, vol. 407, pp. 205–376, 2005.

[245] C. S. Fischer, J. Luecker, and C. A. Welzbacher, "Phase structure of three and four flavor QCD," *Phys. Rev. D*, vol. 90, no. 3, p. 034022, 2014.

[246] F. Gao and J. M. Pawlowski, "QCD phase structure from functional methods," *Phys. Rev. D*, vol. 102, no. 3, p. 034027, 2020.

[247] P. Braun-Munzinger and J. Wambach, "The Phase Diagram of Strongly-Interacting Matter," *Rev. Mod. Phys.*, vol. 81, pp. 1031–1050, 2009.

[248] K. Fukushima and T. Hatsuda, "The phase diagram of dense QCD," *Rept. Prog. Phys.*, vol. 74, p. 014001, 2011.

[249] E. Witten, "Cosmic Separation of Phases," *Phys. Rev. D*, vol. 30, pp. 272–285, 1984.

[250] E. Farhi and R. L. Jaffe, "Strange Matter," *Phys. Rev. D*, vol. 30, p. 2379, 1984.

[251] C. Alcock, E. Farhi, and A. Olinto, "Strange stars," *Astrophys. J.*, vol. 310, pp. 261–272, 1986.

[252] N. K. Glendenning, "First order phase transitions with more than one conserved charge: Consequences for neutron stars," *Phys. Rev. D*, vol. 46, pp. 1274–1287, 1992.

[253] M. Hempel, G. Pagliara, and J. Schaffner-Bielich, "Conditions for Phase Equilibrium in Supernovae, Proto-Neutron and Neutron Stars," *Phys. Rev. D*, vol. 80, p. 125014, 2009.

[254] M. Hempel, V. Dexheimer, S. Schramm, and I. Iosilevskiy, "Noncongruence of the nuclear liquid-gas and deconfinement phase transitions," *Phys. Rev. C*, vol. 88, no. 1, p. 014906, 2013.

[255] C. Constantinou, T. Zhao, S. Han, and M. Prakash, "Framework for phase transitions between the Maxwell and Gibbs constructions," *Phys. Rev. D*, vol. 107, no. 7, p. 074013, 2023.

[256] K. Schertler, C. Greiner, J. Schaffner-Bielich, and M. H. Thoma, "Quark phases in neutron stars and a 'third family' of compact stars as a signature for phase transitions," *Nucl. Phys. A*, vol. 677, pp. 463–490, 2000.

[257] C. Gocke, D. Blaschke, A. Khalatyan, and H. Grigorian, "Equation of state for strange quark matter in a separable model," in *Workshop on Quark Matter in Astrophysics and Particle Physics*, (Rostock), pp. 171–182, Rostock University Press, 2001.

[258] G. F. Burgio, M. Baldo, P. K. Sahu, and H. J. Schulze, "The Hadron quark phase transition in dense matter and neutron stars," *Phys. Rev. C*, vol. 66, p. 025802, 2002.

[259] S. Banik and D. Bandyopadhyay, "Color superconducting quark matter core in the third family of compact stars," *Phys. Rev. D*, vol. 67, p. 123003, 2003.

[260] C. Maieron, M. Baldo, G. F. Burgio, and H. J. Schulze, "Hybrid stars with the color dielectric and the MIT bag models," *Phys. Rev. D*, vol. 70, p. 043010, 2004.

[261] M. Alford, M. Braby, M. W. Paris, and S. Reddy, "Hybrid stars that masquerade as neutron stars," *Astrophys. J.*, vol. 629, pp. 969–978, 2005.

[262] T. Kojo, P. D. Powell, Y. Song, and G. Baym, "Phenomenological QCD equation of state for massive neutron stars," *Phys. Rev. D*, vol. 91, no. 4, p. 045003, 2015.

[263] S. Benic, D. Blaschke, D. E. Alvarez-Castillo, T. Fischer, and S. Typel, "A new quark-hadron hybrid equation of state for astrophysics - I. High-mass twin compact stars," *Astron. Astrophys.*, vol. 577, p. A40, 2015.

[264] M. G. Alford and A. Sedrakian, "Compact stars with sequential QCD phase transitions," *Phys. Rev. Lett.*, vol. 119, no. 16, p. 161104, 2017.

[265] G. Baym, S. Furusawa, T. Hatsuda, T. Kojo, and H. Togashi, "New Neutron Star Equation of State with Quark-Hadron Crossover," *Astrophys. J.*, vol. 885, p. 42, 2019.

[266] D. Blaschke, H. Grigorian, and G. Röpke, "Chirally improved quark Pauli blocking in nuclear matter and applications to quark deconfinement in neutron stars," *Particles*, vol. 3, no. 2, pp. 477–499, 2020.

[267] K. Otto, M. Oertel, and B.-J. Schaefer, "Nonperturbative quark matter equations of state with vector interactions," *Eur. Phys. J. ST*, vol. 229, no. 22-23, pp. 3629–3649, 2020.

[268] N. Jokela, M. Järvinen, G. Nijs, and J. Remes, "Unified weak and strong coupling framework for nuclear matter and neutron stars," *Phys. Rev. D*, vol. 103, no. 8, p. 086004, 2021.

[269] C. Xia, Z. Zhu, X. Zhou, and A. Li, "Sound velocity in dense stellar matter with strangeness and compact stars," *Chin. Phys. C*, vol. 45, no. 5, p. 055104, 2021.

[270] T. Kojo, G. Baym, and T. Hatsuda, "Implications of NICER for Neutron Star Matter: The QHC21 Equation of State," *Astrophys. J.*, vol. 934, no. 1, p. 46, 2022.

[271] A. Clevinger, J. Corkish, K. Aryal, and V. Dexheimer, "Hybrid equations of state for neutron stars with hyperons and deltas," *Eur. Phys. J. A*, vol. 58, no. 5, p. 96, 2022.

[272] E. S. Fraga, R. da Mata, S. Pitsinigkos, and A. Schmitt, "Strange quark matter from a baryonic approach," *Phys. Rev. D*, vol. 106, no. 7, p. 074018, 2022.

[273] D. Blaschke, O. Ivanytskyi, and M. Shahrbaf, "Quark deconfinement in compact stars through sexaquark condensation," in *New Phenomena And New States Of Matter In The Universe: From Quarks To Cosmos*, pp. 317–342, Singapore: World Scientific, 2023.

[274] I. Sagert, T. Fischer, M. Hempel, G. Pagliara, J. Schaffner-Bielich, A. Mezzacappa, F. K. Thielemann, and M. Liebendorfer, "Signals of the QCD phase transition in core-collapse supernovae," *Phys. Rev. Lett.*, vol. 102, p. 081101, 2009.

[275] V. A. Dexheimer and S. Schramm, "A Novel Approach to Model Hybrid Stars," *Phys. Rev. C*, vol. 81, p. 045201, 2010.

[276] J. P. Olson, M. Warren, M. Meixner, G. J. Mathews, N. Q. Lan, and H. E. Dalhed, "Generalized density functional equation of state for astrophysical simulations with 3-body forces and quark gluon plasma," *arXiv e-prints*, p. arXiv:1612.08992, 2016.

[277] T. Klahn, T. Fischer, and M. Hempel, "Simultaneous chiral symmetry restoration and deconfinement - Consequences for the QCD phase diagram," *Astrophys. J.*, vol. 836, no. 1, p. 89, 2017.

[278] J. Roark and V. Dexheimer, "Deconfinement phase transition in proto-neutron-star matter," *Phys. Rev. C*, vol. 98, no. 5, p. 055805, 2018.

[279] P. M. Chesler, N. Jokela, A. Loeb, and A. Vuorinen, "Finite-temperature Equations of State for Neutron Star Mergers," *Phys. Rev. D*, vol. 100, no. 6, p. 066027, 2019.

[280] M. Cierniak, T. Fischer, N.-U. Bastian, T. Klähn, and M. Salinas, "Impact of the Nuclear Equation of State on the Stability of Hybrid Neutron Stars," *Universe*, vol. 5, no. 8, p. 186, 2019.

[281] G. Malfatti, M. G. Orsaria, G. A. Contrera, F. Weber, and I. F. Ranea-Sandoval, "Hot quark matter and (proto-) neutron stars," *Phys. Rev. C*, vol. 100, no. 1, p. 015803, 2019.

[282] A. Motornenko, J. Steinheimer, V. Vovchenko, S. Schramm, and H. Stoecker, "Equation of state for hot QCD and compact stars from a mean field approach," *Phys. Rev. C*, vol. 101, no. 3, p. 034904, 2020.

[283] N.-U. F. Bastian, "Phenomenological quark-hadron equations of state with first-order phase transitions for astrophysical applications," *Phys. Rev. D*, vol. 103, no. 2, p. 023001, 2021.

[284] T. Demircik, C. Ecker, and M. Järvinen, "Dense and Hot QCD at Strong Coupling," *Phys. Rev. X*, vol. 12, no. 4, p. 041012, 2022.

[285] A. Prakash, D. Radice, D. Logoteta, A. Perego, V. Nedora, I. Bombaci, R. Kashyap, S. Bernuzzi, and A. Endrizzi, "Signatures of deconfined quark phases in binary neutron star mergers," *Phys. Rev. D*, vol. 104, no. 8, p. 083029, 2021.

[286] O. Ivanytskyi and D. Blaschke, "A new class of hybrid EoS with multiple critical endpoints for simulations of supernovae, neutron stars and their mergers," *Eur. Phys. J. A*, vol. 58, no. 8, p. 152, 2022.

[287] W. Busza, K. Rajagopal, and W. van der Schee, "Heavy Ion Collisions: The Big Picture, and the Big Questions," *Ann. Rev. Nucl. Part. Sci.*, vol. 68, pp. 339–376, 2018.

[288] N. A. Gentile, M. B. Aufderheide, G. J. Mathews, F. D. Swesty, and G. M. Fuller, "The QCD phase transition and supernova core collapse," *Astrophys. J.*, vol. 414, pp. 701–711, 1993.

[289] T. Fischer, N.-U. F. Bastian, M.-R. Wu, P. Baklanov, E. Sorokina, S. Blinnikov, S. Typel, T. Klähn, and D. B. Blaschke, "Quark deconfinement as a supernova explosion engine for massive blue supergiant stars," *Nature Astron.*, vol. 2, no. 12, pp. 980–986, 2018.

[290] P. Jakobus, B. Mueller, A. Heger, A. Motornenko, J. Steinheimer, and H. Stoecker, "The role of the hadron-quark phase transition in core-collapse supernovae," *Mon. Not. Roy. Astron. Soc.*, vol. 516, no. 2, pp. 2554–2574, 2022.

[291] S. Zha, E. P. O'Connor, and A. da Silva Schneider, "Progenitor Dependence of Hadron-quark Phase Transition in Failing Core-collapse Supernovae," *Astrophys. J.*, vol. 911, no. 2, p. 74, 2021.

[292] N. K. Largani, T. Fischer, and N. U. F. Bastian, "Constraining the onset density for the QCD phase transition with the neutrino signal from core-collapse supernovae," *arXiv e-prints*, p. arXiv:2304.12316, 2023.

[293] S. Han, M. A. A. Mamun, S. Lalit, C. Constantinou, and M. Prakash, "Treating quarks within neutron stars," *Phys. Rev. D*, vol. 100, no. 10, p. 103022, 2019.

[294] E. Annala, T. Gorda, A. Kurkela, J. Nättilä, and A. Vuorinen, "Evidence for quark-matter cores in massive neutron stars," *Nature Phys.*, vol. 16, no. 9, pp. 907–910, 2020.

[295] K. Chatziioannou and S. Han, "Studying strong phase transitions in neutron stars with gravitational waves," *Phys. Rev. D*, vol. 101, no. 4, p. 044019, 2020.

[296] T. Gorda, K. Hebeler, A. Kurkela, A. Schwenk, and A. Vuorinen, "Constraints on Strong Phase Transitions in Neutron Stars," *Astrophys. J.*, vol. 955, no. 2, p. 100, 2023.

[297] L. Brandes, W. Weise, and N. Kaiser, "Evidence against a strong first-order phase transition in neutron star cores: Impact of new data," *Phys. Rev. D*, vol. 108, no. 9, p. 094014, 2023.

[298] J.-E. Christian, J. Schaffner-Bielich, and S. Rosswog, "Which first order phase transitions to quark matter are possible in neutron stars?," *arXiv e-prints*, p. arXiv:2312.10148, 2023.

[299] L. Brandes and W. Weise, "Constraints on Phase Transitions in Neutron Star Matter," *arXiv e-prints*, p. arXiv:2312.11937, 2023.

[300] M. G. Alford, S. Han, and M. Prakash, "Generic conditions for stable hybrid stars," *Phys. Rev. D*, vol. 88, no. 8, p. 083013, 2013.

[301] M. Camenzind, *Gravity of Compact Objects*, pp. 27–103. Berlin, Heidelberg: Springer Berlin Heidelberg, 2007.

[302] M. Alcubierre, *Introduction to 3+1 Numerical Relativity*. Oxford: Oxford University Press, 2008.

[303] J. A. Font, "Numerical Hydrodynamics and Magnetohydrodynamics in General Relativity," *Living Rev. Rel.*, vol. 11, p. 7, 2008.

[304] T. Baumgarte and S. Shapiro, *Numerical Relativity: Solving Einstein's Equations on the Computer*. Cambridge: Cambridge University Press, 2010.

[305] L. Rezzolla and O. Zanotti, *Relativistic hydrodynamics*. Oxford: Oxford University Press, 2013.

[306] S. Rosswog, "SPH Methods in the Modelling of Compact Objects," *Living Reviews in Computational Astrophysics*, vol. 1, p. 1, Oct. 2015.

[307] L. Baiotti and L. Rezzolla, "Binary neutron star mergers: a review of Einstein's richest laboratory," *Rept. Prog. Phys.*, vol. 80, no. 9, p. 096901, 2017.

[308] M. D. Duez and Y. Zlochower, "Numerical Relativity of Compact Binaries in the 21st Century," *Rept. Prog. Phys.*, vol. 82, no. 1, p. 016902, 2019.

[309] F. Foucart, P. Laguna, G. Lovelace, D. Radice, and H. Witek, "Snowmass2021 Cosmic Frontier White Paper: Numerical relativity for next-generation gravitational-wave probes of fundamental physics," *arXiv e-prints*, p. arXiv:2203.08139, 2022.

[310] T. Nakamura, K. Oohara, and Y. Kojima, "General Relativistic Collapse to Black Holes and Gravitational Waves from Black Holes," *Prog. Theor. Phys. Suppl.*, vol. 90, pp. 1–218, 1987.

[311] M. Shibata and T. Nakamura, "Evolution of three-dimensional gravitational waves: Harmonic slicing case," *Phys. Rev. D*, vol. 52, pp. 5428–5444, 1995.

[312] T. W. Baumgarte and S. L. Shapiro, "On the numerical integration of Einstein's field equations," *Phys. Rev. D*, vol. 59, p. 024007, 1998.

[313] C. Bona, T. Ledvinka, C. Palenzuela, and M. Zacek, "General covariant evolution formalism for numerical relativity," *Phys. Rev. D*, vol. 67, p. 104005, 2003.

[314] S. Bernuzzi and D. Hilditch, "Constraint violation in free evolution schemes: Comparing BSSNOK with a conformal decomposition of Z4," *Phys. Rev. D*, vol. 81, p. 084003, 2010.

[315] D. Alic, C. Bona-Casas, C. Bona, L. Rezzolla, and C. Palenzuela, "Conformal and covariant formulation of the Z4 system with constraint-violation damping," *Phys. Rev. D*, vol. 85, p. 064040, 2012.

[316] W. E. East, F. Pretorius, and B. C. Stephens, "Hydrodynamics in full general relativity with conservative AMR," *Phys. Rev. D*, vol. 85, p. 124010, 2012.

[317] J. Isenberg and J. Nester, "Canonical Gravity," in *General Relativity and Gravitation. Vol. 1. One hundred years after the birth of Albert Einstein. Edited by A. Held. New York, NY: Plenum Press, p. 23, 1980* (A. Held, ed.), p. 23, 1980.

[318] J. R. Wilson, G. J. Mathews, and P. Marronetti, "Relativistic numerical model for close neutron star binaries," *Phys. Rev. D*, vol. 54, pp. 1317–1331, 1996.

[319] L. R. Weih, M. Hanauske, and L. Rezzolla, "Postmerger Gravitational-Wave Signatures of Phase Transitions in Binary Mergers," *Phys. Rev. Lett.*, vol. 124, no. 17, p. 171103, 2020.

[320] F. Foucart, M. D. Duez, A. Gudinas, F. Hebert, L. E. Kidder, H. P. Pfeiffer, and M. A. Scheel, "Smooth Equations of State for High-Accuracy Simulations of Neutron Star Binaries," *Phys. Rev. D*, vol. 100, no. 10, p. 104048, 2019.

[321] C. Ecker, M. Järvinen, G. Nijs, and W. van der Schee, "Gravitational waves from holographic neutron star mergers," *Phys. Rev. D*, vol. 101, no. 10, p. 103006, 2020.

[322] R. De Pietri, A. Drago, A. Feo, G. Pagliara, M. Pasquali, S. Traversi, and G. Wiktorowicz, "Merger of compact stars in the two-families scenario," *Astrophys. J.*, vol. 881, no. 2, p. 122, 2019.

[323] S. V. Chaurasia, T. Dietrich, M. Ujevic, K. Hendriks, R. Dudi, F. M. Fabbri, W. Tichy, and B. Brügmann, "Gravitational waves and mass ejecta from binary neutron star mergers: Effect of the spin orientation," *Phys. Rev. D*, vol. 102, no. 2, p. 024087, 2020.

[324] A. Bauswein and S. Blacker, "Impact of quark deconfinement in neutron star mergers and hybrid star mergers," *Eur. Phys. J. ST*, vol. 229, no. 22-23, pp. 3595–3604, 2020.

[325] S. L. Liebling, C. Palenzuela, and L. Lehner, "Effects of High Density Phase Transitions on Neutron Star Dynamics," *Class. Quant. Grav.*, vol. 38, no. 11, p. 115007, 2021.

[326] C. Palenzuela, R. Aguilera-Miret, F. Carrasco, R. Ciolfi, J. V. Kalinani, W. Kastaun, B. Miñano, and D. Viganò, "Turbulent magnetic field amplification in binary neutron star mergers," *Phys. Rev. D*, vol. 106, no. 2, p. 023013, 2022.

[327] Y. Fujimoto, K. Fukushima, K. Hotokezaka, and K. Kyutoku, "Gravitational Wave Signal for Quark Matter with Realistic Phase Transition," *Phys. Rev. Lett.*, vol. 130, no. 9, p. 091404, 2023.

[328] Y.-J. Huang, L. Baiotti, T. Kojo, K. Takami, H. Sotani, H. Togashi, T. Hatsuda, S. Nagataki, and Y.-Z. Fan, "Merger and Postmerger of Binary Neutron Stars with a Quark-Hadron Crossover Equation of State," *Phys. Rev. Lett.*, vol. 129, no. 18, p. 181101, 2022.

[329] M. Ujevic, H. Gieg, F. Schianchi, S. V. Chaurasia, I. Tews, and T. Dietrich, "Reverse phase transitions in binary neutron-star systems with exotic-matter cores," *Phys. Rev. D*, vol. 107, no. 2, p. 024025, 2023.

[330] A. Kedia, H. I. Kim, I.-S. Suh, and G. J. Mathews, "Binary neutron star mergers as a probe of quark-hadron crossover equations of state," *Phys. Rev. D*, vol. 106, no. 10, p. 103027, 2022.

[331] L.-J. Guo, W.-C. Yang, Y.-L. Ma, and Y.-L. Wu, "Probing hadron-quark transition through binary neutron star merger," *arXiv e-prints*, p. arXiv:2308.01770, 2023.

[332] A. Kumar, D. Dey, S. Haque, R. Mallick, and S. K. Patra, "Quarkyonic Model for Neutron Star Matter: A Relativistic Mean-Field Approach," *arXiv e-prints*, p. arXiv:2304.08223, 2023.

[333] H. T. Janka, T. Zwerger, and R. Moenchmeyer, "Does artificial viscosity destroy prompt type-II supernova explosions?," *Astron. Astrophys.*, vol. 268, no. 1, pp. 360–368, 1993.

[334] C. A. Raithel, F. Ozel, and D. Psaltis, "Finite-temperature extension for cold neutron star equations of state," *Astrophys. J.*, vol. 875, no. 1, p. 12, 2019.

[335] A. Bauswein, N. Stergioulas, and H. T. Janka, "Revealing the high-density equation of state through binary neutron star mergers," *Phys. Rev. D*, vol. 90, no. 2, p. 023002, 2014.

[336] A. Bauswein, N. Stergioulas, and H.-T. Janka, "Exploring properties of high-density matter through remnants of neutron-star mergers," *Eur. Phys. J. A*, vol. 52, no. 3, p. 56, 2016.

[337] S. Vretinaris, N. Stergioulas, and A. Bauswein, "Empirical relations for gravitational-wave asteroseismology of binary neutron star mergers," *Phys. Rev. D*, vol. 101, no. 8, p. 084039, 2020.

[338] K. Hotokezaka, K. Kyutoku, H. Okawa, M. Shibata, and K. Kiuchi, "Binary Neutron Star Mergers: Dependence on the Nuclear Equation of State," *Phys. Rev. D*, vol. 83, p. 124008, 2011.

[339] T. Dietrich, M. Ujevic, W. Tichy, S. Bernuzzi, and B. Bruegmann, "Gravitational waves and mass ejecta from binary neutron star mergers: Effect of the mass-ratio," *Phys. Rev. D*, vol. 95, no. 2, p. 024029, 2017.

[340] M. Hanauske, K. Takami, L. Bovard, L. Rezzolla, J. A. Font, F. Galeazzi, and H. Stöcker, "Rotational properties of hypermassive neutron stars from binary mergers," *Phys. Rev. D*, vol. 96, no. 4, p. 043004, 2017.

[341] A. Feo, R. De Pietri, F. Maione, and F. Löffler, "Modeling Mergers of Known Galactic Systems of Binary Neutron Stars," *Class. Quant. Grav.*, vol. 34, no. 3, p. 034001, 2017.

[342] C. A. Raithel and V. Paschalidis, "Influence of stellar compactness on finite-temperature effects in neutron star merger simulations," *Phys. Rev. D*, vol. 108, no. 8, p. 083029, 2023.

[343] Y. Sekiguchi, K. Kiuchi, K. Kyutoku, and M. Shibata, "Effects of hyperons in binary neutron star mergers," *Phys. Rev. Lett.*, vol. 107, p. 211101, 2011.

[344] D. Radice, S. Bernuzzi, W. Del Pozzo, L. F. Roberts, and C. D. Ott, "Probing Extreme-Density Matter with Gravitational Wave Observations of Binary Neutron Star Merger Remnants," *Astrophys. J. Lett.*, vol. 842, no. 2, p. L10, 2017.

[345] E. R. Most, L. J. Papenfort, V. Dexheimer, M. Hanauske, S. Schramm, H. Stöcker, and L. Rezzolla, "Signatures of quark-hadron phase transitions in general-relativistic neutron-star mergers," *Phys. Rev. Lett.*, vol. 122, no. 6, p. 061101, 2019.

[346] E. R. Most, L. Jens Papenfort, V. Dexheimer, M. Hanauske, H. Stoecker, and L. Rezzolla, "On the deconfinement phase transition in neutron-star mergers," *Eur. Phys. J. A*, vol. 56, no. 2, p. 59, 2020.

[347] S. Tootle, C. Ecker, K. Topolski, T. Demircik, M. Järvinen, and L. Rezzolla, "Quark formation and phenomenology in binary neutron-star mergers using V-QCD," *SciPost Phys.*, vol. 13, p. 109, 2022.

[348] P. L. Espino, A. Prakash, D. Radice, and D. Logoteta, "Revealing Phase Transition in Dense Matter with Gravitational Wave Spectroscopy of Binary Neutron Star Mergers," *arXiv e-prints*, p. arXiv:2301.03619, 2023.

[349] S. Haque, R. Mallick, and S. K. Thakur, "Effects of onset of phase transition on binary neutron star mergers," *Monthly Notices of the Royal Astronomical Society*, vol. 527, no. 4, pp. 11575–11586, 2023.

[350] A. Prakash, I. Gupta, M. Breschi, R. Kashyap, D. Radice, S. Bernuzzi, D. Logoteta, and B. S. Sathyaprakash, "Detectability of QCD phase transitions in binary neutron star mergers: Bayesian inference with the next generation gravitational wave detectors," *arXiv e-prints*, p. arXiv:2310.06025, 2023.

[351] R. Harada, K. Cannon, K. Hotokezaka, and K. Kyutoku, "On the Testability of the Quark-Hadron Transition Using Gravitational Waves From Merging Binary Neutron Stars," *arXiv e-prints*, p. arXiv:2310.13603, 2023.

[352] C. Raithel, V. Paschalidis, and F. Özel, "Realistic finite-temperature effects in neutron star merger simulations," *Phys. Rev. D*, vol. 104, no. 6, p. 063016, 2021.

[353] J. Fields, A. Prakash, M. Breschi, D. Radice, S. Bernuzzi, and A. da Silva Schneider, "Thermal Effects in Binary Neutron Star Mergers," *Astrophys. J. Lett.*, vol. 952, no. 2, p. L36, 2023.

[354] C. A. Raithel and V. Paschalidis, "Detectability of Finite-Temperature Effects From Neutron Star Mergers with Next-Generation Gravitational Wave Detectors," *arXiv e-prints*, p. arXiv:2312.14046, 2023.

[355] M. Miravet-Tenés, D. Guerra, M. Ruiz, P. Cerdá-Durán, and J. A. Font, "Identifying thermal effects in neutron star merger remnants with model-agnostic waveform reconstructions and third-generation detectors," *arXiv e-prints*, p. arXiv:2401.02493, 2024.

[356] M. Asakawa and K. Yazaki, "Chiral Restoration at Finite Density and Temperature," *Nucl. Phys. A*, vol. 504, pp. 668–684, 1989.

[357] P. de Forcrand and O. Philipsen, "The Chiral critical point of N(f) = 3 QCD at finite density to the order (mu/T)**4," *JHEP*, vol. 11, p. 012, 2008.

[358] O. Philipsen, "Constraining the phase diagram of QCD at finite temperature and density," *PoS*, vol. LATTICE2019, p. 273, 2019.

[359] A. Andronic, P. Braun-Munzinger, and J. Stachel, "Hadron production in central nucleus-nucleus collisions at chemical freeze-out," *Nucl. Phys. A*, vol. 772, pp. 167–199, 2006.

[360] S. Blacker, H. Kochankovski, A. Bauswein, A. Ramos, and L. Tolos, "Thermal behavior as indicator for hyperons in binary neutron star merger remnants," *Phys. Rev. D*, vol. 109, no. 4, p. 043015, 2024.

[361] S. Blacker, A. Bauswein, and S. Typel, "Exploring thermal effects of the hadron-quark matter transition in neutron star mergers," *Phys. Rev. D*, vol. 108, no. 6, p. 063032, 2023.

[362] R. Oechslin, S. Rosswog, and F. K. Thielemann, "Conformally flat smoothed particle hydrodynamics: application to neutron star mergers," *Phys. Rev. D*, vol. 65, p. 103005, 2002.

[363] R. A. Gingold and J. J. Monaghan, "Smoothed particle hydrodynamics: Theory and application to non-spherical stars," *Mon. Not. Roy. Astron. Soc.*, vol. 181, p. 375, 1977.

[364] L. B. Lucy, "A numerical approach to the testing of the fission hypothesis," *Astron. J.*, vol. 82, pp. 1013–1024, 1977.

[365] W. Benz, *Smooth Particle Hydrodynamics: A Review*, pp. 269–288. Dordrecht: Springer Netherlands, 1990.

[366] J. J. Monaghan, "Smoothed particle hydrodynamics," *Ann. Rev. Astron. Astrophys.*, vol. 30, pp. 543–574, 1992.

[367] R. A. Gingold and J. J. Monaghan, "Kernel estimates as a basis for general particle methods in hydrodynamics," *Journal of Computational Physics*, vol. 46, pp. 429–453, 1982.

[368] J. J. Monaghan, "Particle methods for hydrodynamics," *Computer Physics Reports*, vol. 3, no. 2, pp. 71–124, 1985.

[369] S. Siegler and H. Riffert, "Smoothed particle hydrodynamics simulations of ultrarelativistic shocks with artificial viscosity," *Astrophys. J.*, vol. 531, pp. 1053–1066, 2000.

[370] F. Banyuls, J. A. Font, J. M. A. Ibanez, J. M. A. Marti, and J. A. Miralles, "Numerical 3+1 General Relativistic Hydrodynamics: A Local Characteristic Approach," *Astrophys. J.*, vol. 476, p. 221, 1997.

[371] M. Shibata, T. W. Baumgarte, and S. L. Shapiro, "Stability of coalescing binary stars against gravitational collapse: Hydrodynamical simulations," *Phys. Rev. D*, vol. 58, p. 023002, 1998.

[372] A. Bauswein, *Relativistic simulations of compact object mergers for nucleonic matter and strange quark matter*. PhD thesis, Technische Universität München, 2010.

[373] R. Courant, K. Friedrichs, and H. Lewy, "Über die partiellen differenzengleichungen der mathematischen physik," *Mathematische annalen*, vol. 100, no. 1, pp. 32–74, 1928.

[374] J. J. Monaghan, "SPH and Riemann Solvers," *Journal of Computational Physics*, vol. 136, no. 2, pp. 298–307, 1997.

[375] E. Chow and J. J. Monaghan, "Ultrarelativistic SPH," *J. Comput. Phys.*, vol. 134, pp. 296–305, 1997.

[376] D. S. Balsara, "von Neumann stability analysis of smooth particle hydrodynamics–suggestions for optimal algorithms," *Journal of Computational Physics*, vol. 121, no. 2, pp. 357–372, 1995.

[377] R. L. Arnowitt, S. Deser, and C. W. Misner, "Dynamical Structure and Definition of Energy in General Relativity," *Phys. Rev.*, vol. 116, pp. 1322–1330, 1959.

[378] T. W. Baumgarte, G. B. Cook, M. A. Scheel, S. L. Shapiro, and S. A. Teukolsky, "General relativistic models of binary neutron stars in quasiequilibrium," *Phys. Rev. D*, vol. 57, pp. 7299–7311, 1998.

[379] W. L. Briggs, V. E. Henson, and S. F. McCormick, *A Multigrid Tutorial, Second Edition*. Philadelphia, PA: Society for Industrial and Applied Mathematics, second ed., 2000.

[380] L. Blanchet, T. Damour, and G. Schaefer, "Postnewtonian hydrodynamics and postnewtonian gravitational wave generation for numerical relativity," *Mon. Not. Roy. Astron. Soc.*, vol. 242, pp. 289–305, 1990.

[381] G. Faye and G. Schaefer, "Optimizing the third and a half postNewtonian gravitational radiation reaction force for numerical simulations," *Phys. Rev. D*, vol. 68, p. 084001, 2003.

[382] A. Bauswein, S. Goriely, and H. T. Janka, "Systematics of dynamical mass ejection, nucleosynthesis, and radioactively powered electromagnetic signals from neutron-star mergers," *Astrophys. J.*, vol. 773, p. 78, 2013.

[383] M. Kölsch, T. Dietrich, M. Ujevic, and B. Bruegmann, "Investigating the mass-ratio dependence of the prompt-collapse threshold with numerical-relativity simulations," *Phys. Rev. D*, vol. 106, no. 4, p. 044026, 2022.

[384] R. Kashyap *et al.*, "Numerical relativity simulations of prompt collapse mergers: Threshold mass and phenomenological constraints on neutron star properties after GW170817," *Phys. Rev. D*, vol. 105, no. 10, p. 103022, 2022.

[385] C. Constantinou, B. Muccioli, M. Prakash, and J. M. Lattimer, "Thermal properties of hot and dense matter with finite range interactions," *Phys. Rev. C*, vol. 92, no. 2, p. 025801, 2015.

[386] T. Fließbach, *Allgemeine Relativitätstheorie*. Berlin, Heidelberg: Springer Berlin Heidelberg, 2016. 7th eddition.

[387] L. Tolos, M. Centelles, and A. Ramos, "The Equation of State for the Nucleonic and Hyperonic Core of Neutron Stars," *Publ. Astron. Soc. Austral.*, vol. 34, p. e065, 2017.

[388] Y. Sugahara and H. Toki, "Relativistic mean field theory for unstable nuclei with nonlinear sigma and omega terms," *Nucl. Phys. A*, vol. 579, pp. 557–572, 1994.

[389] M. Hempel, T. Fischer, J. Schaffner-Bielich, and M. Liebendorfer, "New Equations of State in Simulations of Core-Collapse Supernovae," *Astrophys. J.*, vol. 748, p. 70, 2012.

[390] H. Toki, D. Hirata, Y. Sugahara, K. Sumiyoshi, and I. Tanihata, "Relativistic many body approach for unstable nuclei and supernova," *Nucl. Phys. A*, vol. 588, no. 1, pp. c357–c363, 1995.

[391] S. Typel, G. Ropke, T. Klahn, D. Blaschke, and H. H. Wolter, "Composition and thermodynamics of nuclear matter with light clusters," *Phys. Rev. C*, vol. 81, p. 015803, 2010.

[392] D. Alvarez-Castillo, A. Ayriyan, S. Benic, D. Blaschke, H. Grigorian, and S. Typel, "New class of hybrid EoS and Bayesian M-R data analysis," *Eur. Phys. J. A*, vol. 52, no. 3, p. 69, 2016.

[393] G. Shen, C. J. Horowitz, and S. Teige, "A New Equation of State for Astrophysical Simulations," *Phys. Rev. C*, vol. 83, p. 035802, 2011.

[394] S. Typel and H. H. Wolter, "Relativistic mean field calculations with density dependent meson nucleon coupling," *Nucl. Phys. A*, vol. 656, pp. 331–364, 1999.

[395] E. Wigner and F. Seitz, "On the Constitution of Metallic Sodium," *Phys. Rev.*, vol. 43, pp. 804–810, 1933.

[396] G. Shen, C. J. Horowitz, and S. Teige, "Equation of State of nuclear matter in a Virial expansion of nucleons and nuclei," *Phys. Rev. C*, vol. 82, p. 045802, 2010.

[397] G. Shen, C. J. Horowitz, and S. Teige, "Equation of State of Dense Matter from a density dependent relativistic mean field model," *Phys. Rev. C*, vol. 82, p. 015806, 2010.

[398] J. M. Lattimer and F. D. Swesty, "A Generalized equation of state for hot, dense matter," *Nucl. Phys. A*, vol. 535, pp. 331–376, 1991.

[399] A. S. Schneider, L. F. Roberts, and C. D. Ott, "Open-source nuclear equation of state framework based on the liquid-drop model with Skyrme interaction," *Phys. Rev. C*, vol. 96, no. 6, p. 065802, 2017.

[400] X. Du, A. W. Steiner, and J. W. Holt, "Hot and dense matter equation of state probability distributions for astrophysical simulations," *Phys. Rev. C*, vol. 105, no. 3, p. 035803, 2022.

[401] A. Akmal, V. R. Pandharipande, and D. G. Ravenhall, "The Equation of state of nucleon matter and neutron star structure," *Phys. Rev. C*, vol. 58, pp. 1804–1828, 1998.

[402] A. S. Schneider, C. Constantinou, B. Muccioli, and M. Prakash, "Akmal-Pandharipande-Ravenhall equation of state for simulations of supernovae, neutron stars, and binary mergers," *Phys. Rev. C*, vol. 100, no. 2, p. 025803, 2019.

[403] S. Furusawa, H. Togashi, H. Nagakura, K. Sumiyoshi, S. Yamada, H. Suzuki, and M. Takano, "A new equation of state for core-collapse supernovae based on realistic nuclear forces and including a full nuclear ensemble," *J. Phys. G*, vol. 44, no. 9, p. 094001, 2017.

[404] H. Togashi, K. Nakazato, Y. Takehara, S. Yamamuro, H. Suzuki, and M. Takano, "Nuclear equation of state for core-collapse supernova simulations with realistic nuclear forces," *Nucl. Phys. A*, vol. 961, pp. 78–105, 2017.

[405] I. Bombaci and D. Logoteta, "Equation of state of dense nuclear matter and neutron star structure from nuclear chiral interactions," *Astron. Astrophys.*, vol. 609, p. A128, 2018.

[406] D. Logoteta, A. Perego, and I. Bombaci, "Microscopic equation of state of hot nuclear matter for numerical relativity simulations," *Astron. Astrophys.*, vol. 646, p. A55, 2021.

[407] E. Chabanat, P. Bonche, P. Haensel, J. Meyer, and R. Schaeffer, "A Skyrme parametrization from subnuclear to neutron star densities. 2. Nuclei far from stablities," *Nucl. Phys. A*, vol. 635, pp. 231–256, 1998. [Erratum: Nucl.Phys.A 643, 441–441 (1998)].

[408] H. Shen, H. Toki, K. Oyamatsu, and K. Sumiyoshi, "Relativistic equation of state of nuclear matter for supernova explosion," *Prog. Theor. Phys.*, vol. 100, p. 1013, 1998.

[409] H. Shen, H. Toki, K. Oyamatsu, and K. Sumiyoshi, "Relativistic equation of state of nuclear matter for supernova and neutron star," *Nucl. Phys. A*, vol. 637, pp. 435–450, 1998.

[410] Z. Zhang, Y. Lim, J. W. Holt, and C. M. Ko, "Nuclear dipole polarizability from mean-field modeling constrained by chiral effective field theory," *Phys. Lett. B*, vol. 777, pp. 73–78, 2018.

[411] J. L. Forest, V. R. Pandharipande, and J. L. Friar, "Relativistic nuclear Hamiltonians," *Phys. Rev. C*, vol. 52, pp. 568–575, 1995.

[412] M. Piarulli, L. Girlanda, R. Schiavilla, A. Kievsky, A. Lovato, L. E. Marcucci, S. C. Pieper, M. Viviani, and R. B. Wiringa, "Local chiral potentials with Δ-intermediate states and the structure of light nuclei," *Phys. Rev. C*, vol. 94, no. 5, p. 054007, 2016.

[413] D. Logoteta, I. Bombaci, and A. Kievsky, "Nuclear matter properties from local chiral interactions with Δ isobar intermediate states," *Phys. Rev. C*, vol. 94, no. 6, p. 064001, 2016.

[414] B. D. Day, "Elements of the Brueckner-Goldstone Theory of Nuclear Matter," *Rev. Mod. Phys.*, vol. 39, pp. 719–744, 1967.

[415] V. Dexheimer, "Tabulated Neutron Star Equations of State Modeled within the Chiral Mean Field Model," *Publ. Astron. Soc. Austral.*, vol. 34, p. E006, 2017.

[416] H. Kochankovski, A. Ramos, and L. Tolos, "Hyperonic Uncertainties in Neutron Stars, Mergers and Supernovae," *arXiv e-prints*, 2023.

[417] V. Dexheimer and S. Schramm, "Proto-Neutron and Neutron Stars in a Chiral SU(3) Model," *Astrophys. J.*, vol. 683, pp. 943–948, 2008.

[418] M. A. R. Kaltenborn, N.-U. F. Bastian, and D. B. Blaschke, "Quark-nuclear hybrid star equation of state with excluded volume effects," *Phys. Rev. D*, vol. 96, no. 5, p. 056024, 2017.

[419] L. Tolos, M. Centelles, and A. Ramos, "Equation of State for Nucleonic and Hyperonic Neutron Stars with Mass and Radius Constraints," *Astrophys. J.*, vol. 834, no. 1, p. 3, 2017.

[420] M. Hanauske, L. R. Weih, H. Stöcker, and L. Rezzolla, "Metastable hypermassive hybrid stars as neutron-star merger remnants: A case study," *Eur. Phys. J. ST*, vol. 230, no. 2, pp. 543–550, 2021.

[421] M. Hanauske and L. R. Weih, "Neutron star collisions and gravitational waves," *Astron. Nachr.*, vol. 342, no. 5, pp. 788–798, 2021.

[422] K. Chatziioannou, J. A. Clark, A. Bauswein, M. Millhouse, T. B. Littenberg, and N. Cornish, "Inferring the post-merger gravitational wave emission from binary neutron star coalescences," *Phys. Rev. D*, vol. 96, no. 12, p. 124035, 2017.

[423] H. Yang, V. Paschalidis, K. Yagi, L. Lehner, F. Pretorius, and N. Yunes, "Gravitational wave spectroscopy of binary neutron star merger remnants with mode stacking," *Phys. Rev. D*, vol. 97, no. 2, p. 024049, 2018.

[424] A. Torres-Rivas, K. Chatziioannou, A. Bauswein, and J. A. Clark, "Observing the post-merger signal of GW170817-like events with improved gravitational-wave detectors," *Phys. Rev. D*, vol. 99, no. 4, p. 044014, 2019.

[425] K. W. Tsang, T. Dietrich, and C. Van Den Broeck, "Modeling the postmerger gravitational wave signal and extracting binary properties from future binary neutron star detections," *Phys. Rev. D*, vol. 100, no. 4, p. 044047, 2019.

[426] P. J. Easter, S. Ghonge, P. D. Lasky, A. R. Casey, J. A. Clark, F. H. Vivanco, and K. Chatziioannou, "Detection and parameter estimation of binary neutron star merger remnants," *Phys. Rev. D*, vol. 102, no. 4, p. 043011, 2020.

[427] M. Breschi, R. Gamba, S. Borhanian, G. Carullo, and S. Bernuzzi, "Kilohertz Gravitational Waves from Binary Neutron Star Mergers: Inference of Postmerger Signals with the Einstein Telescope," *arXiv e-prints*, p. arXiv:2205.09979, 2022.

[428] A. W. Criswell, J. Miller, N. Woldemariam, T. Soultanis, A. Bauswein, K. Chatziioannou, M. W. Coughlin, G. Jones, and V. Mandic, "Hierarchical Bayesian method for constraining the neutron star equation of state with an ensemble of binary neutron star postmerger remnants," *Phys. Rev. D*, vol. 107, no. 4, p. 043021, 2023.

[429] K. Walker, R. Smith, E. Thrane, and D. J. Reardon, "Precision constraints on the neutron star equation of state with third-generation gravitational-wave observatories," *arXiv e-prints*, p. arXiv:2401.02604, 2024.

[430] G. Lioutas, A. Bauswein, and N. Stergioulas, "Frequency deviations in universal relations of isolated neutron stars and postmerger remnants," *Phys. Rev. D*, vol. 104, no. 4, p. 043011, 2021.

[431] J. Keller, C. Wellenhofer, K. Hebeler, and A. Schwenk, "Neutron matter at finite temperature based on chiral effective field theory interactions," *Phys. Rev. C*, vol. 103, no. 5, p. 055806, 2021.

[432] J. Keller, K. Hebeler, and A. Schwenk, "Nuclear Equation of State for Arbitrary Proton Fraction and Temperature Based on Chiral Effective Field Theory and a Gaussian Process Emulator," *Phys. Rev. Lett.*, vol. 130, no. 7, p. 072701, 2023.

[433] G. A. Lalazissis, T. Niksic, D. Vretenar, and P. Ring, "New relativistic mean-field interaction with density-dependent meson-nucleon couplings," *Phys. Rev. C*, vol. 71, p. 024312, 2005.

[434] A. Sedrakian and A. Harutyunyan, "Delta-resonances and hyperons in proto-neutron stars and merger remnants," *Eur. Phys. J. A*, vol. 58, no. 7, p. 137, 2022.

[435] K. Kiuchi, K. Kyutoku, Y. Sekiguchi, and M. Shibata, "Global simulations of strongly magnetized remnant massive neutron stars formed in binary neutron star mergers," *Phys. Rev. D*, vol. 97, no. 12, p. 124039, 2018.

[436] K. Kiuchi, S. Fujibayashi, K. Hayashi, K. Kyutoku, Y. Sekiguchi, and M. Shibata, "Self-Consistent Picture of the Mass Ejection from a One Second Long Binary Neutron Star Merger Leaving a Short-Lived Remnant in a General-Relativistic Neutrino-Radiation Magnetohydrodynamic Simulation," *Phys. Rev. Lett.*, vol. 131, no. 1, p. 011401, 2023.

[437] E. R. Most, S. P. Harris, C. Plumberg, M. G. Alford, J. Noronha, J. Noronha-Hostler, F. Pretorius, H. Witek, and N. Yunes, "Projecting the likely importance of weak-interaction-driven bulk viscosity in neutron star mergers," *Mon. Not. Roy. Astron. Soc.*, vol. 509, no. 1, pp. 1096–1108, 2021.

[438] P. Hammond, I. Hawke, and N. Andersson, "Impact of nuclear reactions on gravitational waves from neutron star mergers," *Phys. Rev. D*, vol. 107, no. 4, p. 043023, 2023.

[439] M. Chabanov and L. Rezzolla, "Impact of bulk viscosity on the post-merger gravitational-wave signal from merging neutron stars," *arXiv e-prints*, p. arXiv:2307.10464, 2023.

[440] M. G. Alford and A. Haber, "Strangeness-changing Rates and Hyperonic Bulk Viscosity in Neutron Star Mergers," *Phys. Rev. C*, vol. 103, no. 4, p. 045810, 2021.

[441] V. Vijayan, N. Rahman, A. Bauswein, G. Martínez-Pinedo, and I. L. Arbina, "Impact of pions on binary neutron star mergers," *Phys. Rev. D*, vol. 108, no. 2, p. 023020, 2023.

[442] S. Huth, C. Wellenhofer, and A. Schwenk, "New equations of state constrained by nuclear physics, observations, and QCD calculations of high-density nuclear matter," *Phys. Rev. C*, vol. 103, no. 2, p. 025803, 2021.

[443] K. Kyutoku, M. Shibata, and K. Taniguchi, "Reducing orbital eccentricity in initial data of binary neutron stars," *Phys. Rev. D*, vol. 90, no. 6, p. 064006, 2014.

[444] J. Healy, C. O. Lousto, H. Nakano, and Y. Zlochower, "Post-Newtonian Quasicircular Initial Orbits for Numerical Relativity," *Class. Quant. Grav.*, vol. 34, no. 14, p. 145011, 2017.

Danksagung

Am Ende meiner Promotion möchte ich herzlich allen Menschen meinen Dank aussprechen, die mich in dieser Zeit begleitet und unterstützt haben. Es war eine einerseits spannende und aufregende, andererseits aber durch die Pandemie auch manchmal eintönige, schwierige und unsichere Zeit. Zuerst möchte ich mich sehr herzlich bei meinem Betreuer Andreas Bauswein für das spannende Projekt, die Stelle in seiner Arbeitsgruppe, die fortlaufende Unterstützung, das stets professionelle und konstruktive Feedback und seine endlose Geduld bedanken. Ich habe besonders geschätzt, dass er immer für Diskussionen und Rückfragen verfügbar war und man ohne Furcht auch schlechten Nachrichten und enttäuschenden Resultate überbringen konnte. Ich danke außerdem der TU Darmstadt und dem SFB1245 für die Möglichkeit zu promovieren und die Finanzierung meiner Stelle und dem GSI Helmholtzzentrum für Schwerionenforschung für die Bereitstellung ihrer Infrastruktur für meine Forschung. Außerdem danke ich Gabriel Martínez-Pinedo für die Bereitschaft, Zweitkorrektor meiner Dissertation zu sein und Tetyana Galatyuk und Michael Vogel dafür, als Prüfer in meiner Disputation zur Verfügung zu stehen. Des weiteren bedanke mich mich sehr herzlich bei Hristijan Kochankovski, Angels Ramos, Stefan Typel und Laura Tolos für die gute und produktive Zusammenarbeit an meinen Projekten, ohne die diese Arbeit nicht zustande gekommen wäre. Außerdem danke ich Niels-Uwe Bastian, David Blaschke, Tobias Fischer, Micaela Oertel und Theodoros Soultanis für die Mitarbeit an meiner ersten Publikation über das Thema meiner Masterarbeit, welche zu Beginn meiner Promotion fertiggestellt wurde.

Ich bedanke mich auch bei den aktuellen und ehemaligen Mitgliedern unserer Arbeitsgruppe Christine Collins, Juliane Helbich, Oliver Just, Georgios Lioutas, Aristeidis Nikolaidis, Theodoros Soultanis, Lukas Schnabel und Vimal Vijayan sowie Zafar Iftikhar, Gerrit Leck, Ignacio Lopez de Arbina, Thomas Neff, Christian Schwebler, Diana Alvear Terrero und allen weiteren Mitarbeitern der Arbeitsgruppe von Prof. Martínez-Pinedo im Theoriezentrum der GSI für die stets kollegiale Stimmung auf der Arbeit. Die Atmosphäre war immer entspannt, ich habe mich sehr wohlgefühlt und wenn nötig von allen Seiten Unterstützung und Hilfe erfahren. Ich möchte in diesem Zusammenhang auch meinen ehemaligen Bürokollegen Elena Hanu, Bowen Jiang, Christopher Johnson und Dag Fahlin Strömberg danken. Ich habe auch immer die gemeinsamen Ausflüge außerhalb der Arbeit genossen. Insbesondere die zahlreichen (Schnee-) Wanderungen während der Pandemie haben dazu beigetragen, diese schwierige Zeit zu überstehen.

Abseits der Arbeit möchte ich mich auch bei meinen Freunden Alex, Anna, Ben, Nicole und Rudhi für alle gemeinsamen Unternehmungen der letzten Jahren bedanken. Sie haben mir sehr durch diese Zeit geholfen und ich wünsche allen alles Gute. Einen ganz besonderen Dank möchte ich Shriya für alles aussprechen, was sie für mich getan hat, seit wir uns kennengelernt haben. Mit ihr ist das Leben so viel schöner und leichter geworden und ich bin jeden Tag aufs Neue glücklich, sie an meiner Seite zu haben. Ich danke ihr auch sehr herzlich für das Korrekturlesen dieser Arbeit, ohne das zahlreiche Fehler unentdeckt geblieben wären. Zuletzt möchte ich natürlich bei meiner Familie, insbesondere bei Beate, Daniela und Karl für die bedingungslose Liebe und Unterstützung bedanken, ohne die ich niemals so weit gekommen wäre. Ich könnte mir keine bessere Familie wünschen.